Nuclear magnetic resonance studies of spin and strain phenomena in nanohole GaAs/AlGaAs quantum dots

Ian Michael Griffiths

Thesis submitted for the degree of
Doctor of Philosophy

Department of Physics and Astronomy
University of Sheffield

July 2021

Abstract

This thesis details experimental measurements performed on III-V semiconductor quantum dots, with the main body of work on nanohole GaAs/AlGaAs quantum dots. Through the use of optically detected nuclear magnetic resonance (NMR) and micro-photoluminescence, the components of the gradient elastic tensor, an important material parameter, are determined for GaAs. These values are $S_{11,^{69}\mathrm{Ga}} = (-22.2 \pm 1.1) \times 10^{21}\,\mathrm{V\,m^{-2}}$, $S_{11,^{75}\mathrm{As}} = (23.9 \pm 1.1) \times 10^{21}\,\mathrm{V\,m^{-2}}$, with $\left(\frac{S_{44}}{S_{11}}\right)_{^{75}\mathrm{As}}$ being in the range of 1.20 to 2.36 and $\left(\frac{S_{44}}{S_{11}}\right)_{^{69}\mathrm{Ga}}$ being in the range of -0.88 to -0.11. These values are significantly different to that of the previous work, however, the ratio of the first components for the two nuclei, $\frac{S_{11,^{69}\mathrm{Ga}}}{S_{11,^{75}\mathrm{As}}}$, is in close agreement with the previous work, with other derived material parameters being in agreement with the accepted values. The second component of the gradient elastic tensor, S_{44}, is found to be in close agreement for one nuclei, with a factor of 2 difference for the other nuclei. We conclude that the previous work had unrecognised systematic errors that impacted their results.

We study two GaAs/AlGaAs samples with different barrier thicknesses, using NMR and micro-photoluminescence, and observe unexpected up-conversion and dynamic nuclear polarisation phenomena in both samples, one of which was measured with and without externally applied stress. One of the unexpected phenomena, up-conversion, has its origin isolated to three potential impurities / defects in two possible locations in the sample. The other unexpected phenomena, relating to nuclear polarisation, are discussed in depth with their potential origins being presented.

In addition to this, the fabrication of Schottky diodes for charge control of InGaAs quantum dot samples is detailed with the initial characterisation, through photoluminescence spectroscopy, being performed to identify the quantum dot states and charge plateaus.

Acknowledgements

There are many people that have helped me during this PhD that I wish to thank.

I must thank my supervisor, Evgeny Chekhovich, for training me in the lab and assisting me with his in depth scientific knowledge, as well as Maurice Skolnick, Paul A Crowther and Matt Mears for their help when the road became rough.

With regards to samples, I would like to thank Huiying Huang, Xueyong Yuan, Saimon Filipe Covre da Silva and Armando Rastelli for providing the nanohole GaAs/AlGaAs quantum dot samples and Edmund Clarke for the InGaAs quantum dot samples. I would also like to thank Ian Farrer, Charlotte Ovenden and Aristotelis Trapalis for their invaluable assistance and expertise with performing measurements on the Schottky structures and titanium films, as well as Ben Royall, Ken Kennedy and Saurabh Kumar for both the training they gave me and their sound help and advice in the device fabrication cleanroom.

The measurements contained within this work would have been nothing without the reliable supply of liquid helium, so a considerable thank you to both Chris Vickers and Phil Taylor for providing what they somehow made appear to be an endless supply - I have no idea how you do it!

I would also like to thank Ata Ul Haq, Gau Ragunathan, George Gillard and TJ Broomhall for their help, support and advice in the lab; and Catherine Phillips and Joe Maguire for their support outside of the lab, especially when things were tough.

Finally, and most importantly, I would like to thank my fiancée Claire for her endless support and encouragement - without you this would not have been possible and I promise that two PhDs is enough!

Contents

1 Introduction **1**

2 Background **5**
2.1 Growth of quantum dots . . . 6
2.2 Quantum dot states . . . 9
2.2.1 Excitons . . . 11
2.2.2 Strain . . . 13
2.3 Effect of electric and magnetic fields . . . 16
2.4 Charge state control . . . 19
2.5 Nuclear spins . . . 21
2.6 Nuclear spin manipulation . . . 23

3 Experimental techniques **27**
3.1 Sample structure . . . 27
3.1.1 GaAs/AlGaAs dot samples . . . 27
3.1.2 InGaAs dot samples . . . 29
3.2 Experimental setup . . . 30
3.2.1 RF generation . . . 35
3.2.2 Pump-probe technique . . . 38
3.3 Strained samples . . . 39
3.3.1 Finite element modelling . . . 40
3.4 Confidence intervals for multi-parameter models . . . 41

4 Schottky diodes for optical experiments **43**
4.1 Background . . . 43
4.2 Schottky diode sample fabrication . . . 44
4.2.1 Connecting to the n-layer without etching . . . 46
4.2.2 Thin titanium window . . . 51
4.2.3 Optimisation of thermal deposition of thin titanium films . . . 53
4.3 Photoluminescence of InGaAs self-assembled quantum dots (SAQDs) with varying tunnelling barriers . . . 55

5 Measuring the gradient elastic tensor of GaAs **61**
5.1 Background . . . 61
5.2 Measurement of the S_{11} component . . . 64
5.2.1 Experimental technique . . . 67
5.2.2 Results . . . 70

5.2.3 Discussion 76
5.3 Measurement of the S_{44} component 78
5.3.1 Results 81
5.4 Discussion 85

6 Understanding observed up-conversion and DNP phenomena 87
6.1 Up-conversion 87
6.2 DNP 90
6.3 Experiments 92
6.4 Results 94
6.4.1 Sample B (120 nm barrier) 94
6.4.2 Sample C (12 nm barrier) 102
6.5 Discussion 105
6.5.1 Up-conversion observed in PLE 105
6.5.2 Dynamic nuclear polarisation (DNP) from excitation energies less than X^0 113
6.5.3 Helicity independent DNP at low powers in sample C 116
6.5.4 Inverted DNP polarisation below QW in sample C 116
6.5.5 Reversal of DNP near X^0 at high powers in sample B 117
6.6 Summary 118

7 Summary and future work 119

8 Bibliography 121

List of Tables

3.1 GaAs/AlGaAs quantum dot sample structures. The Aluminium content (x) is 0.5 for sample A and 0.4 for samples B & C. 28
3.2 Sample structure for the InGaAs SAQD samples. The distributed Bragg reflectors (DBRs) are highlighted as they are the only layers that are repeated, as indicated in the left-most column. 30

5.1 Summary of the S_{11} experimental results 76
5.2 S_{11} values from [54]. The values have been converted from cgs to SI. . . . 77

6.1 Relevant impurity and defect levels for up-conversion, with their energy shown relative to either the conduction (E_c) or valence (E_v) band. 111
6.2 Summary of impurity and defect levels that are potentially responsible for the observed up-conversion. 113

List of Figures

2.1 Comparison of the characteristic changes in the density of states with increasing dimensions of confinement. The energy of the first state increases with the confinement. 5
2.2 Representation of the three different growth modes that occur during deposition. The blue circles represent the substrate, with the red circles representing the material being deposited. 6
2.3 Line profiles of a typical nanohole along two directions, measured by AFM. Data courtesy of Armando Rastelli / Johannes Kepler University Linz. . . . 9
2.4 Bulk band structure for a zincblende crystal. The light-holes (*lh*) and heavy-holes (*hh*) are degenerate at the Γ point, with the split-off (*so*) band being considerably far from the other valence band states. 10
2.5 Energy diagram for the bright exciton and biexciton states in a quantum dot. 14
2.6 Exciton spin states split by the Zeeman effect for the two field geometries, with the allowed optical transitions. 18
2.7 Schematic of n-type Schottky structure. 20

3.1 Representative schematic diagram of the band structure of an etched nanohole GaAs/AlGaAs quantum dot. 28
3.2 Representative photoluminescence (PL) spectrum of the GaAs/AlGaAs quantum dots (in sample B), under low power HeNe ($632\,\mathrm{nm}$, approximately $1.96\,\mathrm{eV}$) excitation at zero magnetic field. 29
3.3 Representative schematic diagram of the continuous flow cryostat. 31
3.4 Schematic diagram of the optics used with the continuous flow cryostat. Some mirrors have been omitted for clarity. 32
3.5 Representative schematic of the bath cryostat system. The inset shows a zoomed in view of the sample, objective lens and NMR coil. Some of the wiring, ports and aluminium blocks have been omitted for clarity. 33
3.6 Schematic diagram of the optics used for the bath cryostat system. These optics are physically separated, with optical fibres, shown in the middle of the diagram, connecting the two parts together. The pump laser for the titanium-sapphire laser and some mirrors have been omitted for clarity. 34
3.7 Schematic diagram of the RF circuit. All connecting lines represent $50\,\Omega$ coaxial cabling. 35
3.8 Reflection spectrum of the radio frequency (RF) circuit and coil matched for $^{75}\mathrm{As}$ at $8\,\mathrm{T}$ (the resonant frequency is shown with the black vertical line). . 37
3.9 Reflection spectrum of the RF circuit and coil matched for three isotopes at $8\,\mathrm{T}$. 37

3.10 PL spectrum of a quantum dot's X^0 transitions, at $8\,\mathrm{T}$, under opposite circularly polarisations of a $1.643\,\mathrm{eV}$ laser, resulting in an Overhauser field of opposite signs. The dot's transitions with a zero Overhauser field will approximately be in the middle of the two polarisations. 38
3.11 Representative schematic of the pump-probe cycle, with the direction of the nuclear spins (of three isotopes) shown at the top and the general effect on the resulting Overhauser field shown at the bottom. The modification in this instance represents the depolarisation of one of the isotopes. 39
3.12 Representative diagrams of the clamps used to apply compressive stress to the samples. 40

4.1 Representative schematic of the legacy mask set. The DBRs have been omitted for clarity. 45
4.2 AFM of the edge of a mesa on a working sample (SF1109), with multiple profiles being taken along the same edge of the mesa. The grey shaded area shows the location of the n-doped layer in the sample. 46
4.3 Profiles of gold diffusing from a layer into GaAs at several time points ($t_0 = 0$ and $t_0 < t_1 < t_2 < t_3$). The shaded region represents the depth of the n-layer, with negative depth values representing the region of the gold layer. 48
4.4 Modelling of the sample's resistance during the annealing process with different thicknesses of the gold layer. 49
4.5 Investigation of the contact diffusion time. (a) shows the position of the measurement points on the sample (red ellipses), (b) shows the resistance versus the annealing time. 50
4.6 energy dispersive X-ray spectrometery (EDX) of the tuneable and non-tuneable samples with a $3\,\mathrm{kV}$ electron beam. The peaks are labelled with their associated elements. 52
4.7 Optical transmittance of thermally evaporated titanium onto glass microscope slides versus the resistance across the width of the slide. The continuous lines at the top of the graph are the transmittance, at the different wavelengths, for a glass slide without any deposited titanium. Annotations on the graph are of the approximate thickness values. The data points represented by crosses are for evaporations at lower deposition rates. 54
4.8 Bias PL maps of a quantum dot in each of the three InGaAs samples. The thickness of the tunnelling barriers in the samples is shown above each of the graphs. 55
4.9 Normalised power dependence of a typical dot in the sample with a $52\,\mathrm{nm}$ tunnelling barrier. The spectra are annotated with their excitation power and the dot's lines are annotated with their associated states. 56
4.10 Linearly polarised detection of a dot in the $52\,\mathrm{nm}$ tunnelling barrier sample, with the lines annotated with their respective states and the splitting between the two polarisations. 57
4.11 The intensities of the three identified lines for each of the dots in the three samples, whose tunnelling barrier is shown above each graph. The solid and dashed lines are for the two different measurement sweeps (see text). 57

4.12 Comparison of the normalised intensities of the X^{-1} lines for each of the samples. The solid and dashed lines are for the two different measurement sweeps (see text). 58

5.1 Schematic of an NMR spectrum, where ν_0 is the resonant frequency of the nuclei and ν_Q is the quadrupolar frequency. 64
5.2 Ratio of asymmetric to symmetric biaxial strain for the $(0\,0\,1)$ surface of the sample when compressive stress is applied along the $[0\,0\,1]$ direction. Data is from a finite element model. 68
5.3 Ratio of shear to biaxial strain for the $(0\,0\,1)$ surface of the sample when compressively stressed along the $[0\,0\,1]$ direction. Data is from a finite element model. 68
5.4 Strain in the $[1\,1\,0]$ direction for the $(0\,0\,1)$ surface of the sample when compressively stressed along the $[1\,1\,0]$ direction. Data is from a finite element model. 69
5.5 Ratio of biaxial to hydrostatic strain for the $(0\,0\,1)$ surface of the sample when compressively stressed along the $[1\,1\,0]$ direction. Data is from a finite element model. 70
5.6 Representative nuclear magnetic resonance (NMR) spectra, of $^{75}\mathrm{As}$, for the three strain configurations. The quadrupolar frequency, ν_Q, is labelled between the $-\frac{3}{2} \Leftrightarrow \frac{1}{2}$ and $-\frac{1}{2} \Leftrightarrow \frac{1}{2}$ transitions. 71
5.7 Representative PL spectra, of GaAs, for the three strain configurations. The PL from the predominantly light- and heavy-hole states is annotated with 'LH' and 'HH', respectively. For the unstressed and $[1\,1\,0]$ stressed spectra, two orthogonal polarisations of the PL are shown. This is not shown for the $[0\,0\,1]$ stressed spectra as it is not dependent on polarisation. 72
5.8 Energy of the GaAs PL peaks verses the $^{75}\mathrm{As}$ quadrupolar frequency for quantum dots in the three stress configurations (annotated below data). . . . 73
5.9 The splitting of the light- and heavy-hole peaks in PL verses the quadrupolar frequency for the $[0\,0\,1]$ stressed and unstressed samples. 73
5.10 The average energy of the light- and heavy-hole peaks in PL verses the quadrupolar frequency for the $[1\,1\,0]$ stressed sample. 74
5.11 Comparison of the $^{69}\mathrm{Ga}$ and $^{75}\mathrm{As}$ quadrupolar frequencies for quantum dots in all three stress configurations. 75
5.12 Schematic diagram of the angles describing the sample's rotation. 79
5.13 NMR spectra for a quantum dot in the $[1\,1\,0]$ stressed sample in three orientations. Markers have been added above the satellite transition peaks. 82
5.14 Quadrupolar frequency of both $^{75}\mathrm{As}$ and $^{69}\mathrm{Ga}$ for the $[1\,1\,0]$ stressed sample with respect to the sample's polar angle, for two different azimuth angles. The dotted lines are from equation 5.42 using the fitted parameters. For convenience, the quadrupolar frequency, on the vertical axis, is the magnitude rather than the absolute value. 83
5.15 Quadrupolar frequency for both isotopes with respect to the sample's orientation for quantum dots in an unstressed sample. 83

5.16 Direction of the largest principal strain (red) for two of the unstressed quantum dots, with the estimated error in the direction (blue) calculated using Monte Carlo sampling. 84
5.17 Difference in the magnitudes of the principal strain components ϵ_1 and ϵ_2, which are in the x and y direction, with respect to the azimuth angle of the largest of the two. The best-fit value shown in red, with the estimated confidence regions from Monte Carlo sampling shown in blue. Due to the definition of the principal strain vectors, each point has an azimuth angle at ϕ and ϕ+180° 85

6.1 Diagrams showing up-conversion processes that use an intermediate state, labelled as $|\mathrm{I}\rangle$, with the ground and excited states as $|0\rangle$ and $|\mathrm{E}\rangle$, respectively. 88
6.2 Schematic of the pump-probe cycle used in the wavelength dependence and nuclear spin dynamics measurements. T_p is the length of time that the sample is exposed to the pump laser and T_d is the length of time between the pump excitation pulse and the probe excitation pulse. 93
6.3 Wavelength dependence of DNP of quantum dot 1 in sample B. 95
6.4 Power dependence of PL (a) and photoluminescence excitation (PLE) spectra (b) of quantum dot 1 in sample B. 95
6.5 Integrated PLE of quantum dot 1 in sample B, across the X^0 emission (1.586 to $1.591\,\mathrm{eV}$). The inset plot additionally shows a PL spectrum in grey. . . . 96
6.6 Nuclear spin polarisation build-up and decay times of quantum dot 1 in sample B. The powers next to the data points is the power used for pumping. For the decay data points, the length of time used for pumping is shown in the legend. 97
6.7 Wavelength dependence of DNP of quantum dot 2 in sample B. 98
6.8 Power dependence of PL (a) and PLE spectra (b) of quantum dot 2 in sample B. 99
6.9 Integrated PLE of quantum dot 2 in sample B, across the X^0 emission (1.605 to $1.610\,\mathrm{eV}$). The inset plot additionally shows a PL spectrum in grey. . . . 100
6.10 Wavelength dependence of DNP of quantum dot 1 in the stressed sample B. 100
6.11 Power dependence of PL (a) and PLE spectra (b) of quantum dot 1 in the stressed sample B. 101
6.12 Integrated PLE of quantum dot 1 in the stressed sample B, across the X^0 emission (1.593 to $1.599\,\mathrm{eV}$). The inset plot additionally shows a PL spectrum in grey. 102
6.13 Nuclear spin polarisation build-up and decay times of quantum dot 1 in the stressed sample B. All of the points had an excitation power of $22\,\mathrm{mW}$ with the exception of the points at $1.70\,\mathrm{eV}$ which had an excitation power of $11\,\mathrm{mW}$. 103
6.14 Wavelength dependence of DNP of quantum dot 1 in sample C. 103
6.15 Power dependence of PL (a) and PLE spectra (b) of quantum dot 1 in sample C. 104
6.16 Integrated PLE of quantum dot 1 in sample C, across the X^0 emission (1.573 to $1.575\,\mathrm{eV}$). The inset plot additionally shows a PL spectrum in grey. . . . 105
6.17 Nuclear spin polarisation build-up and decay times for quantum dot 1 in sample C. 106

6.18 Comparison of the up-converted PL observed in the PLE measurements (bottom) to the PL spectra (top) for two quantum dots in sample B. The PL spectra, due to the energy range, show the GaAs emission at each dots' location. 107
6.19 Power dependence of the up-converted PL of quantum dot 1 in sample B. . 108
6.20 Energy diagram showing the up-conversion process when the emission from the quantum dot is being detected. The blue arrow represents the exciting of an electron from the valence band (VB) to an intermediate state ($|\mathrm{I}\rangle$). The orange arrow represents the exciting of an electron from the intermediate to an excited state in the quantum dot ($|\mathrm{E}\rangle$), with the green arrow representing the emission that is detected from the dot's excited state. The annotations CB and $|0\rangle$ are for the conduction band and the ground state of the quantum dot, respectively. 108
6.21 Normalised PL spectra of the two quantum dots in sample B for a range of excitation energies, as annotated to the right of each spectrum. 110
6.22 Impurity and defect levels in bulk GaAs, the confined GaAs of the quantum well and bulk $Al_{0.4}Ga_{0.6}As$ in relation to the conduction and valence bands (show as CB and VB, respectively) of each material. The possible energy range for the intermediate level is shaded green. 112
6.23 Wavelength dependence of DNP for excitation energies around the GaAs peaks observed in PL for quantum dot 1 in sample C. A PL spectrum for the dot is shown in grey at the bottom of the graph. 114

Acronyms

CCD charge-coupled device.

DBR distributed Bragg reflector.

DNP dynamic nuclear polarisation.

EDX energy dispersive X-ray spectrometery.

I-V current-voltage.

MBE molecular beam epitaxy.

MOVPE metalorganic vapour-phase epitaxy.

ND neutral density.

NMR nuclear magnetic resonance.

PL photoluminescence.

PLE photoluminescence excitation.

RF radio frequency.

RTA rapid thermal annealer.

SAQD self-assembled quantum dot.

XRR X-ray reflectometry.

Chapter 1

Introduction

Quantum dots are semiconductor nanostructures that confine charge carriers (electrons and holes) so that they can only occupy discrete states. As III-V semiconductors have a direct bandgap, quantum dots in these materials have a strong light-matter interaction, allowing the discrete states to be populated with charge carriers through the absorption of photons. The intrinsic spin of these charge carriers is a very attractive candidate for use in quantum computing as quantum bits. Whilst the light-matter interaction makes III-V quantum dots particularly interesting, they also have a non-insignificant matter-matter interaction. This interaction, between the spins of the charge carriers and the surrounding nuclear spins, results in the decoherence of the charge carrier's spin, decreasing the quality and usability of the quantum dot as a quantum bit. To maximise the potential of III-V quantum dots, it is therefore important to understand how these interactions affect the lifetime and coherence of the quantum dot states.

Due to their construction from different materials, quantum dots are inherently strained. A key parameter for describing this is the material specific gradient elastic tensor, which, amongst other things, can be used to understand and model the lifetimes and coherence of spins in a quantum dot.

This work measures the components of the gradient elastic tensor for GaAs, one of the most important III-V semiconductors, by utilising nanohole quantum dots as highly localised probes. It also investigates spin and other phenomena observed in these nanohole quantum dots that can give a more informed view of the structure and environment surrounding the quantum dots.

This thesis begins with a background on the concepts used (chapter 2), including the effects of confinement on materials, how quantum dots in semiconductors are grown, electronic states and excitons in quantum dots and how they are affected by electric and magnetic fields. The background finishes by discussing nuclear spins in the context of quantum dots and how they can be manipulated.

Chapter 3 describes the sample structure, experimental setup and the general experimental techniques used in this work.

Chapter 4 details the fabrication of Schottky diodes for InGaAs self-assembled quantum dot (SAQD) samples, covering the issues with previous sample fabrications, isolation of the issues and optimisation of the crucial parts of the fabrication technique. Whilst these samples do not form the basis for the experimental work contained in this thesis, the fabrication technique and the initial characterisation of the samples (also described in this chapter) have already been used for work outside the scope of this thesis.

The experimental work in this thesis is detailed in two chapters. The first, chapter 5, is on the measurement of the gradient elastic tensor for GaAs and begins with a theoretical background on the gradient elastic tensor and how it relates to strain and nuclear magnetic resonance (NMR). The measurement is split into two parts corresponding to the two unique components of the tensor, with the method and experimental results being discussed separately for each. The second, chapter 6, investigates the up-conversion and dynamic nuclear polarisation (DNP) phenomena that was observed in two samples. It discusses the experimental techniques used, the expected results and how the observed results contrast them. This is followed by a discussion and potential identification of the origin of the observed effects.

A summary of this thesis, with potential future work, can be found in chapter 7.

During the course of this work, two papers have been published on measuring the gradient elastic tensor of GaAs, which is detailed in chapter 5:

- E. A. Chekhovich, I. M. Griffiths, M. S. Skolnick, H. Huang, S. F. C. da Silva, X. Yuan & A. Rastelli. “Cross calibration of deformation potentials and gradient-elastic tensors of GaAs using photoluminescence and nuclear magnetic resonance spectroscopy in GaAs/AlGaAs quantum dot structures”. *Physical Review B* **97**(23), 235311 (2018). DOI: 10.1103/physrevb.97.235311

- I. M. Griffiths, H. Huang, A. Rastelli, M. S. Skolnick & E. A. Chekhovich. "Complete characterization of GaAs gradient-elastic tensors and reconstruction of internal strain in GaAs/AlGaAs quantum dots using nuclear magnetic resonance". *Physical Review B* **99**(12), 125304 (2019). DOI: 10.1103/physrevb.99.125304

In addition to this, the InGaAs SAQD samples that were fabricated into Schottky diodes, as described in chapter 4 and section 4.3, have been studied in:

- G. Gillard, I. M. Griffiths, G. Ragunathan, A. Ulhaq, C. McEwan, E. Clarke & E. A. Chekhovich. "Fundamental limits of electron and nuclear spin qubit lifetimes in an isolated self-assembled quantum dot". *npj Quantum Information* **7**(1), 43 (2021). DOI: 10.1038/s41534-021-00378-2

Chapter 2

Background

By confining a material's dimensions, so that the length of the confinement is of the same order of magnitude as the charge carriers' de Broglie wavelength, the material's electronic density of states can be reduced from a continuum of states of the bulk material to only discrete electron and hole states in the confined dimension or dimensions, which is shown in figure 2.1. When the material is confined in all three dimensions, the charge carriers

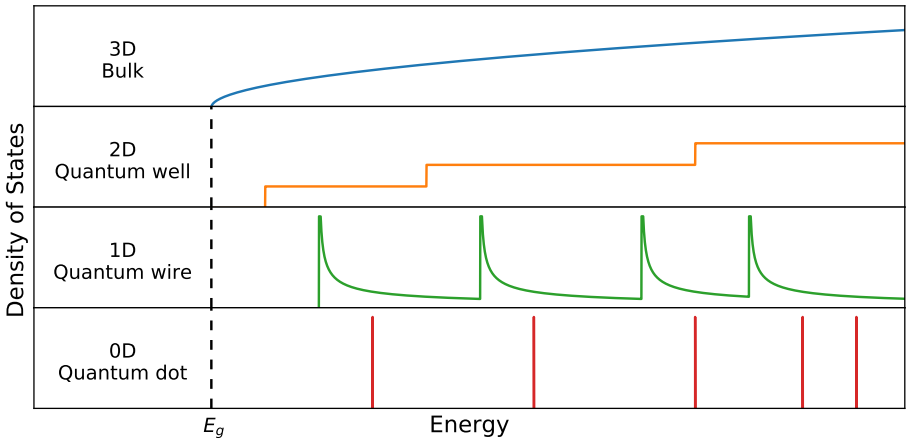

Figure 2.1: Comparison of the characteristic changes in the density of states with increasing dimensions of confinement. The energy of the first state increases with the confinement.

are effectively in a zero dimensional structure, in terms of their free movement, resulting in atomic-like discrete energy levels. Such a structure is called a quantum dot and were first observed in cuprous chloride crystals [1], but have since been made in a variety of ways and materials. In particular, quantum dots in semiconductors can be created either by physically limiting the amount of material (as with colloidal and one of the dimensions of nanowire or

pillar quantum dots) or by creating the confinement with a potential (as with electrostatic quantum dots and those created by a variation in material composition). This work uses optically active quantum dots in III-V semiconductors.

2.1 Growth of quantum dots

III-V semiconductor structures are typically grown either by molecular beam epitaxy (MBE) or metalorganic vapour-phase epitaxy (MOVPE), with atomic layers being deposited either physically from hot sources in a high quality vacuum or through a chemical reaction between gases, respectively. With both of these techniques, the layer by layer growth of one material on top of a substrate is determined by the strain at the interface and therefore depends on the lattice constants of the materials. There are three different regimes, which are pictorially shown in figure 2.2. With materials that have similar lattice constants, the mismatch results

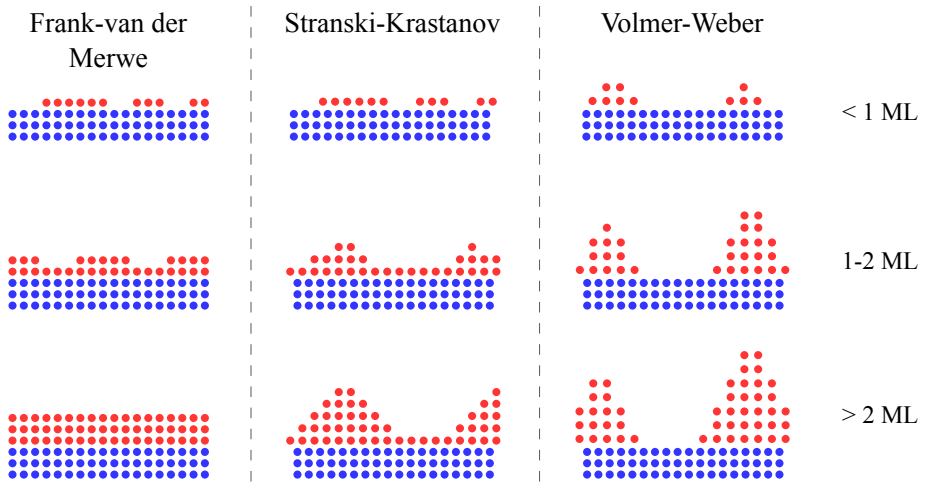

Figure 2.2: Representation of the three different growth modes that occur during deposition. The blue circles represent the substrate, with the red circles representing the material being deposited.

in a small amount of strain at the interface. However, this strain is small enough that the added material can grow as complete layers on top of the substrate – this is referred to as Frank-van der Merwe growth. When there is a large mismatch in the lattice constants, the strain at the interface between the two materials makes it energetically preferable to form islands, reducing the number of atoms at the interface of the two materials and increasing the number of surface atoms, which is referred to as Volmer-Weber growth. With a significant,

but smaller mismatch in the lattice constants (for example, the lattice constant of InAs is $7\,\%$ larger than GaAs), a combination of these two growth modes occurs, with one or more mono-layers being deposited prior to the island growth. This is referred to as Stranski-Krastanov growth and is the most well known method for growing III-V SAQDs [2]. An example of this is InAs SAQDs grown on GaAs, where the InAs forms islands on top of a wetting layer that is on average 1.7 mono-layers thick [3]. These islands are then capped with a GaAs layer, that is significantly thicker, to create a 3 dimensional confinement for the charge carriers. The location of the grown islands is inherently stochastic, but, as the growth is due to strain, can be controlled to a limited extent by fabricating areas of increased strain. It is worth noting that the SAQD's intrinsic strain will also act as a nucleation site for other dots, even when there is a fairly large layer between the dots, resulting in dots stacked in the growth direction [4].

The strain at the interface of the materials results in a migration of the materials across the boundary – in the case of InAs deposited onto GaAs, the dots are not pure InAs but InGaAs, with a higher concentration of indium at the top and gallium at the base of the dots [5]. When the dots are capped, for example with GaAs, further migration occurs with the height of the dots decreasing, blueshifting the emission wavelength [6]. Despite this, the indium concentration increases linearly from the base to the top of the dots [7]. In addition to this, the indium content of the dot can be modified after growth, and capping, by annealing, resulting in a further blueshift to the emission wavelength [8]. Whilst this does add a level of tuneability to the dots, it is an additional variable that will vary between dots and, in some ways, is an unnecessary complication.

The resulting intrinsic strain of a SAQD is quite significant and affects both the dot's electronic and optical properties (see section 2.2.2). An alternative to this are so-called 'strain-free' dots where the lattice constant of the dot's material is similar to the material the dot is grown on (and also capped with). This, of course, means that the growth is Frank-van der Merwe instead of Stranski-Krastanov, so several alternative techniques have been developed to grow these dots, with each having their advantages and disadvantages. One of the first techniques relies on several-monolayer fluctuations in the thickness of narrow quantum wells to create GaAs quantum dots [9]. This results in a strong confinement in the growth (z) direction, but the confinement in the x-y plane is weak and can be significantly

weaker than the lateral confinement found in InGaAs SAQDs. In a similar vein, islands of GaAs can be created at the interface of GaAs and AlGaAs by interrupting the growth for two minutes. Whilst these islands are a single monolayer high, and so have a strong confinement in the growth direction, they also suffer from poor lateral confinement [10]. Another technique is low temperature droplet growth, where GaAs dots are formed on an AlGaAs surface by alternatively depositing Ga and As at a low growth temperature ($250\,^{\circ}\mathrm{C}$). This produces GaAs islands whose size and density strongly depend on the growth conditions (i.e. temperature and material flux); however, these islands can become elongated, due to adatom surface migration [11]. Another disadvantage of low temperature growth is that it produces lower quality material than using typical growth temperatures (approximately 550 to $700\,^{\circ}\mathrm{C}$), which is why it is normally avoided. Another technique uses patterned substrates, where grooves, created by lithography and etching, are used to seed the dot growth [12, 13]. Whilst this can result in site controlled growth (in the case of [12]), the size and quality of the dots can vary significantly across the sample and any contaminants from the etching can affect the quality of the dots.

An alternative to this is to grow InAs quantum dots and then *in situ* etch them, leaving behind nanoholes in the GaAs substrate. A layer of AlGaAs, thicker than the depth of the holes, is then deposited. This fills in the holes, but, due to the surface diffusivity of aluminium, holes appear in the surface of the AlGaAs layer – effectively the holes in the GaAs are transferred to the AlGaAs layer. Dots can then be created by depositing GaAs into these nanoholes [14]. This technique, whilst producing good quality dots, leaves an InAs wetting layer from the initial dot growth, resulting in a strained layer close to the dots, which is a clear disadvantage when trying to create 'strain-free' dots. A further development of this, uses aluminium droplets to etch nanoholes into an AlAs or AlGaAs layer, thus avoiding a strained layer beneath the dots [15]. Aluminium is not the only material that can be used for the droplet etching, both gallium and indium can etch nanoholes into AlAs and AlGaAs [16]. However, with this technique, the droplet material crystallises on the walls of the nanohole and as a ring around the nanohole (see figure 2.3), which when indium or gallium is used results in a ring like quantum well and increased strain. Therefore, the use of aluminium for droplet etching is advantageous as the ring and walls of the nanoholes will be AlAs.

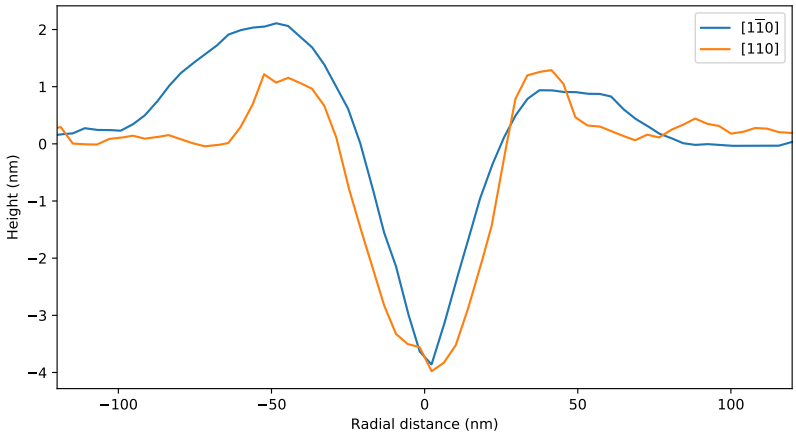

Figure 2.3: Line profiles of a typical nanohole along two directions, measured by AFM. Data courtesy of Armando Rastelli / Johannes Kepler University Linz.

In addition to GaAs/AlGaAs dots being significantly less strained than those grown by Stranski-Krastanov growth, they have an additional advantage – the GaAs deposited into the nanoholes undergoes very little intermixing during growth, the same cannot be said about strained dots.

An important aspect of many experiments with quantum dots, as well as going towards quantum computing and quantum information processing, is the ability to control the number of charge carriers present in a dot. This has been achieved in InGaAs SAQDs [17, 18] and in both interface fluctuation and droplet etched GaAs/AlGaAs dots [19–21].

2.2 Quantum dot states

The crystal structure of III-V semiconductors is either zincblende or wurtzite, with GaAs, as well as AlAs and InAs, having a zincblende structure, which will be the only one that is discussed, with its bulk band structure being shown in figure 2.4. The conduction band originates from *s*-type orbitals that have no orbital angular momentum ($l = 0$), resulting in a single value for the total spin momentum ($s = \frac{1}{2}$) and two possible projections ($S_z = \pm\frac{\hbar}{2}$). The valence band has, primarily, *p*-type orbitals that do have an angular momentum ($l = 1$), resulting in two possible total angular momentums ($j = \frac{1}{2}, \frac{3}{2}$). This splits the valence band into three sub-bands – the light holes ($j = \frac{3}{2}, J_z = \pm\frac{\hbar}{2}$), the heavy holes ($j = \frac{3}{2}, J_z = \pm\frac{3\hbar}{2}$) and the split-off band ($j = \frac{1}{2}, J_z = \pm\frac{\hbar}{2}$) [3]. The split-off band, split by the bulk

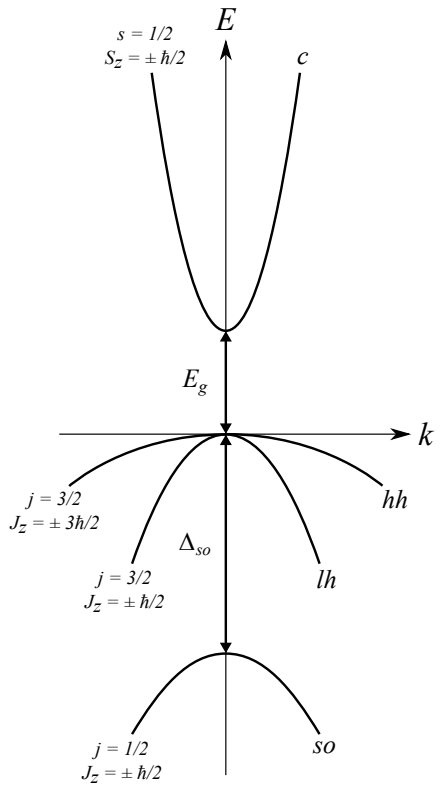

Figure 2.4: Bulk band structure for a zincblende crystal. The light-holes (*lh*) and heavy-holes (*hh*) are degenerate at the Γ point, with the split-off (*so*) band being considerably far from the other valence band states.

spin-orbit interaction, is approximately $340\,\mathrm{meV}$, for GaAs, below the other valence band states and so is typically ignored [22]. The light and heavy hole bands result from different projections of the same total angular momentum ($j = \frac{3}{2}$), with the heavy holes having a larger effective mass than the light holes (induced by the different curvatures of the bands), hence the naming – this increase is approximately a factor of 6 for GaAs and 15 for InAs [3, 22]. For an unstrained bulk crystal, the light and heavy holes bands are degenerate at the Γ point ($k = 0$) as is shown in figure 2.4. In a strained crystal, such as one containing SAQDs, this degeneracy is lifted due to a reduction in symmetry and there is a splitting between the light- and heavy-hole bands, which will be revisited later (in section 2.2.2). As the bands are approximately parabolic around the Γ point, electrons in the conduction band, and holes in the valence bands, effectively behave as free particles in the crystal [3].

Whilst quantum dots can have a variety of different shapes, both SAQD and GaAs/AlGaAs quantum dots typically have a hemispherical or lens-like shape, which allows the dot's states to be approximated by a pair of parabolic oscillators – one in the growth direction (z) and one in-plane (x-y) [3]. This is due to the grown dots having a smaller height than their width (by a factor of approximately 3 or 4), resulting in a significantly stronger confinement in

the growth direction than the in-plane confinement. The stronger confinement energetically separates the states to a much greater extent in the growth direction than in-plane, allowing the motions to be separated into two parabolic oscillators and results in the wavefunction in the growth direction typically being in its ground state. The in-plane wavefunction is two dimensional, with states in each dimension that can be combined into a single 'shell' quantum number, with these shell states having a $2n + 1$ degeneracy (with n starting from zero) [23]. From optical spectra, this simple model is surprisingly accurate, with the observable states corresponding well to this shell structure.

The stronger confinement in the z direction results in a quantisation of the z component of the carrier's momentum operator. This lifts the degeneracy of the light- and heavy-holes and results in a quantisation axis along the z direction [3]. We therefore define the spin states of an electron in the dot as $|\uparrow\rangle$ with $s_z = \frac{1}{2}$ and $|\downarrow\rangle$ with $s_z = -\frac{1}{2}$, and the hole spin states as $|\Uparrow\rangle$ with $j_z = \frac{3}{2}$ and $|\Downarrow\rangle$ with $j_z = -\frac{3}{2}$.

2.2.1 Excitons

The absorption of a photon, that is either resonant with one of the quantum dot optical transitions or from above bandgap excitation, excites an electron from the valence band into the conduction band, leaving an empty state (a hole) in the valence band. The electron hole pair, if generated with excess energy, will relax into the dot on sub-picosecond timescales, with the recombination of the pair inside the dot typically taking less than a nanosecond for spin-allowed excitons [3]. The electron hole pair interact through the Coulomb interaction to form a bound state known as an exciton. In bulk materials, the behaviour of excitons only depends on the ratio of their effective masses, producing a broad spectrum of states. When an exciton is confined in a quantum dot, the energy spectrum of the excitons is largely determined by the confinement, as the confinement potential is typical a factor of two larger than the exciton binding energy.

Excitons are not limited to only a single electron and hole, and can consist of any number of charge carriers – for example a singly charged exciton, or trion, consists of either two electrons and a hole, or two holes and an electron. For clarity, we shall refer to an exciton with a single electron and hole as X^0, two electrons and a hole as X^{-1}, and two holes and an electron as X^{+1} – that is, with the superscript referring to the exciton's overall charge.

In addition to this, there is also a biexciton which consists of two electrons and two holes, which will be denoted as XX^0. A biexciton is not simply the presence of two excitons in the dot (i.e. $2X^0$), as there is an interaction energy between them that can either be positive or negative, allowing both states to be observed.

For X^0 there are four possible combinations for the electron and hole spins – two where the spins are anti-parallel, $|\uparrow\Downarrow\rangle$ and $|\downarrow\Uparrow\rangle$, and two where they are parallel, $|\uparrow\Uparrow\rangle$ and $|\downarrow\Downarrow\rangle$. The states with parallel spins cannot be generated optically, through electric dipole transitions, and are known as dark states, whereas the anti-parallel spin states can be optically generated and are referred to as bright states [3]. For X^{-1}, the states are $|\uparrow\downarrow\Uparrow\rangle$ and $|\uparrow\downarrow\Downarrow\rangle$, and are always bright states as the dot's additional electron is not present before the excitation. It is a similar case for X^{+1}, with the states being $|\uparrow\Uparrow\Downarrow\rangle$ and $|\downarrow\Uparrow\Downarrow\rangle$. As XX^0 consists of both spins of electrons and holes, i.e. $|\uparrow\downarrow\Uparrow\Downarrow\rangle$, it can only be a bright state.

The relative energies of the exciton states depends on the particular Coulomb interaction in the dot, but will generally result in X^{-1} being below X^0 [3]. The X^{+1} state can be either above or below X^0, and can vary for quantum dots in the same sample. The biexciton can either be above or below X^0 depending on whether the attractive energy between the electron and holes under-compensates, or overcompensates, for the repulsion of identical carriers. However, the biexciton's photoluminescence (PL) intensity has a quadratic dependence on excitation power, compared with the linear dependence of the exciton and trions, allowing it to be easily identified.

In addition to this, there is an energy contribution from the exchange interaction that results in the states having a fine structure. For a neutral exciton, the general form of the interaction is,

$$H_{\text{ex}} = -\sum_{i=x,y,z} \left[a_i J_{h,i} \cdot S_{e,i} + b_i J_{j,i}^3 \cdot S_{e,i} \right], \tag{2.1}$$

where a and b are coupling coefficients and J_h and S_e are the spins of the hole and electron, respectively [24]. As we can ignore the light-holes and split-off band, the spins will be $J_h = \frac{3}{2}$ and $S_e = \frac{1}{2}$, resulting in total angular momentum projections ($M = S_{e,z} + J_{h,z}$) of either $|M| = 1$ for the bright states or $|M| = 2$ for the dark states. Using these states as a

basis ($|+1\rangle, |-1\rangle, |+2\rangle, |-2\rangle$), equation 2.1 can be represented in a matrix form,

$$H_{\text{ex}} = \frac{3}{16}\begin{pmatrix} \delta_0 & \delta_1 & 0 & 0 \\ \delta_1 & \delta_0 & 0 & 0 \\ 0 & 0 & -\delta_0 & \delta_2 \\ 0 & 0 & \delta_2 & -\delta_0 \end{pmatrix}, \tag{2.2}$$

where $\delta_0 = -\frac{1}{2}(4a_z + 9b_z)$, $\delta_1 = b_x - b_y$, and $\delta_2 = b_x + b_y$ [23]. The block diagonal form of the matrix means that there is no mixing between the bright and dark states. If the quantum dot has rotational symmetry in the xy plane then $b_x = b_y$, resulting in no mixing between the bright states (as $\delta_1 = 0$), with $|+1\rangle$ and $|-1\rangle$ being eigenstates of H_{ex}. However, if this symmetry is broken (i.e. $b_x \neq b_y$), as is often the case in SAQDs, then the bright states will be mixed. This results in eigenstates that are symmetric and antisymmetric linear combinations that are split by δ_1, producing a fine structure. These mixed eigenstates will have different linear polarisations, with respect to the crystal orientation, allowing the fine structure to be resolved in PL. The dark states, due to the form of δ_2, will always be mixed independently of the dot's rotational symmetry.

Singularly charged excitons do not have a fine structure, as the two like carriers (two electrons in X^{-1} and two holes in X^{+1}) will have a total spin projection of zero (this is due to the Pauli exclusion principle requiring the spins to be opposite). Whilst, for the same reason, the XX^0 state is degenerate, the biexciton emission does have a fine structure as an emission from XX^0 will result in an X^0 state occupying the dot. Therefore, if X^0 is split by δ_1, then so will the XX^0 state. As a result of this dependence, the linear polarisation for the transitions are opposite for the biexciton, with the lower energy component of the X^0 emission having the same polarisation as the higher energy component of the XX^0 emission – this is shown diagrammatically in figure 2.5 [25].

2.2.2 Strain

Up until this point, we have considered an unstrained zincblende crystal; however, as was stated earlier, in section 2.1, SAQDs are formed by strain and even 'strain-free' quantum dots still have a non-zero amount of strain (albeit significantly less than that of SAQDs), so

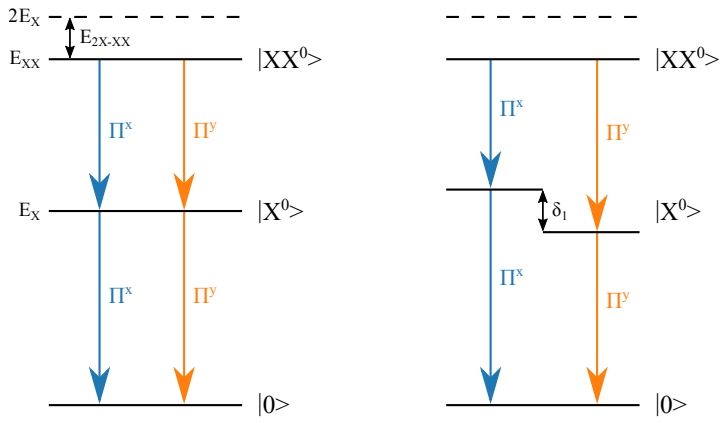

(a) Rotationally symmetric ($b_x = b_y$)

(b) Broken rotational symmetry ($b_x \neq b_y$)

Figure 2.5: Energy diagram for the bright exciton and biexciton states in a quantum dot.

it is necessary to consider the effects strain has on a quantum dot's states. Crystalline strain, caused by either a mismatch in the lattice constants or the material being externally stressed, deforms the crystal's unit cell, changing the length of the crystal's bonds and affecting the band structure [23]. As the deformation is significantly smaller than the size of the crystal, the strain can be modelled as infinitesimal and is described by a second rank tensor,

$$\epsilon_{ij} = \frac{1}{2}\left(\frac{\partial u_j}{\partial x_i} + \frac{\partial u_i}{\partial x_j} - \frac{\partial u_i \partial u_j}{\partial x_i \partial x_j}\right) \approx \frac{1}{2}\left(\frac{\partial u_j}{\partial x_i} + \frac{\partial u_i}{\partial x_j}\right), \tag{2.3}$$

where $\mathbf{u}$ is the displacement vector field of the strained crystal (relative to an unstrained crystal) and the subscripts, i and j, are either x, y or z [26]. From equation 2.3, it should be noted that the strain tensor is symmetric (i.e. $\epsilon_{ij} = \epsilon_{ji}$).

The conduction band is only affected by the hydrostatic component of strain, $\epsilon_h = \epsilon_{xx} + \epsilon_{yy} + \epsilon_{zz}$, with the edge of the band moving to,

$$E_c = E_c^0 + a_c \epsilon_h, \tag{2.4}$$

where E_c^0 is the edge of the unstrained material and a_c is the material dependent hydrostatic deformation potential for the conduction band. In a similar way, the valence band edge is

also affected by the hydrostatic strain,

$$E_v = E_v^0 + a_v \epsilon_h, \tag{2.5}$$

with the symbols representing the same quantities but for the valence band. As the change in the band gap is easily measurable, it is a useful quantity,

$$\Delta E_g = (a_c - a_v)\, \epsilon_h = a \epsilon_h. \tag{2.6}$$

In addition to the hydrostatic component, the valence band states are also affected by the biaxial and shear components of strain, which lifts the degeneracy of the light- and heavy-holes. This results in a splitting of the states, which, at the Γ point, is,

$$E_{v_{lh}^{hh}} = E_v^0 \pm \sqrt{b^2 \left(\epsilon_b^2 + \frac{3}{4} \epsilon_\eta^2 \right) + d^2 \epsilon_s^2}, \tag{2.7}$$

where b and d are the deformation potentials, $\epsilon_b = \epsilon_{zz} - \frac{1}{2}(\epsilon_{xx} + \epsilon_{yy})$ is the biaxial term of the strain, $\epsilon_\eta = \epsilon_{xx} - \epsilon_{yy}$ is the asymmetry in the biaxial strain and $\epsilon_s^2 = \epsilon_{xy}^2 + \epsilon_{xz}^2 + \epsilon_{yz}^2$ is the shear term of the strain. The notation of $E_{v_{lh}^{hh}}$ is used here to indicate that the heavy-hole (hh) state corresponds to the '$+$', with the light-hole (lh) state corresponding to '$-$'. For compressive strain, the heavy-hole states have higher energy than the light-hole states, and for tensile strain the light-hole states have higher energy than the heavy-hole states at the Γ point, but there is a certain k vector where the bands typically anti-cross and their characteristics change [27].

In addition to these shifts, the strain also affects the effective masses of both the electrons and holes, as they are dependent on the band gap. This results in the conduction and valence bands changing shape; however, for this work, it is only necessary for us to consider the changes that occur at, and around, the Γ point, which can be well described using 8-band $k \cdot p$ theory [27, 28].

It is worth noting that III-V materials are piezoelectric and can become polarised when they are strained. However, there are two reasons why we will not consider piezoelectric effects in this work. The first is that GaAs (and similar materials) are only significantly piezoelectric along the $[1\,1\,1]$ crystal direction. The samples used in this work are grown

along the $[0\,0\,1]$ direction, resulting in the largest intrinsic strain component, due to the lattice mismatch, also being in the $[0\,0\,1]$ direction. Those samples that were externally stressed (see section 5.2) were along the $[0\,0\,1]$ and $[1\,1\,0]$ directions. The second reason is that the piezoelectric polarisation is dependent on the shear component of strain and is independent of the hydrostatic and biaxial components [27]. It will be argued later that the shear components are significantly smaller than the other components of strain, and are significantly smaller than those required to see any polarisation.

2.3 Effect of electric and magnetic fields

Externally applied fields can be classified as either static or dynamic. Static fields affect the energy and symmetry of the states through a field that is constant whereas dynamic fields temporarily perturb the states, allowing them to be externally manipulated.

The application of a static electric field results in a small relative displacement of the electron and hole in an exciton, decreasing the binding energy of the exciton state [3]. For free excitons, when the applied field results in an energy shift of the exciton that is greater than the binding energy, the exciton will break apart. This results in a substantial decrease in the oscillator strength and significantly limits the state tuning in bulk materials. However, for well confined excitons, the electron and hole cannot separate and an energy shift much greater than the binding energy can be observed, known as the quantum confined Stark effect [29]. The change in the exciton's energy is quadratic with the electric field for small fields as the intrinsic dipole moment ($\mathbf{p_0}$) is small and the polarisability of the exciton (β) can be quite large,

$$\Delta E = -\mathbf{p_0} \cdot \mathbf{F} - \beta F^2, \tag{2.8}$$

where $\mathbf{F}$ is the externally applied electric field [23]. For large fields, where the separation of the electron and hole, $\frac{\beta \mathbf{F}}{e}$, becomes limited by the size of the quantum dot, the change in energy becomes linear with the electric field [3]. A typical quantum dot will have an intrinsic dipole moment as there will inevitably be a small relative displacement between the electron and hole wavefunctions. For example, in InGaAs quantum dots, the holes are localised at the indium rich top of the dot, whilst the electrons are delocalised over the entirety of the dot, resulting in a small dipole moment [3]. For these dots, the largest Stark shift is seen when

the electric field is applied along the growth direction, that is in the same direction as the intrinsic dipole moment.

A dynamic electric field has a similar effect to a static field; however, the resulting shift is also dependent on the frequency of the field. Typically, dynamic electric fields are applied to optically active quantum dots by the use of an additional non-resonant laser and is known as the optical Stark effect [30]. As this is not used in this work, it will be excluded from this discussion.

A static magnetic field couples to the spins of the carriers through the Zeeman effect and extends the fine structure splitting,

$$H_z = \mu_B \sum_{i=x,y,z} \left(g_{e,i} S_{e,i} - g_{h,i} J_{h,i}\right) B_i, \tag{2.9}$$

where S_e and J_h are the electron and hole spins, respectively, g_e and g_h are the Landé g-factors (also respectively), μ_B is the Bohr magneton and B is the magnetic field [23]. The orientation of the magnetic field to the spins, that is the growth axis of the quantum dots, affects the magnitude of the splitting as well as the allowed optical transitions, with there being two distinct configurations. The first is the Faraday geometry, where the magnetic field is parallel to the growth axis, that is out of the sample's plane, and the second is the Voigt geometry, where the magnetic field is perpendicular to the growth axis, that is in the sample's plane.

In the Faraday geometry, using the spin projection as a basis $\left(\frac{3}{2}, \frac{1}{2}, -\frac{1}{2}, -\frac{3}{2}\right)$, equation 2.9 becomes,

$$H_z = \frac{\mu_B B}{2} \begin{pmatrix} g_{e,z} + g_{h,z} & 0 & 0 & 0 \\ 0 & -(g_{e,z} + g_{h,z}) & 0 & 0 \\ 0 & 0 & -(g_{e,z} - g_{h,z}) & 0 \\ 0 & 0 & 0 & g_{e,z} - g_{h,z} \end{pmatrix}, \tag{2.10}$$

with the matrix having a diagonal form due to the rotational symmetry around the growth axis. This results in the bright exciton states ($|M| = 1$) linearly splitting with magnetic field and the dark exciton states ($|M| = 2$) having a non-linear splitting with magnetic field, due to their hybridisation at zero field. For asymmetric dots, the bright exciton states are linear

combinations of the eigenstates, resulting in the splitting having a quadratic dependence on magnetic field for low fields and a linear dependence for high fields, where the Zeeman energy is considerably larger than the exchange energy [23].

In the Voigt geometry, the rotation of the sample to the field affects the Hamiltonian, so for this discussion we will assume the field is parallel to the x axis, which makes equation 2.9 become,

$$H_z = \frac{\mu_B B}{2} \begin{pmatrix} 0 & 0 & g_{e,z} & g_{h,z} \\ 0 & 0 & g_{h,z} & g_{e,z} \\ g_{e,z} & g_{h,z} & 0 & 0 \\ g_{h,z} & g_{e,z} & 0 & 0 \end{pmatrix}. \tag{2.11}$$

The presence of the magnetic field breaks the rotational symmetry, mixing the bright and dark exciton states, allowing both to be observed in spectra. If the bright excitons have a higher energy without an applied magnetic field, an increasing field results in the bright excitons shifting to higher energies, with the dark excitons shifting to lower energies [23].

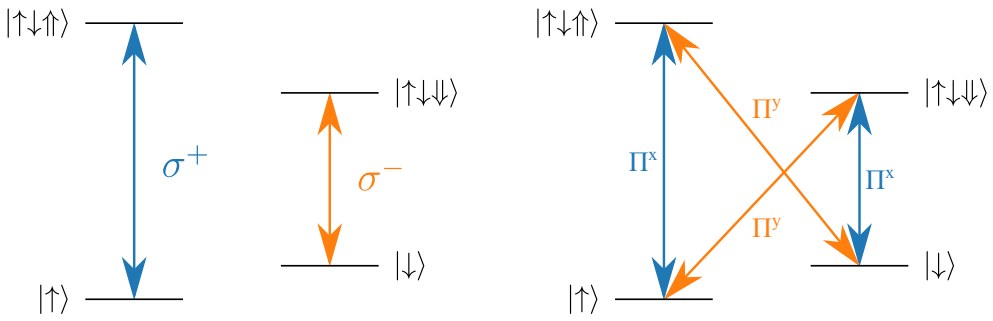

(a) Faraday (b) Voigt

Figure 2.6: Exciton spin states split by the Zeeman effect for the two field geometries, with the allowed optical transitions.

Excitons can be injected into a certain state through the polarisation of the optical excitation – circularly polarised light for the Faraday geometry and linearly polarised for the Voigt geometry, both of these are shown in figure 2.6. In the Voigt geometry, transitions between all four states are possible, but this is not the case in the Faraday geometry where the cross-transitions – those which could be used to change a spin up into a spin down electron – are not possible.

2.4 Charge state control

A static electric field, when combined with a doped layer, can also be used to control the charge carrier population of a quantum dot, but it is not the only method.

With SAQDs there are two methods of controlling the charge carrier population, which both rely on the placement of doped layers near to the quantum dot layer. The first method is referred to as delta-doping (or δ-doping), where the level of dopants in the doping layer is controlled during the growth so that the desired number of charge carriers are, on average, present in each dot. The second method manipulates the dot's states with respect to the doped layer, or layers, allowing the number of charge carriers to be actively controlled. Whilst the delta-doped layer approach is simpler, once the correct dopant concentration is found, it is less desirable as there will be many SAQDs that are unusable, with a charge carrier population that is either less or greater than the value targeted[1]. This is not an issue when using active control; however, the grown wafer has to be processed into a diode structure to enable the control.

For active control, an electric field is applied across the dot layer, shifting the energy levels of the confined states so that they can be adjusted with respect to the Fermi energy of the doped layer or layers. This can be achieved in a variety of ways, but typically uses a diode structure, with a Schottky diode being used to control a single charge carrying species (with the dopant determining which) and a p-i-n diode, utilising two doped regions, to control both species[2]. As we are only interested in controlling the electron population, n-type Schottky diodes were used, with both p-type Schottky and p-i-n diodes not being discussed any further.

A Schottky diode structure utilises an n-doped layer, below the dot layer, and a thin metallic contact, on the surface of the sample, to create an electric field across the dots. When a bias is applied to the diode, the energy levels of the confined states are raised, or lowered, with respect to the Fermi energy of the n-doped region (a Fermi sea). Figure 2.7a shows the schematic band structure for a quantum dot embedded in an n-type Schottky diode, with figure 2.7b illustrating the effect of the bias on the dot's states. We define V_n

[1] This is an inevitable drawback of a delta-doped structure relying on the statistical population rather than the actual population.

[2] A p-i-n diode can be used to control only a single charge carrying species by making one of the tunnelling barriers so thick that the energy levels of the dot cannot be brought inline with one of the doped layers. However, the layer structure is more complicated and more processing is required for a p-i-n diode than a Schottky diode.

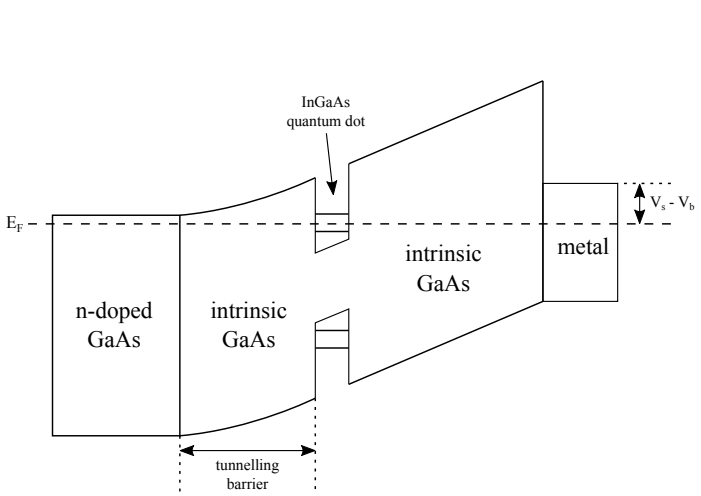

(a) Band structure

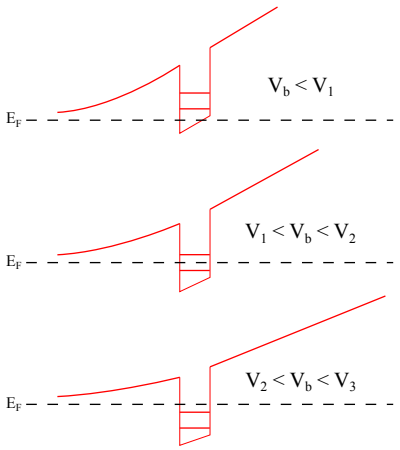

(b) Charge population for different biases (V_b).

Figure 2.7: Schematic of n-type Schottky structure.

as the voltage required to align the n^{th} electron state with the Fermi energy. So in the top diagram in figure 2.7b, where V_b is less than V_1, the energy of the first electron state is higher than the Fermi energy and so electrons in the Fermi sea cannot tunnel into the dot. If there were any electrons in the dot (i.e. if the bias voltage had changed), they would tunnel out into the Fermi sea on a timescale dependent on the barrier thickness. In the middle diagram, the bias voltage results in the Fermi energy being between the first and second electron states, allowing an electron from the Fermi sea to tunnel into the dot's first electron state, but not the second electron state, resulting in a single electron being in the dot. For the third diagram in figure 2.7b, the bias voltage results in both the first and second electron states being below the Fermi energy, and so they each can be occupied by an electron, resulting in two electrons being inside the dot.

Once an electron tunnels into the dot, there is a probability that it will tunnel out of the dot and another will tunnel in to replace it. This is an issue for spin manipulation experiments, as the spin state would be lost, and so it is important that the tunnelling probability is low enough that this does not negatively impact the experiment, whilst being high enough that the dot can become occupied in a reasonable amount of time. As the tunnelling probability depends exponentially on the width of the tunnelling barrier, the thickness of the tunnelling barrier between the doped region and the dots is a key part of the design of a charge control structure. In addition to this, the quality of the diode, in terms of the turn on and break down

voltages as well as the leakage current, is also important, as, in an ideal system, there should be no current flowing in the bias region used for charge controlling. If there is a significant current, for example, caused by a low breakdown voltage, the electric field across the dot becomes less dependent on the barrier thickness, resulting in a degraded charge control of the dot.

2.5 Nuclear spins

Up until this point, we have only discussed the spins of the charge carriers; however, they are not the only spins present in a quantum dot, with each nucleus, with non-zero spin, acting as a magnetic dipole. This results in a hyperfine interaction between the charge carriers in the quantum dot and the 10^4 to 10^6 nuclear spins that surround it [31]. It is possible to derive this interaction from the Dirac, or relativistic, Hamiltonian with an additional potential for an electromagnetic field; which results in the following,

$$H_{\text{hf}}^{n} = \frac{4}{3} g_n \mu_n \mu_0 \mu_B \delta(\mathbf{r}_n) \mathbf{S} \cdot \mathbf{I}_n \tag{2.12a}$$

$$+ \frac{1}{2\pi} g_n \mu_n \mu_0 \mu_B \left[\frac{3\left(\mathbf{I}_n \cdot \mathbf{r}_n\right)\left(\mathbf{S} \cdot \mathbf{r}_n\right)}{r_n^5} - \frac{\mathbf{I}_n \cdot \mathbf{S}}{r_n^3} \right] \tag{2.12b}$$

$$+ \frac{1}{2\pi} g_n \mu_n \mu_0 \mu_B \frac{\mathbf{L}_n \cdot \mathbf{I}_n}{r_n^3} \tag{2.12c}$$

where $\mathbf{S}$ is the charge carrier's spin, μ_0 is the permeability of free space and μ_B is the Bohr magneton; the subscript n refers to an individual nucleus that has a g factor of g_n, a nuclear magneton of μ_n, a spin of $\mathbf{I}_n$, an orbital angular momentum of $\mathbf{L}_n$ and is located at $\mathbf{r}_n$, relative to the charge carrier [32][3]. Equation 2.12 has been split into the three parts that define the hyperfine interaction, the Fermi-contact or isotropic interaction (2.12a), the dipole-dipole or anisotropic interaction (2.12b) and the nuclear spin orbit coupling to the charge carrier's orbital angular momentum (2.12c). For an electron in the conduction band, which has *s*-type orbitals, the Fermi-contact term dominates as it depends on the overlap of the carrier's wavefunction and the lattice sites, and there is no orbital angular momentum for the orbit coupling term. For holes in the valence band, which have *p*-type orbitals, the dipole-

[3] It is worth noting that this equation is slightly different to that found in [32] as it has been converted into SI units.

dipole term dominates as it depends on the overlap of the carrier's wavefunction with lattice anti-sites; however, it is approximately an order of magnitude weaker than the Fermi-contact term for conduction band electrons [33].

The Fermi-contact part of the hyperfine interaction can be re-written as,

$$H_{\text{hf}}^{n} = \nu_0 A_n \left|\psi\left(\mathbf{r}_n\right)\right|^2 \left(2I_z^n S_z + \left[I_+^n S_- + I_-^n S_+\right]\right), \tag{2.13}$$

where A_n is the constant for the hyperfine interaction, ν_0 is the volume of a two atom cell and $\psi\left(\mathbf{r}_n\right)$ is the carrier's envelope wavefunction at n [33]. Equation 2.13 is time-dependent and allows for the electron and nuclear spins to be exchanged. The $2I_z^n S_z$ term fluctuates with time but does not directly cause any exchanges and only results in a shift of the electron and nuclear spin transitions; however, the $\left[I_+^n S_- + I_-^n S_+\right]$ term allows for the exchange of spins between the electron and nuclear spins through simultaneous spin flips [33].

As a carrier in a quantum dot interacts with 10^4 to 10^6 nuclear spins, it can be considered that the electron is affected by a mean nuclear spin polarisation resulting in an effective magnetic field – the Overhauser field,

$$B_n = \frac{\nu_0}{g_e \mu_B} \sum_n A_n \left|\psi\left(\mathbf{r}_n\right)\right|^2 \langle \mathbf{I}_n \rangle. \tag{2.14}$$

Likewise, the nuclear spins are affected by the mean electron spin polarisation, resulting in the Knight field,

$$B_{Kn} = f \frac{\nu_0}{g_n \mu_n} A_n \left|\psi\left(\mathbf{r}_n\right)\right|^2 \langle \mathbf{S} \rangle, \tag{2.15}$$

where f is the electron filling factor of the quantum dot and is between zero and one [33]. From equation 2.15, it is worth noting that the Knight field cannot exist without an electron being present in the dot and the strength of the field decreases with the distance from the centre of the dot. In comparison, whilst the nuclear polarisation is independent on whether the dot contains an electron, the Overhauser field, being defined as the effect of the nuclear polarisation on the electron, is meaningless without the dot being occupied. Similarly, due to its definition, the Overhauser field cannot vary over the volume of the dot.

The existence of the spin-flipping term in equation 2.13 allows for the electron's spin to be exchanged with, or lost to, the nuclear spin bath when a transition would otherwise

be forbidden[4], but consequently allows for the manipulation of the nuclear spins. Providing that the nuclear spins have a long enough lifetime, the repeated injection of a spin polarised electron in to the quantum dot, that undergoes a spin-flip with the nuclear spins before it leaves the dot, will result in the nuclear spins becoming polarised, in what is referred to as DNP [10]. Through this technique, it is possible to achieve high polarisations of around $80\,\%$ [34].

The lifetime of a spin state, of either a charge carrier or nucleus, is characterised by two timescales – the spin relaxation time, T_1, and the spin decoherence time, T_2. The spin relaxation time characterises the time required for a spin to return to its equilibrium value (on the Bloch sphere, this is the polar angle); with the spin decoherence time characterising the time required for the spin to lose its phase information (the horizontal angle on the Bloch sphere). For an ensemble of spins, the rate of precession is often different across the ensemble (due to their local environment) resulting in the ensemble dephasing, which is characterised by the spin dephasing time, T_2^*. For quantum dot nuclear spin ensembles, $T_2^* < T_2$ and $T_2 << T_1$ [3, 31].

In semiconductor quantum dots, there are three relaxation mechanisms for nuclear spins [33]. The first, described above, is the spin-flipping term of the Fermi-contact part of the hyperfine interaction, often referred to as electron-mediated nuclear spin relaxation. The second is nuclear spin diffusion, where a flip-flop term in the dipolar coupling of the nuclear spins allows for spin exchange. This, however, does require that the nuclei have the same level spacing [35]. Finally, the third mechanism is quadrupolar nuclear spin relaxation, where the nuclear spins, through their quadrupole moments, couple to the electric field gradients of the lattice. Here the spin-flipping is either mediated through phonons, which is typically suppressed below $20\,\mathrm{K}$, or through charge fluctuations, from tunnelling or optical excitation.

2.6 Nuclear spin manipulation

A nuclear spin in a static magnetic field has its energy levels split by the Zeeman effect ($\hat{H}_z = -\gamma\hbar\mathbf{B}\cdot\hat{\mathbf{I}}$, where $\hat{\mathbf{I}}$ is a vector of the three spin operators $\hat{I}_x$, $\hat{I}_y$ and $\hat{I}_z$). With the field

[4]Such as when a magnetic field is applied, where the nuclear Zeeman splitting is significantly smaller than the equivalent electron splitting.

in the z direction, this is,

$$E_0 = \pm\gamma\hbar B_0 I_z, \tag{2.16}$$

where γ is the gyromagnetic ratio and B_0 is the field strength. The angular momentum's equations of motion can be described in the Heisenberg representation as,

$$\frac{\hbar}{i}\frac{d\hat{\mathbf{I}}}{dt} = \left[\hat{H}_z, \hat{\mathbf{I}}\right] \tag{2.17}$$

$$= -\gamma\hbar\left[\mathbf{B}\cdot\hat{\mathbf{I}}, \hat{\mathbf{I}}\right]. \tag{2.18}$$

If we look at the z component,

$$\frac{\hbar}{i}\frac{d\hat{I}_z}{dt} = -\gamma\hbar\left(B_x\left[\hat{I}_x, \hat{I}_z\right] + B_y\left[\hat{I}_y, \hat{I}_z\right]\right), \tag{2.19}$$

it can be written as,

$$\frac{d\hat{I}_z}{dt} = \gamma\left[\hat{\mathbf{I}}\times\mathbf{B}\right]_z. \tag{2.20}$$

This describes a torque between the magnetic field and the angular momentum of the nuclear spin, and is an analogue to a classical magnetic moment in a magnetic field,

$$\frac{d\mathbf{M}}{dt} = \gamma\mathbf{M}\times\mathbf{B}, \tag{2.21}$$

where $\mathbf{M}$ is the magnetic moment [35]. In fact, it is possible to treat the angular momentum as if it was a magnetic moment, and this is typically done in a rotating reference frame[5]. A reference frame that has an angular velocity of ω with respect to the laboratory frame, changes equation 2.21 to,

$$\frac{\partial\mathbf{M}}{\partial t} = \gamma\mathbf{M}\times\left(B_0 + \frac{\omega}{\gamma}\right)\hat{\mathbf{k}}, \tag{2.22}$$

where $\hat{\mathbf{k}}$ is a unit vector in the z direction. If the reference frame is rotating at $\omega_0 = -\gamma B_0$, then $\frac{\partial\mathbf{M}}{\partial t} = 0$ and there is no torque in the rotating frame, resulting in the magnetic moment precessing at a fixed angle to the magnetic field in the laboratory frame. This angular velocity is known as the Larmor frequency and is the moment's natural resonance in the field. Whilst this precession does occur, the angle of the precession varies with time due to relaxation

[5]For reasons which should become clear

mechanisms, aligning the moment with the magnetic field, resulting in a helical precession in the laboratory frame. This return to the equilibrium is characterised by the spin relaxation time (T_1),

$$\frac{dM_z}{dt} = -\frac{M_z - M_0}{T_1}, \tag{2.23}$$

where M_0 is the magnitude of the moment when aligned with $\mathbf{B}_0$ [35, 36].

If an additional transverse magnetic field, B_1, is added to the rotating reference frame, equivalent to an radio frequency (RF) signal in the laboratory frame, then equation 2.22 becomes,

$$\frac{\partial \mathbf{M}}{\partial t} = \gamma \mathbf{M} \times \left[\left(B_0 + \frac{\omega}{\gamma} \right) \hat{\mathbf{k}} + B_1 \hat{\mathbf{i}} \right], \tag{2.24}$$

where $\hat{\mathbf{i}}$ is a unit vector in the x direction. This results in a torque in the rotating frame and a time dependent precession in the laboratory frame. Assuming the moment is initially in the z direction, then the angle (α) between the moment and the z direction is,

$$\cos(\alpha) = 1 - 2\sin^2(\theta)\sin^2\left(\frac{1}{2}\gamma |\mathbf{B}_{\text{eff}}| t\right), \tag{2.25}$$

where $|\mathbf{B}_{\text{eff}}| = \frac{1}{\gamma}\sqrt{(\omega - \omega_0)^2 + \omega_1^2}$, with $\omega_n = -\gamma B_n$. As B_1 is typically much smaller than B_0 in experiments, α can only become large when $|\omega - \omega_0|$ is comparable to $|\omega_1|$, that is when the additional magnetic field is resonant, or near resonant, with the Larmor frequency [35, 37].

Relating this back to the nuclear spin's angular momentum, the static magnetic field creates an equilibrium where the angular momentum is in an eigenstate of the Zeeman Hamiltonian. This can be manipulated from one eigenstate to another, by applying an RF signal that is resonant with the transition - this is the Larmor frequency.

Chapter 3

Experimental techniques

This work is predominantly based on the measurements of GaAs/AlGaAs quantum dots in a bath cryostat system, with the samples and the experimental techniques used being described in the following sections. In addition to this, significant effort went into the fabrication and initial characterisation of InGaAs quantum dots that have since been used for other experiments [38]. The fabrication and initial characterisation are detailed in the last two sections of this chapter. However, the InGaAs samples are not mentioned outside of this chapter, as the subsequent experiments involving them are beyond the scope of this thesis.

3.1 Sample structure

3.1.1 GaAs/AlGaAs dot samples

Three samples containing GaAs/AlGaAs dots – grown using the etched nanohole method described in section 2.1 – were used. The structure of the samples is shown in table 3.1 and a representative band structure is shown in figure 3.1. The samples consist of an AlGaAs barrier layer on top of a GaAs buffer. The quantum dots are created by the Al etching droplets creating nanoholes in the barrier which are then filled by GaAs. Practically, this results in the barrier between the dot and the buffer layer being less than the barrier thickness shown in table 3.1.

From the table, it can be seen that there are quite a few differences between the samples. However, a number of these, coloured in light grey in the table, have no effect on the opti-

A (AS52)	B (AS82)	C (AS118)		
-	-	4 nm	GaAs	capping layer for C
-	-	0.75 ML	Al	etching droplets
-	-	30 nm	$Al_xGa_{1-x}As$	
7 nm	4 nm	2 nm	GaAs	capping layer for A & B
-	0.75 ML	-	Al	etching droplets
100 nm	120 nm	100 nm	$Al_xGa_{1-x}As$	
3.5 nm	4 nm	4 nm	GaAs	quantum dots
0.75 ML	0.75 ML	0.75 ML	Al	etching droplets
100 nm	120 nm	12 nm	$Al_xGa_{1-x}As$	barrier
320 nm	250 nm	250 nm	GaAs	buffer layer

Table 3.1: GaAs/AlGaAs quantum dot sample structures. The Aluminium content (x) is 0.5 for sample A and 0.4 for samples B & C.

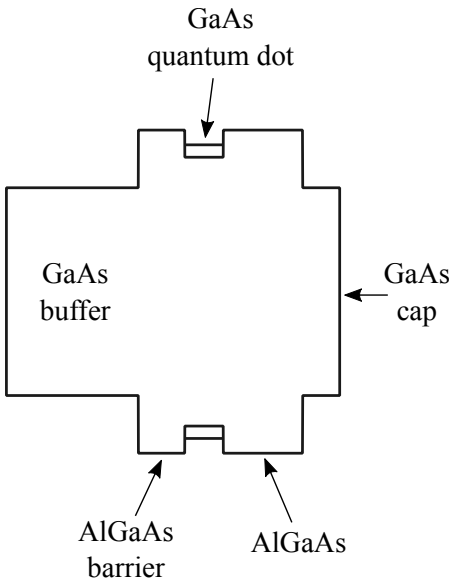

Figure 3.1: Representative schematic diagram of the band structure of an etched nanohole GaAs/AlGaAs quantum dot.

cal properties of the sample, or the properties of the dots, and are there either to protect the AlGaAs layers from oxidation or to allow non-optical microscopy of the dots. The main differences between the samples is the thickness of the barrier layer and the aluminium content of the AlGaAs layers.

An example of the PL spectrum for sample B is shown in figure 3.2, where there are three distinct features – the bulk GaAs around 1.49 to $1.51\,\mathrm{eV}$, a quantum dot around $1.57\,\mathrm{eV}$ and the quantum well at approximately $1.69\,\mathrm{eV}$, which is considerably brighter. These general

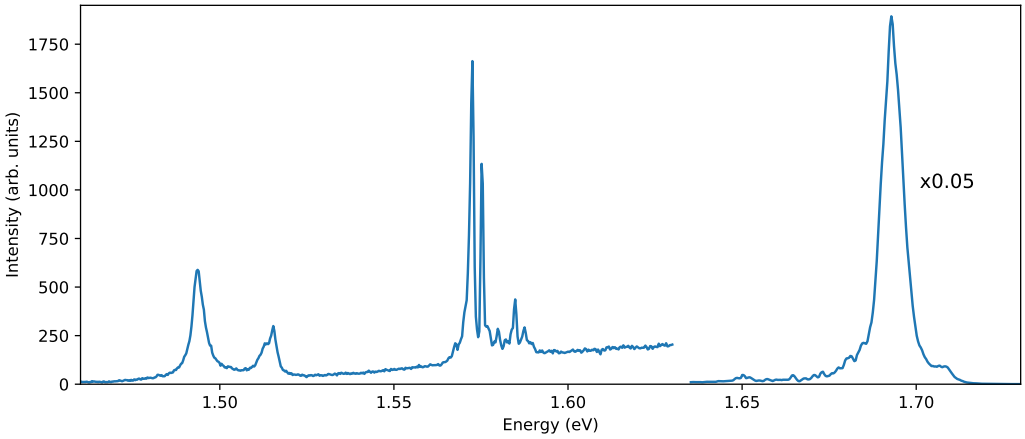

Figure 3.2: Representative PL spectrum of the GaAs/AlGaAs quantum dots (in sample B), under low power HeNe ($632\,\mathrm{nm}$, approximately $1.96\,\mathrm{eV}$) excitation at zero magnetic field.

features are present in all the samples; however, the quantum well in sample A is at significantly higher energy.

3.1.2 InGaAs dot samples

There are three InGaAs SAQD samples that have been used in this work that share a common structure, which is shown in table 3.2, but have different tunnelling barrier thicknesses. The dots are embedded in a charge tuneable structure, as described in section 2.4, as well as a micro-cavity to improve the optical efficiency. The cavity is a $\frac{\lambda}{2}$ cavity centred around $930\,\mathrm{nm}$ that is created by using distributed Bragg reflectors (DBRs) as mirrors. DBRs utilise a change in the refractive index of two materials to create a mirror, with the thickness of the two materials determining the wavelength of light that is reflected. A single interface of two materials that have a different refractive index will produce a reflection, with a larger change in the refractive index resulting in a larger reflection and multiple repeats of the interface

	Thickness (nm)	Material	
2x	67.2	GaAs	top DBR
	78.6	AlAs	
	133.5	GaAs	spacer
	2	InAs	quantum dots
	t_{tun}	GaAs	tunnelling barrier
	118.5-t_{tun}	n-GaAs	n-doped layer
	15	GaAs	spacer
15x	78.6	AlAs	bottom DBR
	67.2	GaAs	
	200	GaAs	buffer layer

Table 3.2: Sample structure for the InGaAs SAQD samples. The DBRs are highlighted as they are the only layers that are repeated, as indicated in the left-most column.

– that is, using multiple pairs of the layers – increasing the mirror's reflectivity. The two DBRs used in these samples have 15 repeats of GaAs and AlAs layers for the bottom mirror – making it have quite a high reflectivity – and 2 repeats for the top mirror – allowing for the light to interact with the cavity as well as for it to be emitted from the sample so that it can be detected. As the sample uses a $\frac{\lambda}{2}$ cavity, the dot layer has to be in the middle of the two mirrors for the emission to be enhanced. With these three samples varying the thickness of the tunnelling barrier, a layer below the dots has to also be changed to ensure the dots are in the centre of the cavity. As the $15\,\mathrm{nm}$ GaAs spacing layer is to limit dopant segregation into the bottom DBR, which would affect its refractive index [39], the thickness of the n-doped layer has to be decreased with increasing tunnelling barrier thickness. The three samples had tunnelling barrier thicknesses of 37, 42 and $52\,\mathrm{nm}$ and will be referred to as I-37, I-42 and I-52, respectively.

3.2 Experimental setup

All measurements were performed at low temperatures using liquid helium in two different cryostats. The first system is based around a continuous flow cryostat, where liquid helium is continuously pumped through a heat exchanger. This heat exchanger cools a 'cold finger', inside an evacuated vessel, that the sample is attached to. A schematic of the cryostat is shown in figure 3.3. As the temperature depends on the flow of helium, this type of cryostat can be less stable than other cryostats and so was primarily used for characterising samples.

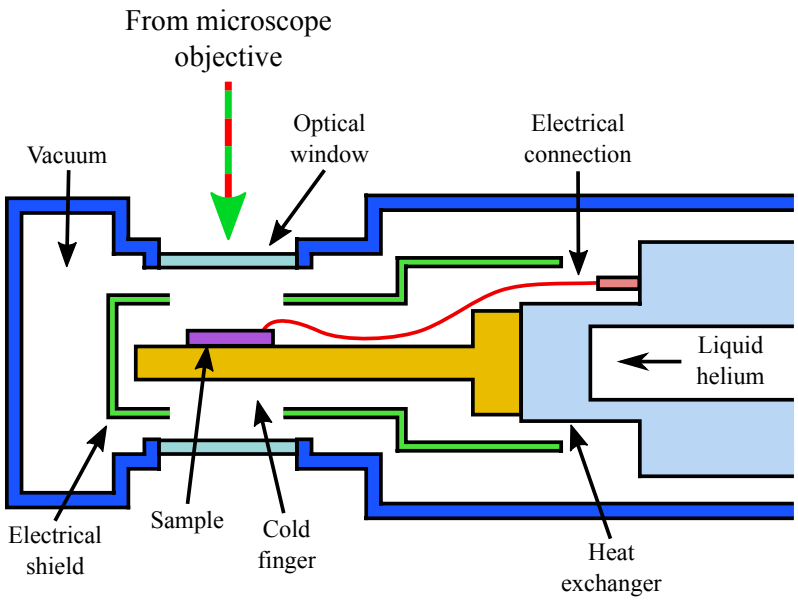

Figure 3.3: Representative schematic diagram of the continuous flow cryostat.

It therefore had a fairly simplistic optical setup, shown in figure 3.4, which allowed for micro-PL measurements to be performed. The light from an $850\,\mathrm{nm}$ laser diode is directed into a beam splitter through a neutral density filter wheel, which is used to control the light's power. The beam splitter symmetrically splits the light, with half going to a power meter and the other half to a microscope objective. The microscope objective is mounted on top of a piezoelectric stage, allowing limited fine movement along 3 axes, and focuses the light onto the sample inside the cryostat through the optical window. Light emitted by and reflected from the sample follows this path in reverse to the beam splitter where it is transmitted either to an alignment camera or to a fibre coupler, through a filter. A multi-mode fibre carries the light to a single spectrometer. This spectrometer has two selectable gratings (a $300\,\mathrm{mm}^{-1}$ and a $1200\,\mathrm{mm}^{-1}$), a Peltier cooled charge-coupled device (CCD) camera and, due to its design, requires that a low pass filter is used to prevent any of the laser light entering the spectrometer, despite the difference in wavelength. The cryostat is mounted on a coarse 2 axis mechanical stage, which is not shown in figure 3.3, this, with the piezoelectric stage, allows the entirety of the sample's surface to be accessible.

The second system uses a bath cryostat, which is schematically shown in figure 3.5, where a nonmagnetic stainless steel tube (the insert), is submerged in a cryostat containing liquid helium. A $10\,\mathrm{T}$ superconducting magnet sits at the bottom of the cryostat and has

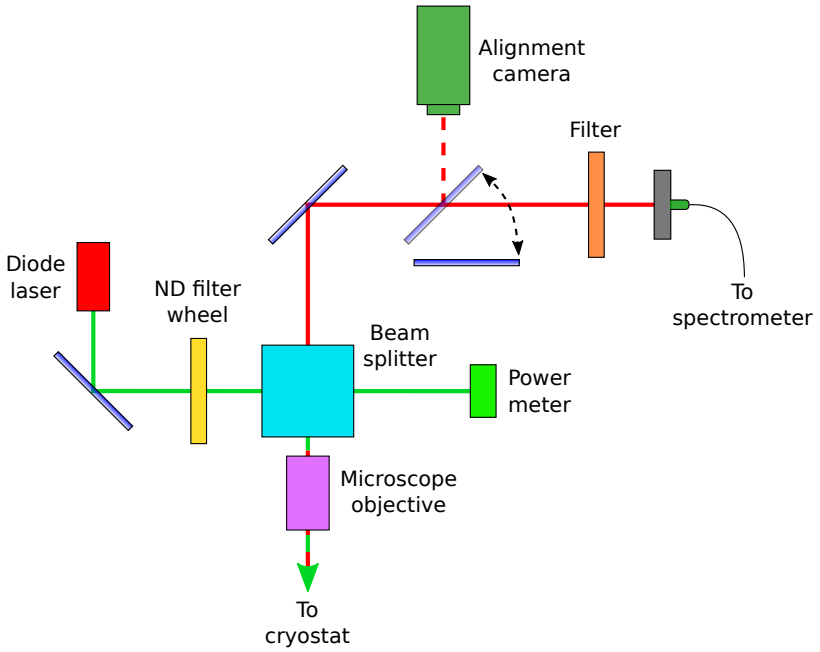

Figure 3.4: Schematic diagram of the optics used with the continuous flow cryostat. Some mirrors have been omitted for clarity.

a bore slightly larger than the insert's diameter, so that the bottom of the insert is placed in the magnet when it is installed. The insert uses a cage system, where 4 nonmagnetic stainless steel rods are held in place with aluminium blocks. All the aluminium blocks, with one exception, have an aperture in the middle of them allowing light to travel parallel to the insert to an optical window at the top of the insert. The last block has a 3 axis nanopositioner fitted to the aluminium block to which the sample is affixed and is positioned on the cage system so that the sample sits approximately in the middle of the magnet's bore. Two blocks, that are directly above the sample (with only one of these being shown in figure 3.5), hold an objective lens (one of several aspheric or achromatic doublets with focal lengths between 1.45 and $20\,\mathrm{mm}$, and a working distance between 0.81 and $17.7\,\mathrm{mm}$) and an RF coil (10 turns of $0.1\,\mathrm{mm}$ wire in 5 layers with an internal diameter of $0.4\,\mathrm{mm}$) used for NMR. The insert is evacuated and filled with a small amount of helium gas prior to it being installed in the cryostat, with this exchange helium ensuring that the sample is efficiently cooled. An optical breadboard is fitted directly above the optical window, which contains the majority of the optics.

The optical setup is more complicated than that of the continuous flow system, but shares similarities. The main differences are the use of multiple lasers, with the ability to use two

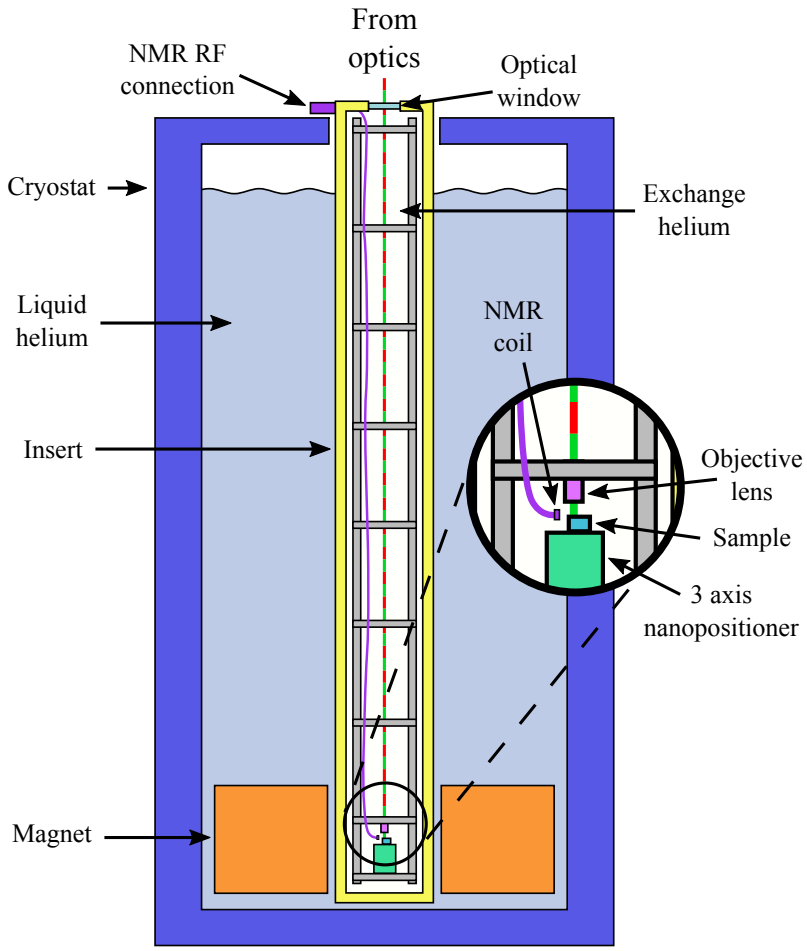

Figure 3.5: Representative schematic of the bath cryostat system. The inset shows a zoomed in view of the sample, objective lens and NMR coil. Some of the wiring, ports and aluminium blocks have been omitted for clarity.

concurrently, polarising optics and automated power and beam control. The optical setup is schematically shown in figure 3.6. There are two separate beams on the left hand side of

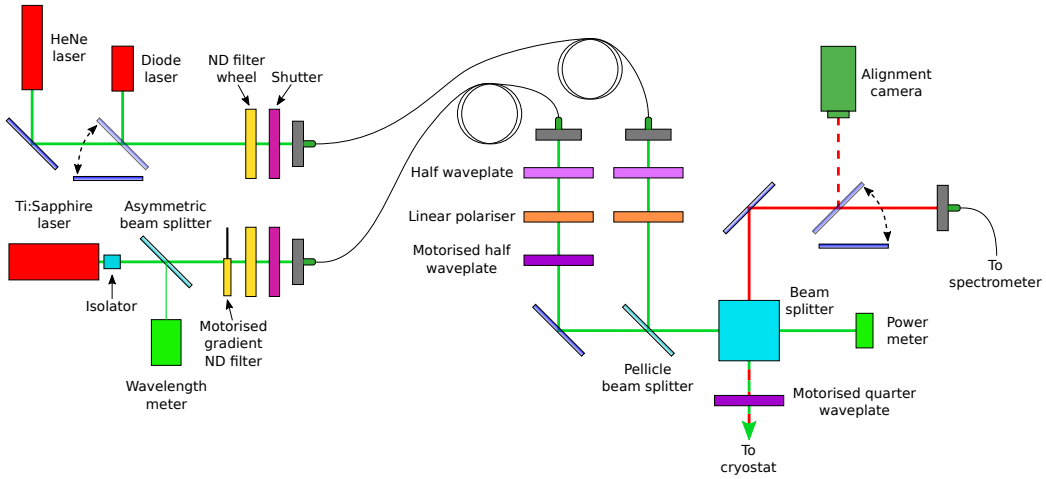

Figure 3.6: Schematic diagram of the optics used for the bath cryostat system. These optics are physically separated, with optical fibres, shown in the middle of the diagram, connecting the two parts together. The pump laser for the titanium-sapphire laser and some mirrors have been omitted for clarity.

the figure, which are referred to as the probe and pump arms. The probe arm contains the helium-neon (HeNe) gas laser and a $650\,\mathrm{nm}$ diode laser, with one of them being selected by a flippable mirror. The laser light from one of these passes through a neutral density (ND) filter wheel, which allows the power to be controlled, and then a mechanical shutter, which can be remotely controlled, into a single-mode fibre. The pump arm contains a tuneable titanium-sapphire laser, which has an optical isolator directly in front of its output – this prevents reflections from the optical elements in the beam from entering the laser cavity and destabilising the laser. An asymmetric beam splitter then redirects part of the light and directs it towards a wavelength meter. The rest of the light continues to a motorised gradient ND filter and then, like the probe arm, a ND filter wheel, a mechanical shutter and into a single mode fibre. These two fibres carry the laser light to an optical breadboard that is mounted on top of the cryostat's insert.

The light, in both of the arms, then passes through separate half-waveplates and linear polarisers. This is done so that the light in both of the beams have a consistent orientation, with the angle of the linear polarisers being fixed and the half-waveplates being rotated to optimise the throughput. The light in the pump arm then passes through a motorised half-

waveplate and then the light from both the pump and probe arms is combined using a pellicle beam splitter. The light then enters a non-polarising broadband cube beam splitter where half is directed onto a power meter, with the other half being directed into the insert via a motorised quarter-waveplate. The quarter-waveplate converts the linearly polarised light into circularly polarised light, with the orientation being determined by the motorised half-waveplate. A motorised half-waveplate for the probe arm is not required as the light's energy is high enough that the polarisation of the electron it produces in the sample is lost before the electron reaches the dot ground state. Inside the insert, the light is focused onto the sample by an objective lens.

Light emitted by the sample follows the same path (but in reverse) with its circular polarisation being converted to a linear polarisation by the quarter-waveplate. This light passes through the beam splitter and is then either directed into a camera used for alignment or a fibre coupler, with the fibre being connected to a spectrometer. This spectrometer, for the majority of the experiments, is a double spectrometer which has a liquid nitrogen cooled CCD camera and an additional mechanical shutter fitted at its input, but the fibre can also be connected to the same spectrometer that is used in the continuous flow system.

3.2.1 RF generation

For NMR, an RF signal needs to be applied to the coil shown in figure 3.5. This is generated by the circuit shown schematically in figure 3.7. A carrier is modulated by the RF signal

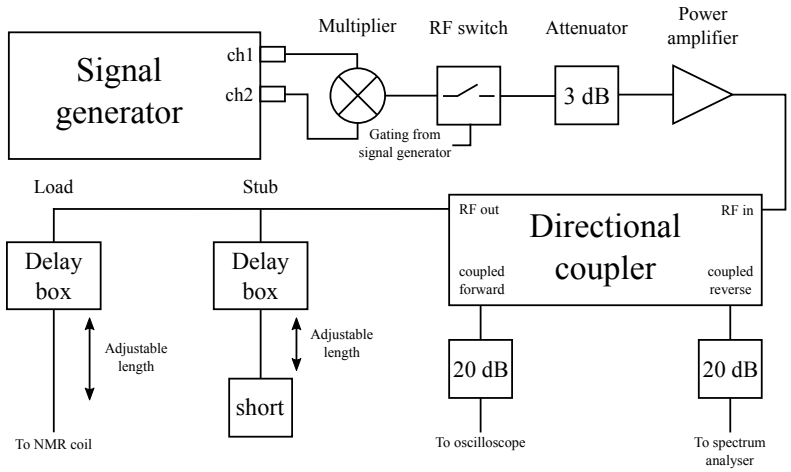

Figure 3.7: Schematic diagram of the RF circuit. All connecting lines represent $50\,\Omega$ coaxial cabling.

so that it is resonant with the desired isotope(s). As this cannot be achieved in the signal generator, an RF multiplier, or mixer, is used, which results in two spectral images of the signal. Whilst the signal generator can be triggered quite accurately, to ensure that the RF signal is only produced when required the signal is passed through an RF switch which is gated by an additional signal generator. The signal is then amplified to the required level for driving the coil by a power amplifier (an attenuator is again used to reduce the gain). The power amplified signal is then passed through a directional coupler which samples a small proportion of the signal (in our case $20\,\mathrm{dB}$). This allows both the forward and reflected power to be measured, with an oscilloscope and a spectrum analyser being used, respectively. The forward power is purely for monitoring the power being transmitted to the RF coil in the cryostat, and so an oscilloscope is used. The reflected power is used to determine the matching of the RF circuit as well as being used to verify that the correct waveform is being transmitted, hence the use of a spectrum analyser. As the coil is essentially an inductor, it has an almost entirely reactive impedance that is dependant on the driving frequency, rather than the $50\,\Omega$ characteristic impedance of the RF circuit. To avoid excessive reflections, that could damage the power amplifier as well as resulting in only a small emission from the coil, a matching circuit is used consisting of an adjustable length shorted stub and an adjustable path length connecting the circuit to the coil. The stub, ignoring transmission line loses, presents a reactive impedance that is tuned so that it cancels the reactive impedance of the coil, with the adjustable length of the path to the coil being used to match the resistive part of the coil and circuit to the characteristic impedance ($50\,\Omega$). The majority of the adjustable length is achieved through the use of delay boxes, which allow a delay of between 0 and $63.5\,\mathrm{ns}$ in $0.5\,\mathrm{ns}$ steps[1], with small changes being achieved through the addition of extra connector type converters (e.g. BNC to SMA) or adapters (e.g. male to female). The matching is achieved by generating a broadband noise signal at low power and looking at the reflected spectrum on the spectrum analyser, the length is then manually tuned until an adequate dip in the reflection spectrum at the desired frequency is found, an example of this is shown in figure 3.8. This dip in the reflection, shows that the coil is absorbing the power at that frequency and is therefore both matched to the RF circuit as well as efficiently emitting the signal. For some experiments, it is necessary to match the RF circuit and coil for multiple frequencies to allow

[1]The delay boxes internally consist of RG58A/U cabling connected with switches between two connectors.

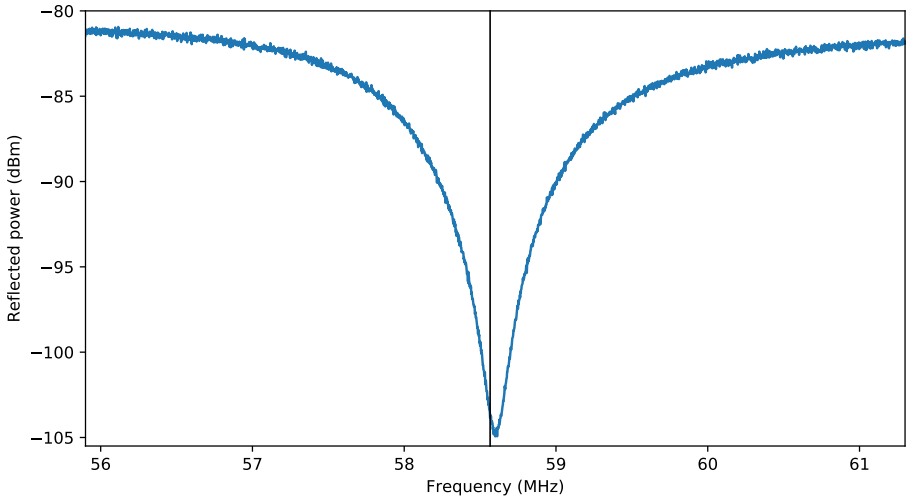

Figure 3.8: Reflection spectrum of the RF circuit and coil matched for $^{75}\mathrm{As}$ at $8\,\mathrm{T}$ (the resonant frequency is shown with the black vertical line).

the manipulation of multiple isotopes at the same time, this can be achieved by increasing both the lengths (i.e. of the stub and the connection to the coil). An example of this is shown in 3.9. It should be noted from this figure that not only are the dips in the spectrum smaller

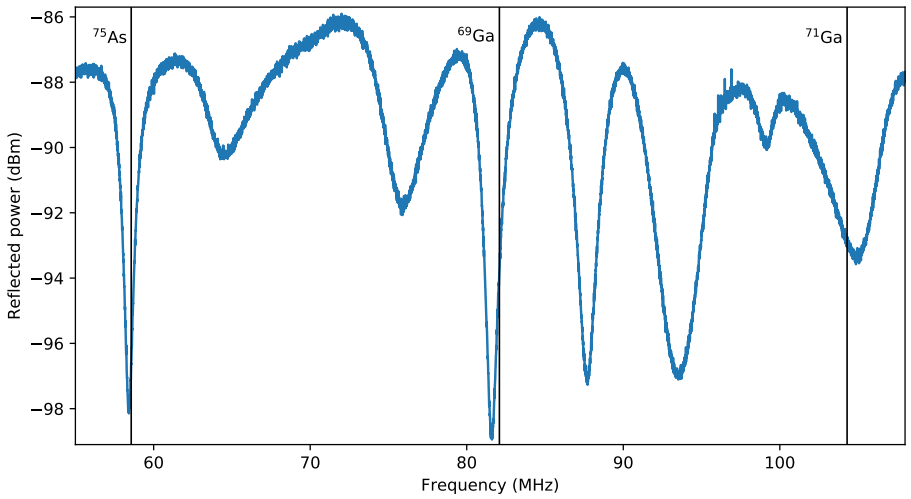

Figure 3.9: Reflection spectrum of the RF circuit and coil matched for three isotopes at $8\,\mathrm{T}$.

than those for a single isotope, but the alignment to the resonant frequencies of the isotopes is worse. This is unfortunate but cannot be avoided and results in less power being dissipated in the coil, particularly in figure 3.9 where the dip for $^{71}\mathrm{Ga}$ is noticeable worse than the other isotopes and substantially worse than that of a single isotope. To produce the same effect in the sample, either the length or the amplitude of the RF pulse can be increased.

3.2.2 Pump-probe technique

As was previously described in section 2.5, the repeated injection of spin polarised electrons into a quantum dot results in the polarisation of the nuclear spins that surround the dot. This results in an additional effective magnetic field (the Overhauser field) that will increase, or decrease, the splitting between the exciton spin states. This can be observed in PL as a change in the splitting of the X^0 transitions and an example of this is shown in figure 3.10. Any change in the local nuclear spin population that affects the Overhauser field will

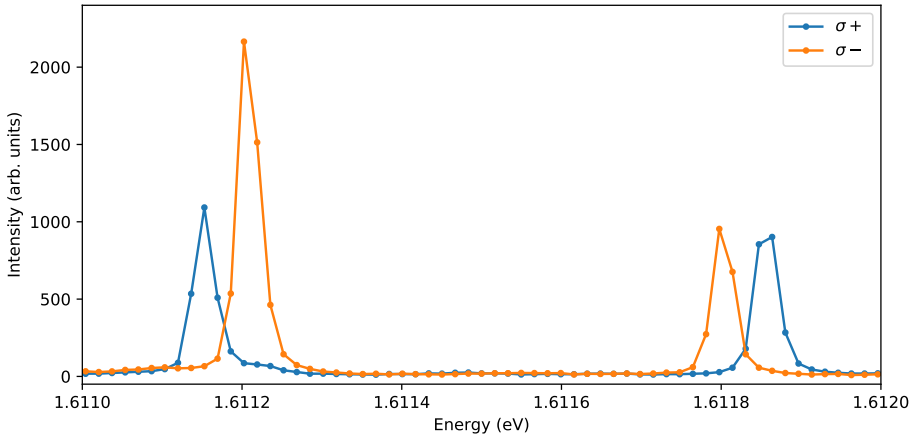

Figure 3.10: PL spectrum of a quantum dot's X^0 transitions, at $8\,\mathrm{T}$, under opposite circularly polarisations of a $1.643\,\mathrm{eV}$ laser, resulting in an Overhauser field of opposite signs. The dot's transitions with a zero Overhauser field will approximately be in the middle of the two polarisations.

result in a change in the splitting, making the quantum dot's transitions an excellent probe of the nuclear spin system. In figure 3.10, the laser that is producing, or pumping, the polarised nuclear spins is the same that is being used for excitation when detecting the PL. This results in a high degree of nuclear spin polarisation as any polarisation that is lost is quickly replaced, resulting in a steady state. Whilst this is a very good method for spin preparation, any changes to the nuclear spin system that are due to the experiment will be lost during the time it takes to acquire the spectrum. Using a laser with significantly higher photon energy, where the spin polarisation of the electron is lost before it reaches the dot, to probe the spin states suffers from an opposite problem, where the decaying of the nuclear spins would interfere with the acquisition of the spectrum (admittedly over a longer time period). In both of these cases, the solution is to reduce the time that the dot is exposed to

the probing laser, but this drastically decreases the detected PL signal. However, this can be increased to an adequate signal to noise ratio by acquiring the spectrum over several cycles of preparation, modification and detection, with the resulting spectrum indicating the average nuclear spin state. A schematic example of one of these cycles is shown in figure 3.11. The

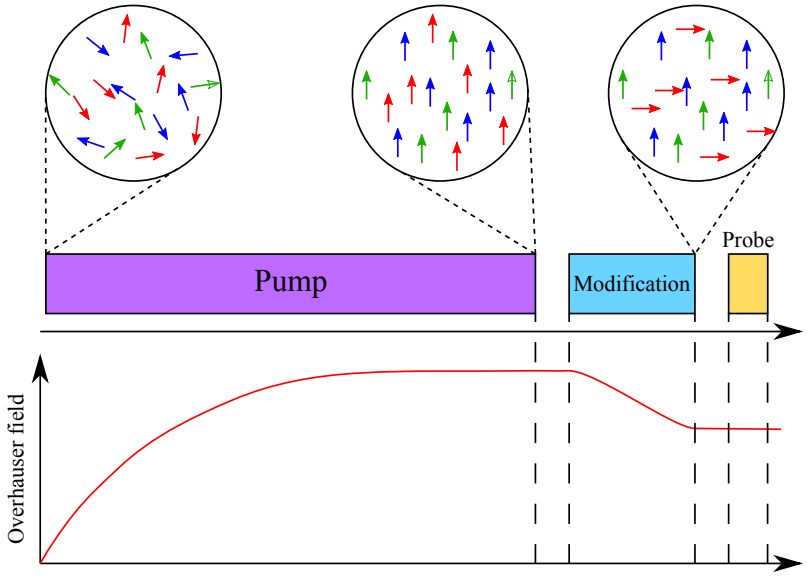

Figure 3.11: Representative schematic of the pump-probe cycle, with the direction of the nuclear spins (of three isotopes) shown at the top and the general effect on the resulting Overhauser field shown at the bottom. The modification in this instance represents the depolarisation of one of the isotopes.

modification of the nuclear spins is either due to an RF signal or the inherent evolution of the spins.

3.3 Strained samples

Stressed samples were required for the gradient elastic tensor experiments, with the compressive stress being applied in two different directions (relative to the sample). This was achieved through the use of two different styles of mechanical clamps, shown in figure 3.12. The first clamp, shown in figure 3.12a, had the sample glued between the open jaws of the titanium bracket. By tightening the bolt, the sides of the bracket were pushed closer together creating a compressive stress along the sample's $[1\,1\,0]$ direction.

The second style of clamp, shown in figure 3.12b, used a titanium bracket that had a small hole drilled through the top of it. The sample was then glued to a piece of sapphire and

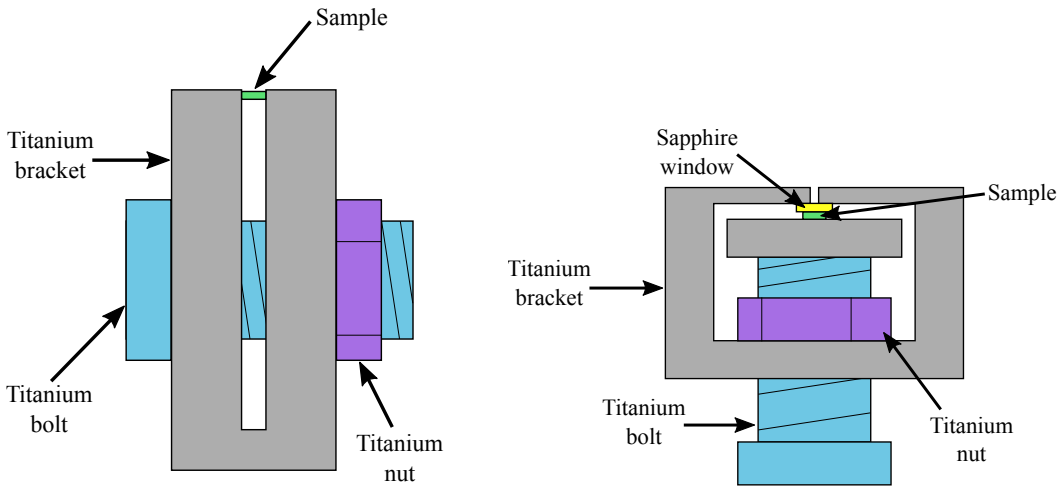

(a) $[1\,1\,0]$ direction (b) $[0\,0\,1]$ direction

Figure 3.12: Representative diagrams of the clamps used to apply compressive stress to the samples.

then underneath the hole in the top of the bracket. This allowed the sample to be stressed along its $[0\,0\,1]$ direction whilst allowing PL to be detected (which is emitted along the same direction), as the sapphire window spreads the force across the surface of the sample whilst being transparent.

3.3.1 Finite element modelling

Whilst the clamps are designed to apply the stress to the sample as uniformly as practical (whilst also keeping the clamps small enough to fit into the cryostat), the applied stress will not be perfectly uniform. To understand the nature of the applied stress, the clamps and samples were modelled using finite element modelling in the COMSOL Multiphysics software package, using simplified models of the clamps.

In the case of the $[1\,1\,0]$ clamp, the titanium bolt and nut were not modelled, instead a constant pressure was applied to the faces that the bolt head and nut are in contact with. Whilst this results in a different distribution of the pressure on the sides of the titanium bracket in contact with the head of titanium bolt and the nut, the distribution of the pressure on the sample is the same.

In addition to this, the glue was not modelled, as the amount used was small and its distribution is not known, and both the surfaces of the sample and titanium bracket were

modelled as being perfectly smooth. The sample was also modelled as a homogenous piece of GaAs, rather than having the same structure as the sample, as the layers are much smaller than the cell size of the mesh.

For the $[0\,0\,1]$ clamp, only the sample, sapphire window and the titanium block in contact with the sample were modelled. A constant pressure was applied to the faces of the sapphire window and titanium block opposite to those in contact with the sample. It was not necessary to model the titanium bracket that applies the pressure to the sapphire window as the combination of a small aperture in the titanium bracket, the use of a hard material (sapphire) and the dimensions of the sapphire window meant that the pressure applied by the sapphire window to the sample is equivalent to a constant pressure being applied to the sapphire window.

For both clamps, the glue and surface roughness of the materials were not modelled. Adding these to the models would introduce local variations in the sample's strain. This is unnecessary for our use case as we are modelling the general effects on the sample rather than trying to precisely model a specific sample being strained.

3.4 Confidence intervals for multi-parameter models

Typically the confidence intervals for the parameters of a fitted model are estimated using the standard error derived from the covariance matrix that most fitting software will produce. These confidence intervals will be symmetrical about the fitted value, due to an inherent assumption that the residuals are Gaussian distributed about zero, which is only true for a limited set of models. A more reliable method of estimating the confidence interval can be achieved through using the χ^2 value.

The fitting algorithm will result in the sum of the squared residuals, i.e. the squared difference between the data and the fitted model, being at a minimum. This can be used with the number of degrees of freedom the model has to calculate the χ^2 value of the fit. If we then vary the fitted parameters we can find those that increase the χ^2 value by our desired level of confidence. In the case of a two parameter model, this will result in a set of parameters that form an ellipse when plotted against each other with the fitted parameters being inside and

the extents of the ellipse for each parameter indicating the parameter's confidence interval [40].

For n parameters, this results in a n dimensional hyper-ellipsoid whose boundary becomes significantly more difficult, and computationally expensive, to determine. Instead we use a Monte Carlo approach where we randomly perturb the parameters (or equally, randomise each parameter within a certain range) keeping any set of parameters that has a χ^2 value that is lower than the combination of the fitted χ^2 value and our desired level of confidence. This, with a large number of found parameter sets, can be used to approximate the boundary of the hyper-ellipsoid, providing that the perturbation of the parameters, or the allowed parameter range, is large enough to not truncate its boundary.

Chapter 4

Schottky diodes for optical experiments

This chapter details the fabrication of Schottky diode charge control structures for use in optical experiments and concludes with a preliminary photoluminescence study on how different tunnelling barrier thicknesses affect the emission from the quantum dots.

4.1 Background

A Schottky diode has a diode characteristic due to a metal-semiconductor junction, where the difference of the work functions of the metal and semiconductor materials results in a potential barrier in the conduction band (called a Schottky barrier). This barrier, under forward bias, allows current to flow, whilst under reverse bias only allows a small leakage current to flow, unless the bias is large enough that the barrier breaks down. In its simplest form, a Schottky diode consists of a metal wire pressed against a semiconductor substrate – which was the first manufacturing technique used (in 1904 [41]) – however, significantly more reliable methods are now used with the most common depositing the metal onto the semiconductor material in a vacuum. This provides a more consistent and reliable contact, providing that the surface of the semiconductor is clean enough for the metal to adhere, being free of contaminants and not being heavily oxidised[1].

Commercial Schottky diode manufacturing usually involves more complicated designs than a simple metal-semiconductor junction, for example with the use of guard rings and

[1] Oxidisation is inevitable and can result in an additional potential barrier; however, the effect of this can be negated by annealing the deposited contact.

oxide isolations, to create diodes with very specific qualities – such as low leakage currents or reduced capacitance [41]. However, a Schottky diode for charge control does not need to have the same level of perfection, or characterisation, as commercial diodes. The only requirement is that the current-voltage (I-V) characteristics allow an electric field to be held across the dots with as little current flowing through the diode as possible. Practically, this requires that the turn on and breakdown voltages are well separated (typically greater than $5\,\mathrm{V}$) and that the leakage current is small (typically less than $1\,\mu\mathrm{A}$). From an experimental point of view, it is beneficial to be able to change the charge population of the dot quickly, which puts an upper limit on the diode's capacitance. However, the frequencies used in experiments are, at most, a few hundred kHz, which essentially means that no special considerations need to be made.

4.2 Schottky diode sample fabrication

The Schottky diodes are fabricated on the grown quantum dot structures using several stages of photo-lithography. This was chosen over other methods, namely electron beam lithography, as the mask set does not change, the resolution required is well within the range of photo-lithography and photo-lithography is significantly quicker. There is also the potential problem that electron beam lithography can cause damage to the crystal.

Two different mask sets have been used for fabricating the Schottky diodes, with the fabrication process being the same for both masks. The n-layer, which is below the quantum dots, is reached by wet-etching, with a contact being deposited onto the etched region using thermal evaporation. This contact would then be annealed, allowing the metal to diffuse slightly into the doped material, to ensure a good contact. A thin titanium layer, designed to act as an electrically conducting window, would then be deposited (either through thermal evaporation or sputtering) on to the non-etched region, with top contact being added to complete the structure (see figure 4.1). The difference between the two mask sets is the location of the lower contacts. In the first set, which we shall refer to as the legacy mask set, the etched region was a narrow trench directly next to the diode mesas[2]. Whilst working diodes were produced using the legacy masks, they were fairly rare and would frequently

[2]Mesas (hills) are frequently used to refer to the non-etched regions.

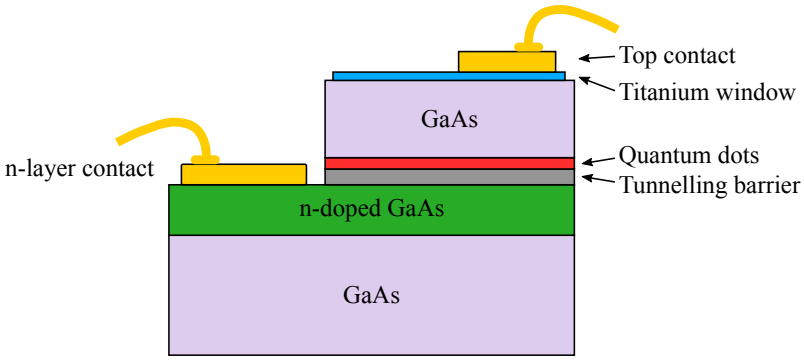

Figure 4.1: Representative schematic of the legacy mask set. The DBRs have been omitted for clarity.

break during thermal cycling (i.e. cooling to cryogenic temperatures and then heating back to room temperature). A cause of these failures was determined to be the metal deposited for the lower contact filling up the etched trench to such an extent that it would short, or partially short, the diode structure, resulting in no electric field being applied across the dot layer.

To remedy this, a new mask set, which we will refer to as the new mask set, was designed where the lower contact is separated from the mesas by $130\,\mu\mathrm{m}$, removing the possibility of shorting the dot layer. However, this requires that the entire sample, with the exception of the mesas, is etched, which results in the etch depth being critical, as any reduction in the thickness of the n-layer decreases the conductivity up to the point where the n-layer can no longer conduct. The initial processing run using the new mask produced working diodes, with some failing. However, subsequent processing runs were not able to produce electrically working diodes. The cause of this was the inheritance of the legacy mask's processing protocol.

As the legacy mask used an etched trench, the target depth for the etch was halfway into the n-layer. This was designed so that when the metal for the contact was deposited it would fill up the trench, resulting in no loss in conductivity for the n-layer. With the new mask, etching halfway into the n-layer, as noted above, is detrimental but should still produce electrically working diodes. However, AFM images of a working diode from the first processing run with the new mask set showed an over-etch at the edges of the mesas. This is shown in figure 4.2, where the measured depth (relative to the top of the mesa) is deeper at approximately $11.5\,\mu\mathrm{m}$ than the rest of the etch (e.g., $>13\,\mu\mathrm{m}$). Such an over-etch increases the etch depth from approximately $30\,\mathrm{nm}$ into the $92.2\,\mathrm{nm}$ n-layer to around 60 to

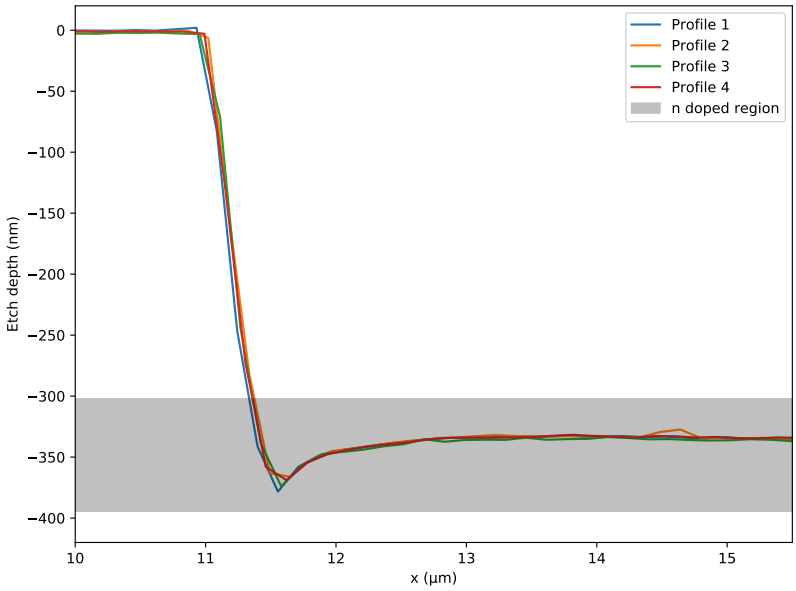

Figure 4.2: AFM of the edge of a mesa on a working sample (SF1109), with multiple profiles being taken along the same edge of the mesa. The grey shaded area shows the location of the n-doped layer in the sample.

70 nm, which helps to explain why only some of the diodes from this processing run worked (as there is a variation in etch depth across the sample) and potentially why other processing runs failed, particularly if the target etch depth was reached. The processing protocol was changed so that the target etch depth was at the top of the n-layer or just above it, which consistently produced electrically working diodes; however, they were unable to tune the quantum dots.

4.2.1 Connecting to the n-layer without etching

A diode that works electrically but cannot tune quantum dots, means that the diode is not applying an electric field across the dot layer, which can have two possible causes – either the dot layer is being shorted or the thin titanium window is not spreading the electric field.

To investigate this, the etching step was replaced with annealing. Annealing, the process of heating a sample to a high temperature and then cooling it, allows two materials to diffuse across the boundary that connects them. This is frequently used to control dopant levels in semiconductor devices, but the vast majority of materials will diffuse across a boundary [42]. As mentioned when describing the fabrication protocol, annealing is used to diffuse the metal of the lower contact into the semiconductor material, to ensure that a good electrical

connection is made. However, the time and temperatures used for this have been inherited through different protocols, with the depth of the diffusion not being known.

Diffusion in semiconductors is normally modelled using Fick's laws, namely the first law,

$$\mathbf{J} = -D\nabla C, \tag{4.1}$$

where $\mathbf{J}$ is the flux of atoms and C is the concentration at the same point, and D is the diffusion coefficient; and the second law,

$$\frac{\partial C}{\partial t} = \nabla \left(D\nabla C \right), \tag{4.2}$$

where t is time [42]. With the appropriate boundary conditions, a solution can be found that is applicable to the diffusion of a metal contact into a semiconductor – the diffusion from a finite layer, of thickness h, into a semi-infinite sample,

$$C\left(x,t\right) = \frac{C_0}{2}\left(\operatorname{erfc}\frac{x-h}{\sqrt{Dt}} - \operatorname{erfc}\frac{x+h}{2\sqrt{Dt}}\right), \tag{4.3}$$

where C_0 is the initial surface concentration, x is the distance into the sample[3] and erfc is the complementary error function [43]. The diffusion coefficient is dependent on both the material of the layer and of the sample, but also has an exponential dependency on temperature.

The lower contact, in the protocol, consists of two layers – $20\,\mathrm{nm}$ of indium-germanium (InGe) and $200\,\mathrm{nm}$ of gold, with the InGe being used as the gold will not adhere directly to the sample (due to oxidisation). Gold is known to be a rapid diffuser in III-V compounds and has a diffusion coefficient that is significantly greater than both In and Ge in GaAs [43]. However, the In content of the InGaAs SAQDs will also diffuse, which will affect their properties. To mitigate this, a lower temperature can be used, resulting in only the gold diffusing. The majority of diffusion studies, and certainly those for gold, are conducted at fairly high temperatures – for example 740 to $1020\,^{\circ}\mathrm{C}$ [43]. This means that the diffusion coefficient for gold is not known for the lower temperature ($320\,^{\circ}\mathrm{C}$) being used. In addition to this, the sample is not as simple as the schematic shows in figure 2.7a, with DBRs being placed at the top and bottom of the sample to increase efficiency (see section 3.1). Both of

[3]Zero being the boundary between the sample and the layer, and negative values being in the finite layer.

these complicate modelling the diffusion of the contact into the sample. However, a simple model will be largely representative of the annealing process.

The n-layer in the samples is typically between 300 to $500\,\mathrm{nm}$ below the surface, with the metal contact containing approximately $200\,\mathrm{nm}$ of gold. Intuitively, this amount of gold would be a poor choice and this is confirmed by the model, see figure 4.3. Here the gold layer

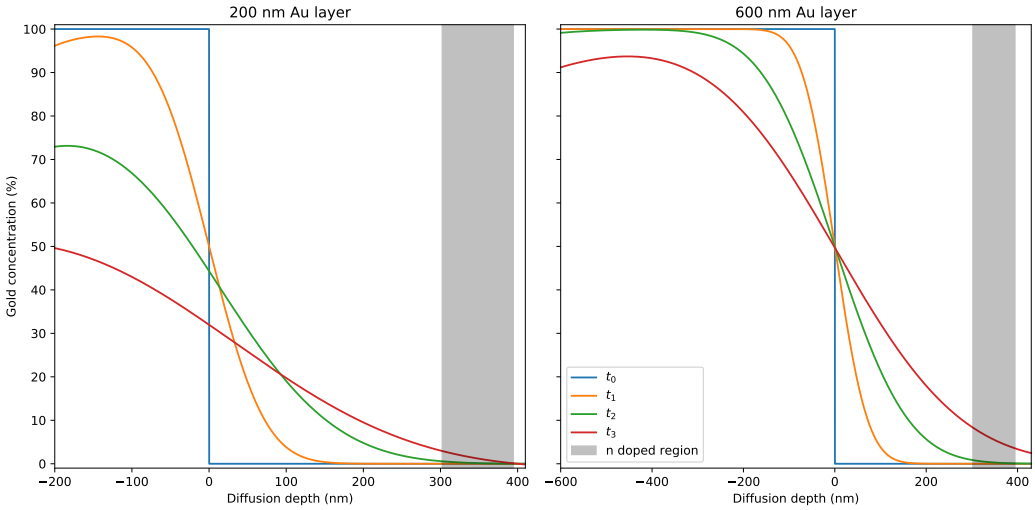

Figure 4.3: Profiles of gold diffusing from a layer into GaAs at several time points ($t_0 = 0$ and $t_0 < t_1 < t_2 < t_3$). The shaded region represents the depth of the n-layer, with negative depth values representing the region of the gold layer.

becomes significantly depleted of gold with only a small proportion reaching the buried n-layer. Whilst this would work, at least to a limited extent, the lack of gold in the contact would make it very difficult to bond to and the resistance of the resulting diode would likely be high. Figure 4.3 also shows the same model with a $600\,\mathrm{nm}$ layer of gold, with a reasonable proportion diffusing into the n-layer without an excessive loss of concentration in the gold layer.

Whilst it is possible to model the diffusion profile, it is difficult to measure it in the Schottky structured samples. The parameter that ultimately matters is the resistance and, therefore, it is necessary to know how the resistance will change as the gold diffuses through the sample. This is shown in figure 4.4 and is fairly intuitive – the resistance exponentially decreases to a minimum and then will gradually increase if the diffusion is allowed to continue. Thicker layers of gold result in a lower resistance being achievable; however, whilst the size of the minimum increases (in terms of annealing time), increasing the thickness of

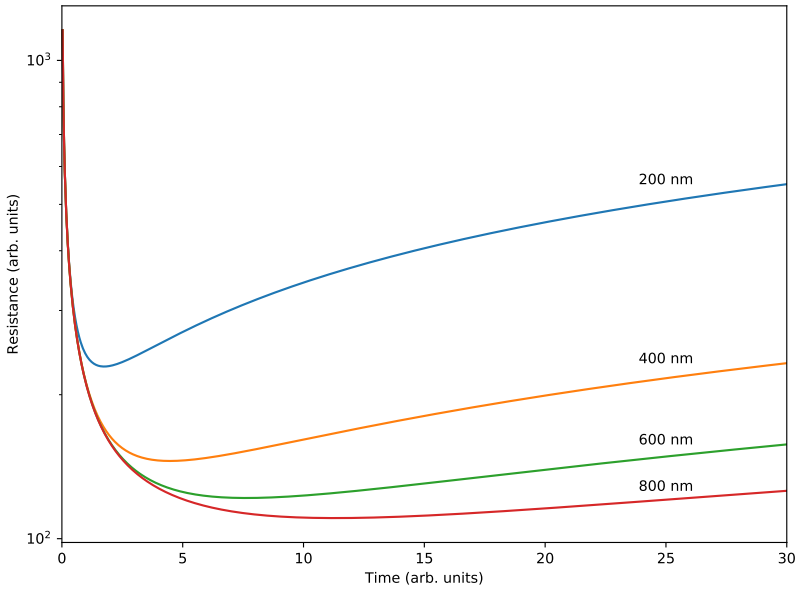

Figure 4.4: Modelling of the sample's resistance during the annealing process with different thicknesses of the gold layer.

the gold layer repeatedly has a diminishing return. From a practical point of view, depositing large amounts of metal using thermal evaporation can cause issues, so a thickness of $600\,\mathrm{nm}$ was chosen for the gold layer.

To determine the required time for the gold to diffuse to the n-layer, a sample, containing dots with undesirable characteristics, had the lower contact deposited on it, with the thickness of the gold layer being increased to $600\,\mathrm{nm}$. The sample was then cleaved to electrically isolate areas of the contact, so that I-V measurements could be taken, with the current flowing from a contact on the surface, through the diffused gold, to the n-layer and then back to a different contact. The sample was then repeatedly annealed, allowing the gold to diffuse. The results of this, shown in figure 4.5, largely follow an exponential decrease in the resistance, as is expected. There is a jump in the resistance due to different heating profiles of the rapid thermal annealer (RTA), where the time taken for heating between $200\,^\circ\mathrm{C}$ and $320\,^\circ\mathrm{C}$ (the rise time) changed from 30 to $60\,\mathrm{s}$, effectively increasing the annealing time. There are some deviations from an ideal curve that are likely due to the sample's structure, heating consistency and uniformity of the RTA, as well as additional resistance from the measurement probes which is unlikely to be constant for each measurement. Once the resistance appeared to reach a minimum, the annealing was stopped, so any increase in the resistance

(a)

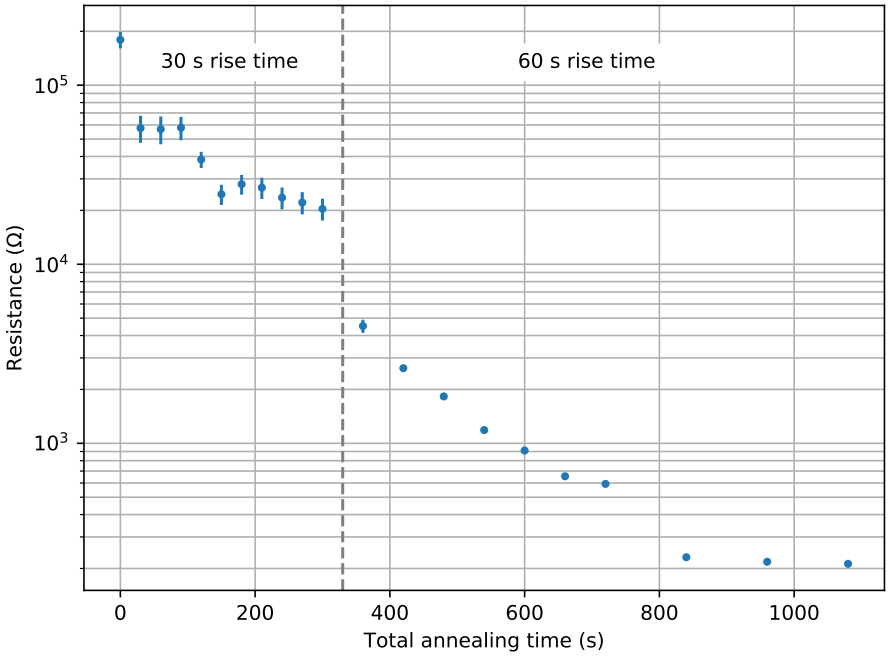

(b)

Figure 4.5: Investigation of the contact diffusion time. (a) shows the position of the measurement points on the sample (red ellipses), (b) shows the resistance versus the annealing time.

after the minimum was not seen. The total annealing time, i.e. the time the sample was held at $320\,°\mathrm{C}$, was $18\,\mathrm{min}$.

Using this approach for the lower contact resulted in electrically working diodes that had more consistent turn on voltages and generally larger breakdown voltages than those produced with the same wafer but using etching. However, these diodes were unable to tune the dots and therefore ruled out the possibility of any metal shorting the electric field across the dot layer.

4.2.2 Thin titanium window

There are only two possible reasons why the titanium window would not be spreading the electric field across the dots – either it is not electrically connected to the contact or the layer itself is non-conducting. High resolution microscopy, namely AFM and SEM, was performed on the non-tuning diodes; however, these did not show any reason why the diodes could not tune the dots, e.g. a trench or gap in the titanium layer. When using the SEM, energy dispersive X-ray spectrometery (EDX) was also performed – which is where characteristic X-rays, produced by the sample interacting with the electron beam, are detected. The penetration depth of the beam depends on the beam's energy, with the used $3\,\mathrm{kV}$ beam penetrating approximately $100\,\mathrm{nm}$, making this technique quite surface sensitive. Figure 4.6 shows the results of this, with two measurements of both a tuneable and non-tuneable diode (shown in different colours). These measurements were on the titanium window (continuous lines) and on the sample's surface away from the diodes (dashed lines) – for the tuneable diode this is a measurement of the etched n-layer and for the non-tuneable diode this is the top of the sample's structure. The dashed lines can be considered as a background measurement for the samples, which is particularly important for the oxygen peak, as the samples can be easily contaminated by atmospheric oxygen after the sample has been fabricated. The titanium peak for the non-tuneable diode is larger than the tuneable diode, which is to be expected as approximately $40\,\%$ more was deposited. However, the oxygen peak increases by a factor of approximately 2.6, which is not expected. As the measurements of the titanium windows were taken away from its edges, it was expected that the oxygen content would be similar as only the surface of the titanium should be oxidised. In addition to this, titanium oxidises quickly, with the surface becoming completely oxidised in a matter of minutes. So

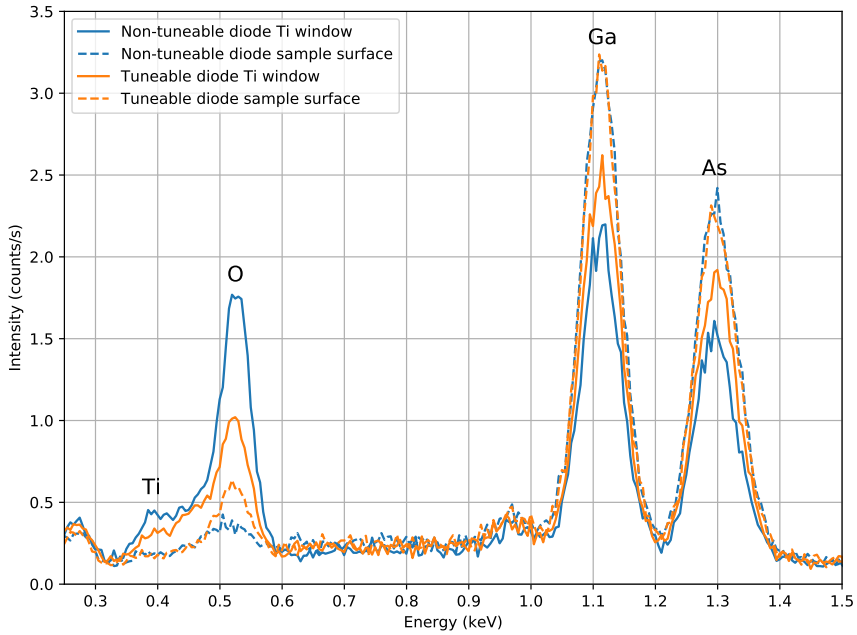

Figure 4.6: EDX of the tuneable and non-tuneable samples with a $3\,\mathrm{kV}$ electron beam. The peaks are labelled with their associated elements.

any differences between the samples should not be due to when the diodes were fabricated. Even if this was not the case, with the oxidation taking significantly longer, as the tuneable diode had considerably longer to oxidise, it would be expected that the oxygen peak for the non-tuneable diode would be much smaller than the tuneable diode, not what was observed. This suggested that there might be an issue with the titanium deposition.

The metal for the contacts is deposited by thermal evaporation, with the inherited protocol using sputtering for depositing the thin titanium window. Thermal evaporation deposits metal by heating a coil of the desired metal so that it melts, evaporates and then condenses on the sample, with the deposition rate and the total amount of material deposited being difficult to accurately control. Sputter deposition accelerates argon ions into a target, causing some of the atoms to be ejected onto the sample. Unlike thermal evaporation, this is more controllable and is highly repeatable, making it significantly easier and more accurate for the deposition of thin films.

A comparison between the two deposition methods was made, with $20\,\mathrm{nm}$ of titanium being deposited on to glass microscope slides. These films were then measured using X-ray reflectometry (XRR), a surface sensitive measurement technique that is able to characterise thin films, determining their thickness and density, amongst others. This showed that the den-

sity of the thermally evaporated sample was very close to that of bulk titanium, $4.59\,\mathrm{g\,cm^{-3}}$ (approximately $102\,\%$ of the bulk value); however, the density of the sputtered sample was significantly lower at $3.75\,\mathrm{g\,cm^{-3}}$ (approximately $83\,\%$ of the bulk value), which is very close to that of anatase, a form of titanium dioxide, whose density is $3.8\,\mathrm{g\,cm^{-3}}$ [44]. A set of diodes were then fabricated using thermal evaporation, instead of sputtering, for the deposition of the titanium window. These were able to tune the quantum dots, isolating the issue in the diode fabrication to a fault with the sputter deposition system. However, with thermal evaporation being less controllable and repeatable than sputtering, and the diodes requiring a thin titanium window for optimal light transmission, the deposition technique required optimisation.

4.2.3 Optimisation of thermal deposition of thin titanium films

The purpose of the thin titanium window is to spread the electric field across the dots, whilst still offering optical access to the dots. It therefore needs to have a fairly high optical transmittance as well as a low electrical resistance. Unfortunately, these two parameters are conflicting – a high optical transmittance will be from a very thin film that will have a high resistance and a low resistance will be from a very thick film that has poor optical transmittance. There will, however, be a compromise between the two parameters which will be optimum for the diodes.

With titanium oxidising quite rapidly, it is beneficial for it to be deposited in a high quality vacuum. The thermal evaporation system used typically can reach a vacuum pressure of $10^{-6}\,\mathrm{mbar}$, with a noticeable drop in the vacuum pressure when the titanium starts to evaporate, which is less than ideal. Consequently, the deposition rate is an important parameter to control, with slower rates allowing more time for oxidation; however, faster rates shorten the window in which the shutter can be manually closed and achieve the desired thickness.

To determine the optimum parameters, as well as the best deposition technique, a series of depositions onto glass microscope slides were carried out, with the thickness being intentionally varied as well as the deposition rate. The electrical resistance of the titanium was measured across the width of the glass slides in small steps with the highest and lowest values being recorded. The transmittance of the film was measured with an ellipsometer, with measurements of a clean glass slide being used as a control. The results of this are

show in figure 4.7. One deposition was conducted with a very low deposition rate, this is not

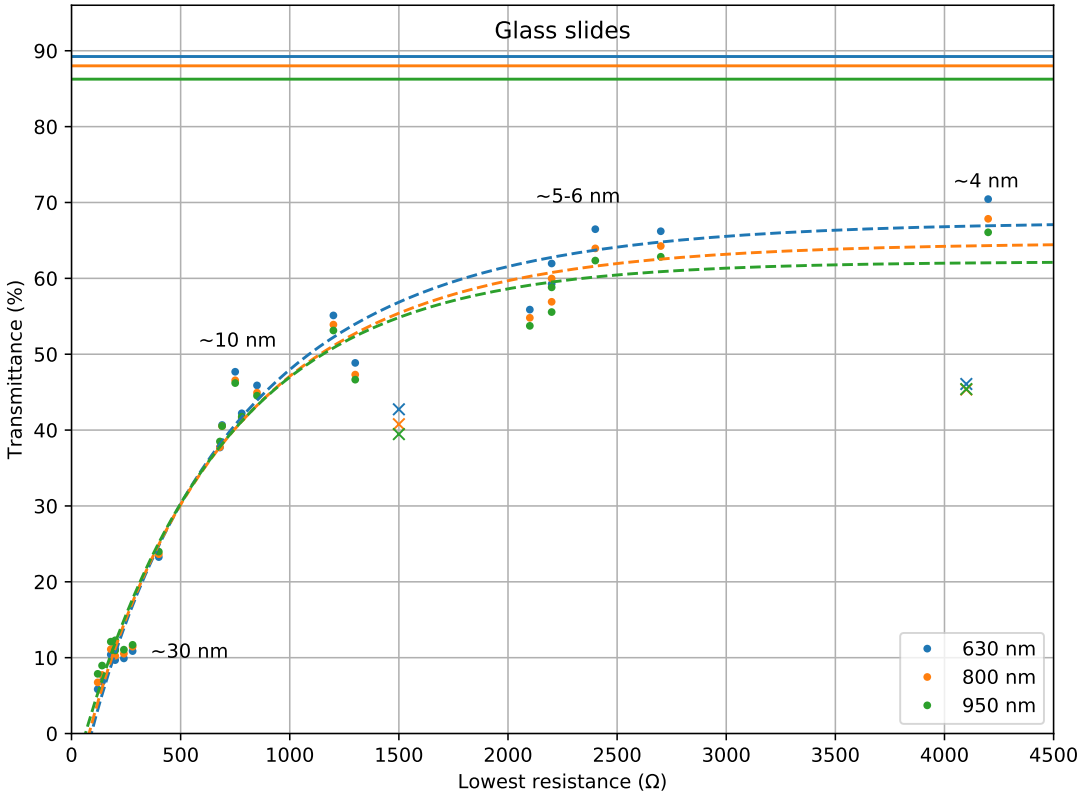

Figure 4.7: Optical transmittance of thermally evaporated titanium onto glass microscope slides versus the resistance across the width of the slide. The continuous lines at the top of the graph are the transmittance, at the different wavelengths, for a glass slide without any deposited titanium. Annotations on the graph are of the approximate thickness values. The data points represented by crosses are for evaporations at lower deposition rates.

shown in figure 4.7 as the resistance was approximately $50\,\mathrm{k\Omega}$ for a film of $40\,\mathrm{nm}$. It had a transmittance between 40 to $45\,\%$ and a significantly lower density of $3.88\,\mathrm{g\,cm^{-3}}$. Whilst this density was not as low as the sputtered titanium, its high resistance shows that a high deposition rate is required to avoid films that are similar to those that were sputtered. Figure 4.7 has fitted curves plotted for the dot data points, which show the general trend of the data. In particular, the transmittance of the films approaches a maximum of around $70\,\%$, with the resistance sharply increasing. Therefore, there is very little advantage to increasing the resistance over $3\,\mathrm{k\Omega}$, with the ideal range being between 1.5 to $3\,\mathrm{k\Omega}$, which has a transmittance of between 55 to $65\,\%$.

4.3 Photoluminescence of InGaAs SAQDs with varying tunnelling barriers

The InGaAs SAQD samples, whose structure is described at the start of this chapter, form a series where the tunnelling barrier thickness is varied to control the tunnelling coupling between quantum dots and the Fermi sea. Larger tunnelling barriers increase the isolation of the dots from the Fermi sea of the n-doped layer, offering the possibilities of increased spin lifetimes. However, this increased isolation also makes it more difficult for an electron to tunnel into the dot, with there being a point where the barrier will be so thick that tunnelling will not be possible. The limiting thickness of the tunnelling barrier is not known, so instead the thickness was stepped by $5\,\mathrm{nm}$ from 37 to $52\,\mathrm{nm}$. Unfortunately, there was an issue with the growth of the $47\,\mathrm{nm}$ sample, so the samples available had tunnelling barriers of 37, 42 and $52\,\mathrm{nm}$. A piece from each of these samples was fabricated into Schottky diodes (using a diffused n-contact and a thermally evaporated titanium layer) and the resulting devices were characterised in the continuous flow cryostat system.

Spatially isolated lines in PL that appeared to be from quantum dots, based on the positional nature of the lines and the effect the bias voltage had on them, were found near the resonant wavelength of the optical cavity. An example of this, for each of the samples, is shown as PL intensity maps with respect to the applied bias voltage in figure 4.8. Whilst

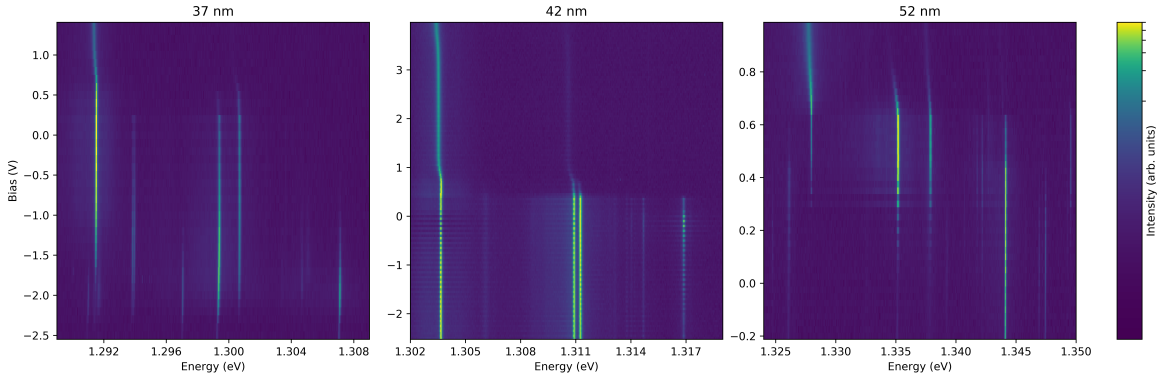

Figure 4.8: Bias PL maps of a quantum dot in each of the three InGaAs samples. The thickness of the tunnelling barriers in the samples is shown above each of the graphs.

it showed tuning of the dot's states, it was necessary to identify the individual states. This was achieved by examining the emission from the states changed with the excitation power

and the polarisation of the emitted light. Figure 4.9 shows a power dependence of a dot's emission intensity, with the spectra being normalised to the excitation power and acquisition time. In this figure, the emissions that are annotated with X^0 and X^{-1} are linear in intensity

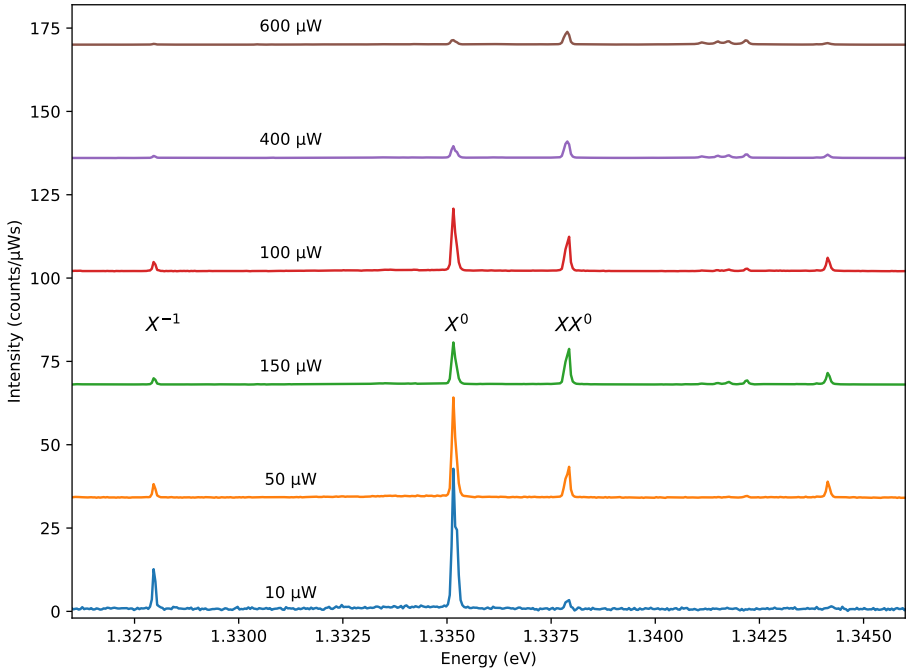

Figure 4.9: Normalised power dependence of a typical dot in the sample with a $52\,\mathrm{nm}$ tunnelling barrier. The spectra are annotated with their excitation power and the dot's lines are annotated with their associated states.

with respect to the excitation power and the XX^0 emission is super-linear in intensity, which allows the XX^0 line to be identified. From their relative positions, the X^0 and X^{-1} lines can be identified [18]. However, as an additional check, the PL was measured with the addition of a rotatable linear polariser being added after the filter and before the fibre coupler, enabling linearly polarised detection of the PL. Two orthogonally polarised PL, for the same dot, is shown in figure 4.10. As discussed in section 2.2.1, singularly charged exciton states (i.e. X^{-1}) do not have a fine structure (as they are spin singlets), but both the exciton and biexciton do have a fine structure producing two orthogonally linear polarised components. These components are split by the same amount for both X^0 and XX^0 but the components are cross polarised, with the lower energy component of X^0 having the same polarisation as the higher component of XX^0 (see figure 2.5). In figure 4.10, X^0 and XX^0 show the expected polarised behaviour and their splittings are within fitting errors of each other. The

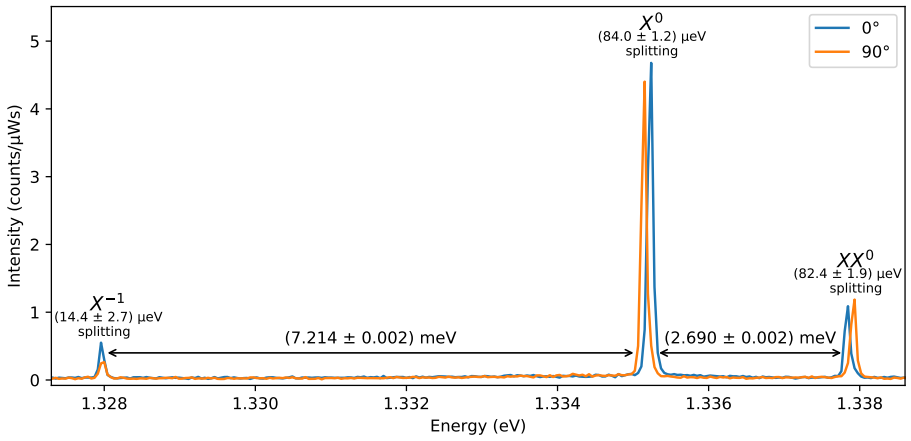

Figure 4.10: Linearly polarised detection of a dot in the $52\,\mathrm{nm}$ tunnelling barrier sample, with the lines annotated with their respective states and the splitting between the two polarisations.

emission from X^{-1} appears to have a small splitting which is unexpected. However, both the intensity of the peaks and their linewidths are significantly different between the two spectra, with the linewidths in particular changing by $18\,\mu\mathrm{eV}$ (from 88 to $70\,\mu\mathrm{eV}$). It is, therefore, more likely that this apparent splitting is due to the instability of the setup and the resolution of the spectrometer (approximately $43\,\mu\mathrm{eV}$ at this wavelength), rather than the emission having a fine structure.

With the lines being identified, we can see how they individual respond to the bias voltage to see the different charge plateaus, as shown in figure 4.11. From this figure, the instability

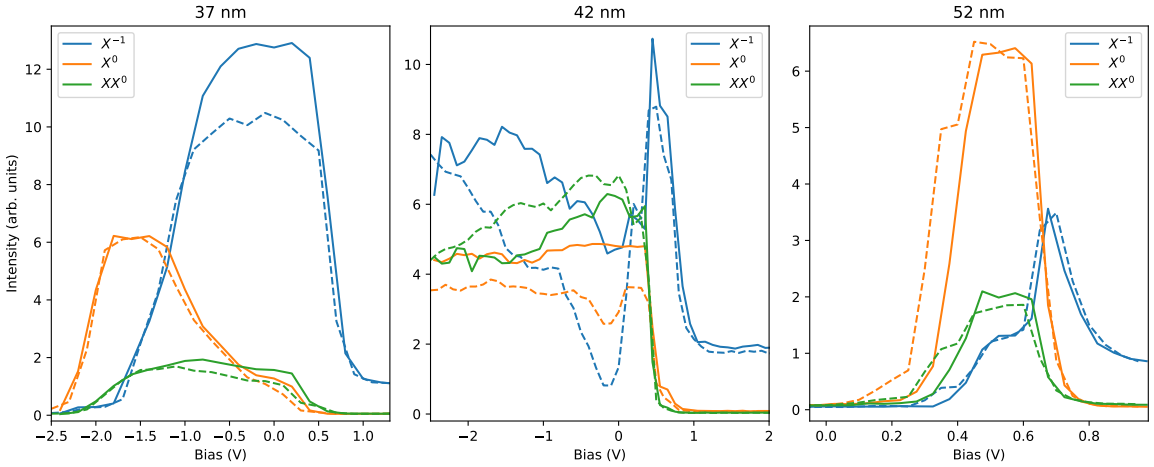

Figure 4.11: The intensities of the three identified lines for each of the dots in the three samples, whose tunnelling barrier is shown above each graph. The solid and dashed lines are for the two different measurement sweeps (see text).

of the measurement system is apparent, with the two different measurement sweeps for each charge plateau varying in intensity due to a drift in the sample's position. This can also be seen in figure 4.8, but is less obvious. The measurement sweeps the bias from the lowest voltage to the highest and then sweeps back to the lowest without repeating any voltages to highlight any hysteresis in the measurement. This is achieved by using twice the set step size for the sweeps, with the second sweep, from the highest to lowest voltage, using an offset of the step size, so that all required voltages are measured. In each of the three graphs, the X^0 and XX^0 lines generally decrease in intensity as the X^{-1} line increases in intensity, showing how the dot's states are being shifted with respect to the Fermi level. What is not particularly easy to see in figure 4.11 is the width of these plateaus in terms of bias voltage. This is, however, shown in figure 4.12 for the X^{-1} line for each of the samples. In this figure, the

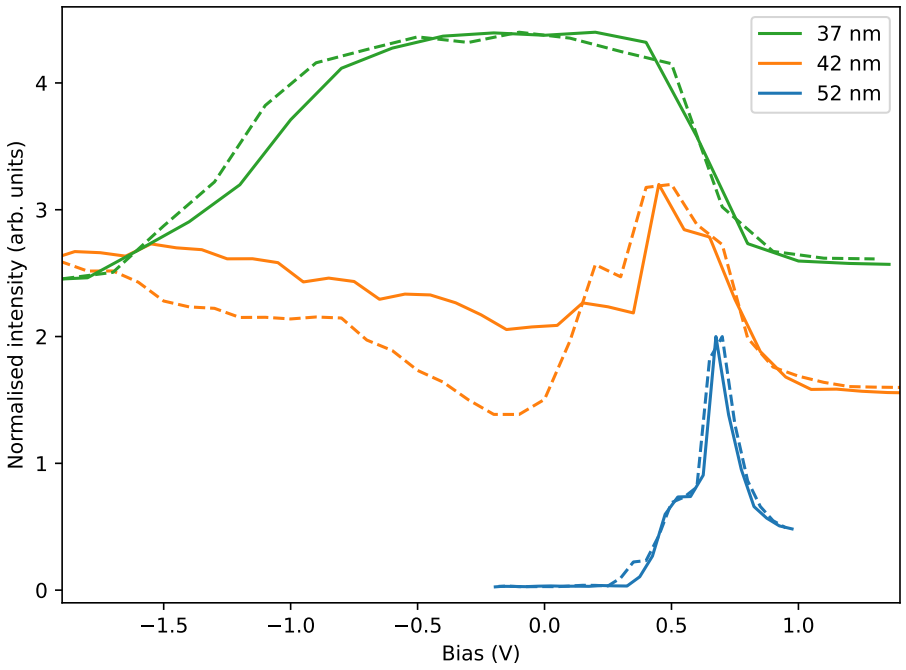

Figure 4.12: Comparison of the normalised intensities of the X^{-1} lines for each of the samples. The solid and dashed lines are for the two different measurement sweeps (see text).

width of the plateau for the $52\,\mathrm{nm}$ sample is roughly half the width of that for the $42\,\mathrm{nm}$ sample and is significantly smaller than that of the $37\,\mathrm{nm}$ sample. This is the expected behaviour, as if we think about the band structure (figure 2.7), the thicker the tunnelling barrier is, the greater the effect that the bias voltage has on shifting the dot's states relative to the Fermi level (essentially a smaller voltage is needed to produce the same relative shift

of the dot's states as dot is moved further away from the 'pivot point' in the band structure diagram).

In summary, from this initial characterisation we have determined that the grown InGaAs SAQD samples, with tunnelling barriers up to $52\,\mathrm{nm}$, correctly show the expected charging behaviour of the identified dot's states. Whilst this characterisation was rather brief, it has already aided in-depth measurements of the dependence of electron and nuclear spin lifetimes on magnet field strength [38].

Chapter 5

Measuring the gradient elastic tensor of GaAs

The gradient elastic tensor is a material specific parameter that relates the crystal's strain to the gradient of the electric field in the crystal and is important for modelling and structural analysis of quantum dots as well as for understanding the effects of the nuclear quadrupolar interaction on electron-nuclear spin dynamics. There have been few measurements of the gradient elastic tensor for GaAs, with the only notable work being that of Sundfors [54, 56]. In this chapter, we measure both independent values of the gradient elastic tensor for GaAs and find that our values are substantially different than those previously reported.

5.1 Background

A crystal has an electrostatic potential, $V(\mathbf{r})$, due to the charge distribution of the nuclei and charge carriers. The electric field, $V_i = \frac{\partial V}{\partial x_i}$, will be zero at the nuclear sites for a crystal in equilibrium; however, the electric field gradient, $V_{ij} = \frac{\partial^2 V}{\partial x_i \partial x_j}$, at the nuclear sites can be non-zero. This is not the case for a crystal with cubic symmetry, where the symmetry results in V_{ij} being zero at the nuclear sites [37]. However, when the crystal is strained, the changing in the size of the unit cell and the length of the bonds deviates the charge distribution from that of an unstrained crystal, potentially resulting in a non-zero electric field gradient at the nuclear sites. The strain induced electric field gradient, to a linear approximation[1], can be

[1] That is appropriate for 'small' strains that can be described as infinitesimal – see section 2.2.2.

described as,

$$V_{ij} = S_{ijkl}\epsilon_{kl}, \tag{5.1}$$

where S_{ijkl} is the gradient elastic tensor and ϵ_{ij} is the strain tensor. The gradient elastic tensor is a fourth rank tensor, consisting of 81 components, that is material specific. However, for the T_d cubic symmetry of GaAs, there are 21 components that are non-zero and 3 independent values,

$$S_{ijkl} = \left(\begin{array}{ccc} \begin{pmatrix} S_{11} & 0 & 0 \\ 0 & S_{12} & 0 \\ 0 & 0 & S_{12} \end{pmatrix} & \begin{pmatrix} 0 & S_{44} & 0 \\ S_{44} & 0 & 0 \\ 0 & 0 & 0 \end{pmatrix} & \begin{pmatrix} 0 & 0 & S_{44} \\ 0 & 0 & 0 \\ S_{44} & 0 & 0 \end{pmatrix} \\ \begin{pmatrix} 0 & S_{44} & 0 \\ S_{44} & 0 & 0 \\ 0 & 0 & 0 \end{pmatrix} & \begin{pmatrix} S_{12} & 0 & 0 \\ 0 & S_{11} & 0 \\ 0 & 0 & S_{12} \end{pmatrix} & \begin{pmatrix} 0 & 0 & 0 \\ 0 & 0 & S_{44} \\ 0 & S_{44} & 0 \end{pmatrix} \\ \begin{pmatrix} 0 & 0 & S_{44} \\ 0 & 0 & 0 \\ S_{44} & 0 & 0 \end{pmatrix} & \begin{pmatrix} 0 & 0 & 0 \\ 0 & 0 & S_{44} \\ 0 & S_{44} & 0 \end{pmatrix} & \begin{pmatrix} S_{12} & 0 & 0 \\ 0 & S_{12} & 0 \\ 0 & 0 & S_{11} \end{pmatrix} \end{array} \right) \tag{5.2}$$

Here we are using Voigt notation for the indices, where

$$S_{11} = S_{xxxx} = S_{yyyy} = S_{zzzz} \tag{5.3}$$

$$S_{12} = S_{xxyy} = S_{yyzz} = S_{zzxx} = S_{yyxx} = S_{zzyy} = S_{xxzz} \tag{5.4}$$

$$S_{44} = S_{yzyz} = S_{zxzx} = S_{xyxy}. \tag{5.5}$$

Further to the symmetry, when a point-charge model is used, due to only the traceless part of V_{ij} being observable in NMR, S_{12} can be represented in terms of S_{11} [45],

$$S_{12} = -\frac{S_{11}}{2}. \tag{5.6}$$

This means that we can describe the gradient elastic tensor using only two independent values, S_{11} and S_{44}, with equation 5.1 becoming,

$$V_{ij} = \begin{pmatrix} S_{11}\left(\epsilon_{xx}+\epsilon_{yy}+\epsilon_{zz}\right) & S_{44}\left(\epsilon_{xy}+\epsilon_{yx}\right) & S_{44}\left(\epsilon_{xz}+\epsilon_{zx}\right) \\ S_{44}\left(\epsilon_{xy}+\epsilon_{yx}\right) & S_{11}\left(\epsilon_{xx}+\epsilon_{yy}+\epsilon_{zz}\right) & S_{44}\left(\epsilon_{yz}+\epsilon_{zy}\right) \\ S_{44}\left(\epsilon_{xz}+\epsilon_{zx}\right) & S_{44}\left(\epsilon_{yz}+\epsilon_{zy}\right) & S_{11}\left(\epsilon_{xx}+\epsilon_{yy}+\epsilon_{zz}\right) \end{pmatrix}. \quad (5.7)$$

It should be noted that S_{11} is only part of the diagonal elements, whereas S_{44} is only part of the off-diagonal elements of V_{ij}.

The electric quadrupole moment of the nucleus interacts with the electric field gradient and the Hamiltonian for the interaction is,

$$\hat{H}_Q = \frac{eQ}{6I\left(2I-1\right)h}\sum_{i,j} V_{ij}\left[\frac{3}{2}\left(\hat{I}_i\hat{I}_j+\hat{I}_j\hat{I}_i\right)-\delta_{ij}I^2\right], \quad (5.8)$$

where Q is the quadrupole moment of the nucleus, I is the nuclear spin, $\hat{I}_n$ is the nth component of the spin operator, e is the elementary charge, h is Planck's constant and the subscripts i and j are either x, y or z [37]. As a magnetic field is used, the total Hamiltonian has the addition of the Zeeman effect,

$$\hat{H}_z = -\frac{\gamma}{2\pi}\mathbf{B}\cdot\hat{\mathbf{I}}, \quad (5.9)$$

where γ is the gyromagnetic ratio and $\mathbf{B}$ is the magnetic field vector. The total Hamiltonian for the system is the sum of equations 5.8 and 5.9.

In the following sections, the measurement of both S_{11} and S_{44} will be discussed. But prior to this, it is useful to understand what the expected NMR spectrum, using first order perturbation theory, looks like for a system of $\frac{3}{2}$ nuclear spins. Figure 5.1 shows a schematic version of this, where the transitions between the nuclear states appear as peaks with a finite width. The $-\frac{1}{2} \Leftrightarrow \frac{1}{2}$ transition is known as the central transition and is at the resonant frequency of the nuclei. The $\frac{1}{2} \Leftrightarrow \frac{3}{2}$ and $-\frac{3}{2} \Leftrightarrow -\frac{1}{2}$ transitions, referred to as satellite transitions, are separated from the central transition by the quadrupolar frequency ν_Q. The quadrupolar frequency, as we will see later, depends on the direction of the magnetic field, the quadrupole moment of the nuclei, the gradient elastic tensor and the strain present. If there is no strain in the material, then the satellite transitions will overlap the central transition

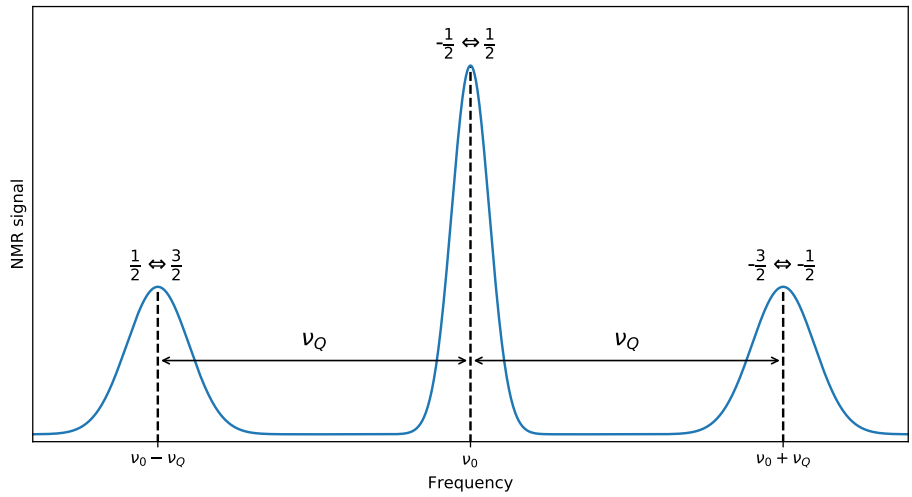

Figure 5.1: Schematic of an NMR spectrum, where ν_0 is the resonant frequency of the nuclei and ν_Q is the quadrupolar frequency.

(as ν_Q is zero). In addition to this, the quadrupolar frequency can be negative (due to the values of the gradient elastic and strain tensors), which results in the satellite transitions being swapped relative to their frequency (so the $\frac{1}{2} \Leftrightarrow \frac{3}{2}$ transition is at $\nu_0 + \nu_Q$).

As the gradient elastic tensor relates the strain tensor to the electric field gradient, it is an important material property for understanding NMR, modelling quantum dot structures and understanding electron-nuclear spin dynamics. Previously, the value of the gradient elastic tensor was measured using an indirect method which, as we will show later, had issues with its accuracy.

To measure the gradient elastic tensor for GaAs, different methodologies were used for measuring each component, which are described in the following sections.

5.2 Measurement of the S_{11} component

To determine the value of S_{11} from NMR requires precisely knowing the value of the strain tensor. Whilst this can be calculated from measuring the applied stress, the resulting strain is insensitive to local variations. An alternative is to measure the PL of the GaAs, where the strain results in splitting of the light and heavy-hole states (see section 2.2.2). The resulting value of the strain is averaged over the area that is illuminated, allowing a significantly finer resolution in regard to localised variations. When combined with quantum dot NMR,

we have the ability to measure the effect of the quadrupolar moment of approximately 10^6 nuclei spherically surrounding the quantum dot's exciton and to measure the strain over approximately 10^{10} nuclei in a cylinder centred on the quantum dot with a width of the excitation laser spot and a material dependent depth, resulting in a highly localised probe.

As the quadrupolar frequency, ν_Q, is less than $500\,\mathrm{kHz}$, it is approximately two orders of magnitude smaller than the resonant frequency of the nuclei, ν_0 ($50\,\mathrm{MHz}$ to $110\,\mathrm{MHz}$ for the $8\,\mathrm{T}$ static magnetic field used). We can therefore treat $\hat{H}_Q$ as a perturbation.

For these measurements, the static magnetic field is aligned within 2° of the sample's growth direction (z axis)[2], this reduces equation 5.9 to,

$$\hat{H}_z = -\frac{\gamma}{2\pi} B_z \hat{I}_z, \tag{5.10}$$

which, in the basis of the nuclear spin states, is a diagonal matrix, resulting in no state mixing in the eigenvectors. The resulting eigenvalues are,

$$E_{z,\frac{3}{2}} = -\frac{3\gamma B_z}{4\pi} \tag{5.11}$$

$$E_{z,\frac{1}{2}} = -\frac{\gamma B_z}{4\pi} \tag{5.12}$$

$$E_{z,-\frac{1}{2}} = \frac{\gamma B_z}{4\pi} \tag{5.13}$$

$$E_{z,-\frac{3}{2}} = \frac{3\gamma B_z}{4\pi}. \tag{5.14}$$

As only magnetic dipole transitions are possible in NMR, the allowed transitions are where I_z changes by ± 1, with the frequencies of these transitions being,

$$\nu_{z,\frac{1}{2}\Leftrightarrow\frac{3}{2}} = \frac{\gamma B_z}{2\pi} \tag{5.15}$$

$$\nu_{z,-\frac{1}{2}\Leftrightarrow\frac{1}{2}} = \frac{\gamma B_z}{2\pi} \tag{5.16}$$

$$\nu_{z,-\frac{3}{2}\Leftrightarrow-\frac{1}{2}} = \frac{\gamma B_z}{2\pi}. \tag{5.17}$$

[2]This was achieved by aligning the sample to the insert and the insert being designed so that it has to be closely aligned to the magnetic field to be inserted into the cryostat - due to the bore on the magnet and the fastening at the top of the cryostat.

As previously mentioned, without the quadrupolar effects, the three transitions that are visible in the NMR spectra will not be split and will instead overlap each other.

When $\hat{H}_Q$ is used as a perturbation, the off-diagonal terms of V_{ij} (equation 5.7) are not present in the first order corrections,

$$E_{Q,\frac{3}{2}} = \frac{eQ}{4h} S_{11}\epsilon_b \tag{5.18}$$

$$E_{Q,\frac{1}{2}} = -\frac{eQ}{4h} S_{11}\epsilon_b \tag{5.19}$$

$$E_{Q,-\frac{1}{2}} = -\frac{eQ}{4h} S_{11}\epsilon_b \tag{5.20}$$

$$E_{Q,-\frac{3}{2}} = \frac{eQ}{4h} S_{11}\epsilon_b, \tag{5.21}$$

where the biaxial strain $\epsilon_b = \epsilon_{zz} - \frac{1}{2}(\epsilon_{xx} + \epsilon_{yy})$ has been used. As a result of this, the first order approach, when the magnetic field is aligned with the sample's growth direction, is insensitive to shear strain.

The transitions between these frequency corrections are,

$$\nu_{Q,\frac{1}{2}\Leftrightarrow\frac{3}{2}} = -\frac{eQ}{2h} S_{11}\epsilon_b \tag{5.22}$$

$$\nu_{Q,-\frac{1}{2}\Leftrightarrow\frac{1}{2}} = 0 \tag{5.23}$$

$$\nu_{Q,-\frac{3}{2}\Leftrightarrow-\frac{1}{2}} = \frac{eQ}{2h} S_{11}\epsilon_b. \tag{5.24}$$

When the first order frequency corrections are applied to the eigenvalues, the transition frequencies are,

$$\nu_{\frac{1}{2}\Leftrightarrow\frac{3}{2}} = \frac{\gamma B_z}{2\pi} - \frac{eQ}{2h} S_{11}\epsilon_b \tag{5.25}$$

$$\nu_{-\frac{1}{2}\Leftrightarrow\frac{1}{2}} = \frac{\gamma B_z}{2\pi} \tag{5.26}$$

$$\nu_{-\frac{3}{2}\Leftrightarrow-\frac{1}{2}} = \frac{\gamma B_z}{2\pi} + \frac{eQ}{2h} S_{11}\epsilon_b. \tag{5.27}$$

From this, it is fairly trivial to see that when the magnetic field is in the z direction,

$$\nu_Q = \frac{eQ}{2h} S_{11}\epsilon_b. \tag{5.28}$$

5.2.1 Experimental technique

For determining the value of S_{11} for GaAs, rectangular pieces of sample A (see table 3.1) measuring approximately $900\,\mu\text{m} \times 1500\,\mu\text{m} \times 350\,\mu\text{m}$ along $[1\,1\,0]$, $[1\,\bar{1}\,0]$ and $[0\,0\,1]$, respectively (with $[0\,0\,1]$ being the growth direction), were externally stressed using two different styles of clamps, as described in section 3.3, with the applied stress being varied. In addition to these, an unstrained sample was also used. Experiments were conducted in the bath cryostat setup described in section 3.2 at approximately $4.2\,\text{K}$. Each quantum dot was found by searching the sample for well isolated PL emission, then the NMR and GaAs PL spectra were measured.

The different directions of the stress being applied to the sample will result in the strain tensor being substantially different for the two different styles of clamp, affecting the observed PL. From section 2.2.2, strain splits the light- and heavy-hole states, with their energy in PL being,

$$E_{\text{PL}} = E_g + a\epsilon_h \pm \sqrt{b^2\left(\epsilon_b^2 + \frac{3}{4}\epsilon_\eta^2\right) + d^2\epsilon_s^2}, \tag{5.29}$$

where E_g is the energy of the band gap, b and d are the deformation potentials, the hydrostatic strain is $\epsilon_h = \epsilon_{xx} + \epsilon_{yy} + \epsilon_{zz}$, the asymmetry in the biaxial strain is $\epsilon_\eta = \epsilon_{xx} - \epsilon_{yy}$ and the shear strain is $\epsilon_s^2 = \epsilon_{xy}^2 + \epsilon_{xz}^2 + \epsilon_{yz}^2$.

For the clamp applying stress in the $[0\,0\,1]$ direction, the force is, ideally, applied uniformly over the $(0\,0\,1)$ surfaces of the sample. The symmetry of the stress, results in the off diagonal components of the stress tensor (ϵ_{xy}, ϵ_{xz} and ϵ_{yz}) being zero as well as the asymmetry of the biaxial strain being zero (as $\epsilon_{xx} = \epsilon_{yy}$). This reduces equation 5.29 to

$$E_{\text{PL},[001]} = E_g + a\epsilon_h \pm b\epsilon_b. \tag{5.30}$$

Unfortunately, the force will not be evenly distributed across the sample's surface. Finite element modelling of the sample and clamp, shows that the asymmetry in the biaxial strain is of little concern as it is around $0.0001\,\%$ of the biaxial strain (when excluding the edges of the sample) – see figure 5.2. However, the shear component of the strain is not zero as shown in figure 5.3 in relation to the biaxial strain. As the b and d deformation potentials for GaAs are of the same order, at the middle of the sample the contribution of the shear

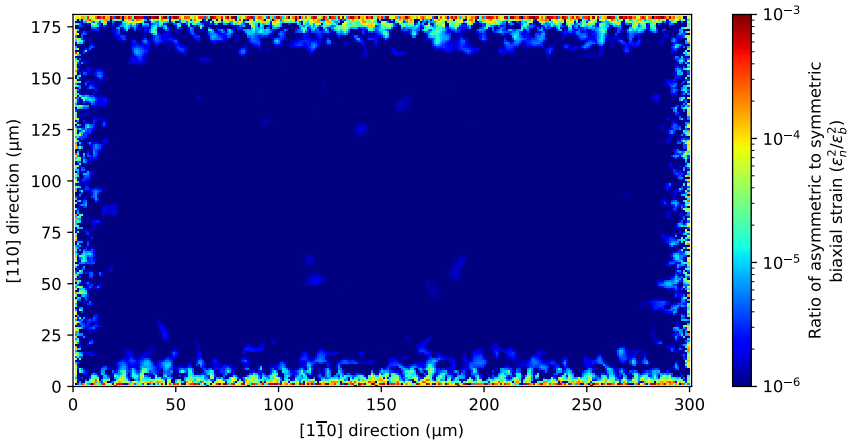

Figure 5.2: Ratio of asymmetric to symmetric biaxial strain for the $(0\,0\,1)$ surface of the sample when compressive stress is applied along the $[0\,0\,1]$ direction. Data is from a finite element model.

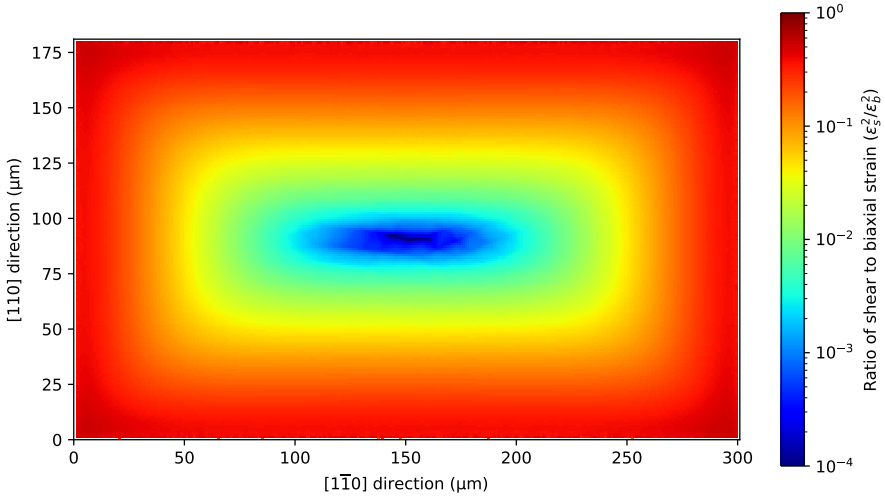

Figure 5.3: Ratio of shear to biaxial strain for the $(0\,0\,1)$ surface of the sample when compressively stressed along the $[0\,0\,1]$ direction. Data is from a finite element model.

strain to the energy of the PL is dwarfed by the biaxial component and is likely to have little effect when measurement errors are considered. The same will be true for the immediate area surrounding the middle of the sample. As the presence of the shear strain becomes significant, the linear relationship of ν_Q to the splitting of E_{PL} will deviate, and so can be used as a test to ensure that ϵ_s is small enough to not affect the results.

The clamp applying stress in the $[1\,1\,0]$ direction is more complicated. As ϵ_{xx} is aligned with the $[1\,0\,0]$ direction and ϵ_{yy} with $[0\,1\,0]$, stress in the $[1\,1\,0]$ direction will result in ϵ_{xy}, and therefore ϵ_s, being non-zero. Ideally, ϵ_{xy} would be constant and so would not affect the relationship between the quadrupolar frequency and the energy of the PL. However, this is not the case for a real sample, as shown in figure 5.4, and will affect the linear relationship between ν_Q and the splitting of E_{PL}. As no external stress is applied to the $(0\,0\,1)$ surface

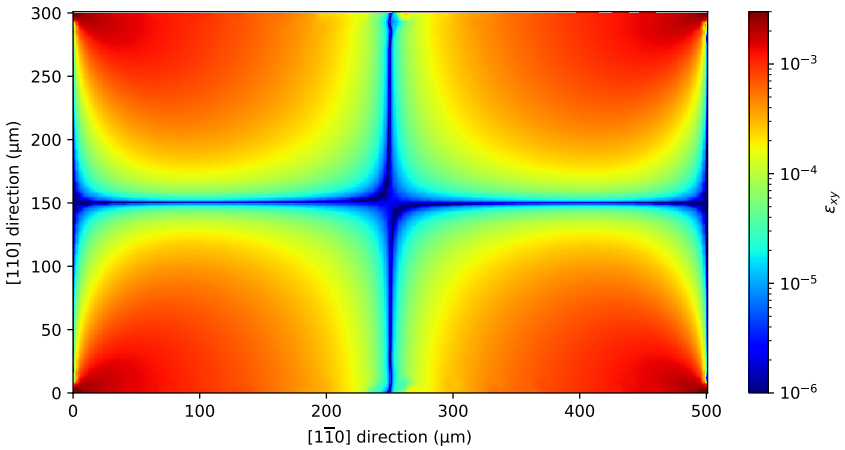

Figure 5.4: Strain in the $[1\,1\,0]$ direction for the $(0\,0\,1)$ surface of the sample when compressively stressed along the $[1\,1\,0]$ direction. Data is from a finite element model.

(i.e. it is traction free), only the σ_{xx}, σ_{yy} and σ_{xy} components of the stress tensor are non-zero (where the stress tensor $\sigma_{ij} = \sum_{kl} c_{ijkl}\epsilon_{kl}$, with c_{ijkl} being the elastic stiffness constants [46]). This allows the biaxial strain to be expressed in terms of the hydrostatic strain,

$$\epsilon_b = -\frac{\sigma_{xx} + \sigma_{yy}}{2\,(c_{11} - c_{12})} \tag{5.31}$$

$$\epsilon_h = \frac{\sigma_{xx} + \sigma_{yy}}{c_{11} + 2c_{12}} \tag{5.32}$$

$$\frac{\epsilon_b}{\epsilon_h} = -\frac{c_{11} + 2c_{12}}{2\,(c_{11} - c_{12})} \tag{5.33}$$

where we are now using Voigt notation for the elastic stiffness constants. The uniformity

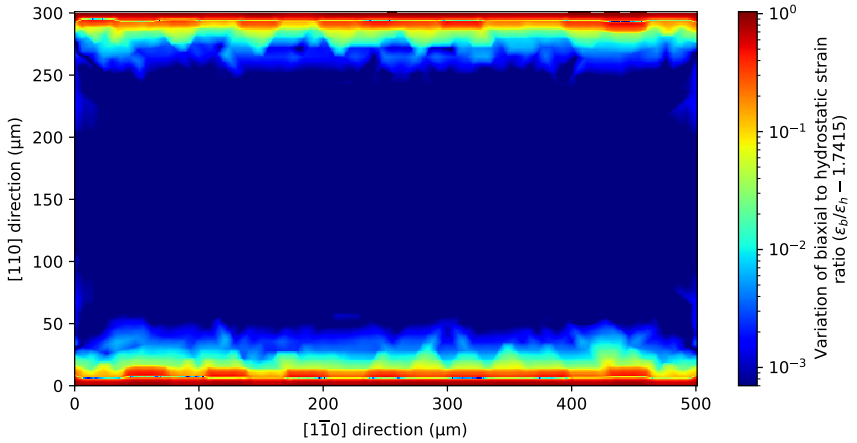

Figure 5.5: Ratio of biaxial to hydrostatic strain for the $(0\,0\,1)$ surface of the sample when compressively stressed along the $[1\,1\,0]$ direction. Data is from a finite element model.

of the ratio of the biaxial and hydrostatic strains, from finite element modelling, is shown in figure 5.5. Whilst there are regions near the edges that are externally stressed (the top and bottom of figure 5.5) where the ratio is not constant, the vast majority of the sample has a variation in the uniformity that is smaller than the experimental error. Using this ratio, equation 5.29 can be expressed as,

$$E_{\mathrm{PL},[110]} = E_g + \frac{2\left(c_{12}-c_{11}\right)}{c_{11}+2c_{12}}a\epsilon_b \pm \sqrt{b^2\left(\epsilon_b^2+\frac{3}{4}\epsilon_\eta^2\right)+d^2\epsilon_s^2}. \tag{5.34}$$

Whilst ϵ_s is still present for each split component of the PL, by taking the average of both components this can be removed,

$$\overline{E}_{\mathrm{PL},[110]} = E_g + \frac{2\left(c_{12}-c_{11}\right)}{c_{11}+2c_{12}}a\epsilon_b, \tag{5.35}$$

with the result having a linear relationship with ν_Q (equation 5.28).

5.2.2 Results

The NMR spectra were measured in a static $8\,\mathrm{T}$ magnetic field, with representative examples of the three types of samples shown in figure 5.6. For the $[0\,0\,1]$ stressed sample, the $-\frac{3}{2} \Leftrightarrow \frac{1}{2}$ satellite transition, due to the stress, is found at lower frequencies than the $-\frac{1}{2} \Leftrightarrow \frac{1}{2}$ central transition. This is opposite to the unstressed material and so is denoted by the quadrupolar

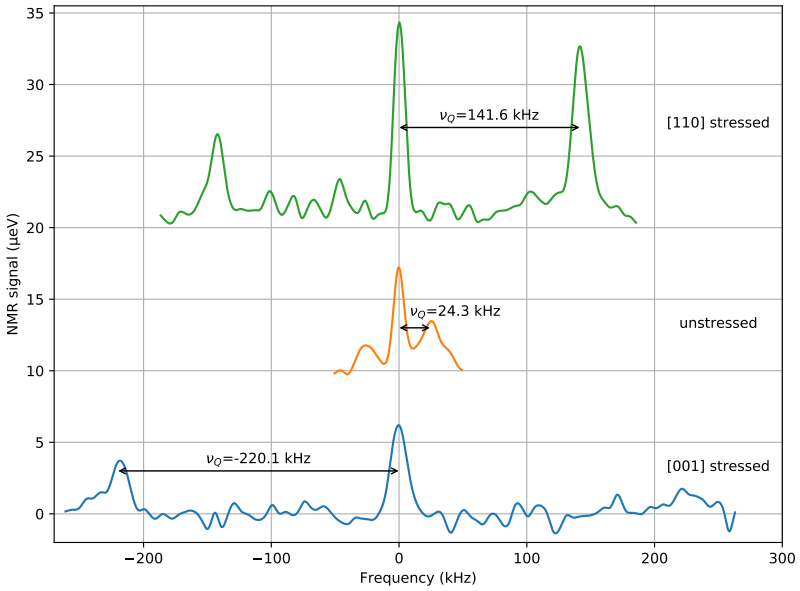

Figure 5.6: Representative NMR spectra, of ^{75}As, for the three strain configurations. The quadrupolar frequency, ν_Q, is labelled between the $-\frac{3}{2} \Leftrightarrow \frac{1}{2}$ and $-\frac{1}{2} \Leftrightarrow \frac{1}{2}$ transitions.

frequency being negative. As we are using 'strain-free' quantum dots, it is reasonable to expect that the quadrupolar frequency of the unstrained sample should be zero. However, the term 'strain-free' is in comparison to SAQDs, where the intrinsic strain is significantly larger.

The GaAs PL was measured without an applied magnetic field, with representative examples of the three types of samples shown in figure 5.7. The spectra in figure 5.7 are for the same quantum dots as those in figure 5.6. The laser excitation for the GaAs PL had an approximate energy of $1.54\,\mathrm{eV}$ and an intensity of approximately $5 \times 10^6\,\mathrm{W\,m^{-2}}$.

As discussed in section 2.2.2, the light- and heavy-hole states in unstrained GaAs are degenerate and so there should be no splitting of the emission from the light- and heavy-hole states; there should also be no splitting in the NMR spectra. Both figures 5.6 and 5.7 show a small quadrupolar frequency and a small splitting of the excitons, respectively. In the case of the NMR spectra, this is likely to be caused by the lattice mismatch between the AlGaAs barrier the dots are etched into and the GaAs buffer layer / substrate. However, as the observed PL is predominantly from the top capping layer, the origin of the exciton splitting is more likely to be defects in the GaAs of the capping layer.

For both the $[0\,0\,1]$ and $[1\,1\,0]$ stressed samples, the fourfold degeneracy of the light- and heavy-hole states is split into two twofold degeneracies, with the resulting excitons being

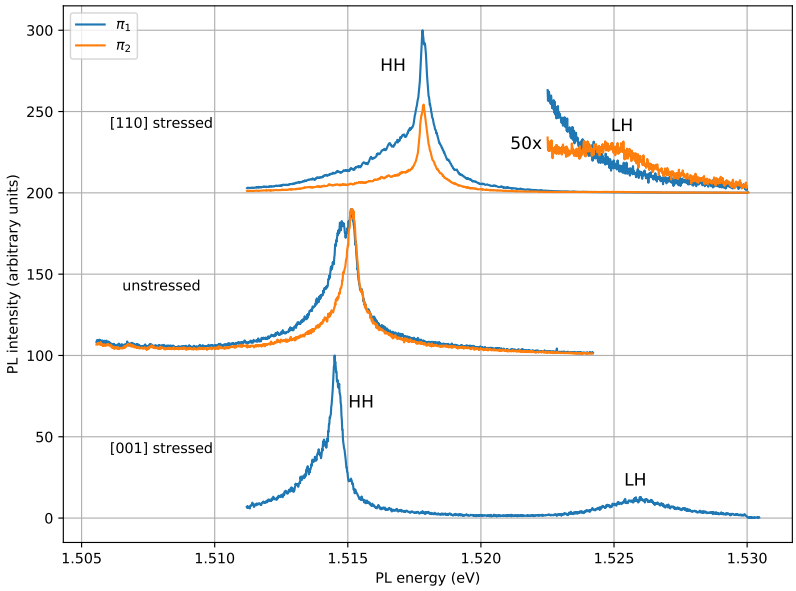

Figure 5.7: Representative PL spectra, of GaAs, for the three strain configurations. The PL from the predominantly light- and heavy-hole states is annotated with 'LH' and 'HH', respectively. For the unstressed and $[1\,1\,0]$ stressed spectra, two orthogonal polarisations of the PL are shown. This is not shown for the $[0\,0\,1]$ stressed spectra as it is not dependent on polarisation.

visible in the PL as two separate peaks. For the $[0\,0\,1]$ stress, these peaks are unpolarised; however, for the $[1\,1\,0]$ stress they are, at least partially, linearly polarised. This is due to the light- and heavy-holes states having their momentum quantisation axis along the $[1\,1\,0]$ direction and the observed peaks in the PL not being pure states.

Figure 5.8 shows the energy of the light- and heavy-hole lines seen in PL with respect to the quadrupolar frequency, for $^{75}\mathrm{As}$, seen in NMR, for a multitude of quantum dots in the three stress configurations. The unstressed sample only shows a small variation for both the light- and heavy-hole energies and the quadrupolar frequency, with the range of these variations being smaller than the shifts observed when the sample is externally stressed. The stressed samples have a significantly larger variation as the applied stress is not perfectly uniform; however, the length scales of these variations are much larger than the area that is measured in both PL and NMR.

Figures 5.9 and 5.10 plot the data shown in figure 5.8 to extract the linear relationship of the data. In particular, the fitted line in figure 5.9 of the splitting of the light- and heavy-holes for the $[0\,0\,1]$ stressed and unstressed samples has a gradient of $(47.0 \pm 1.5)\,\mu\mathrm{eV\,kHz^{-1}}$; with

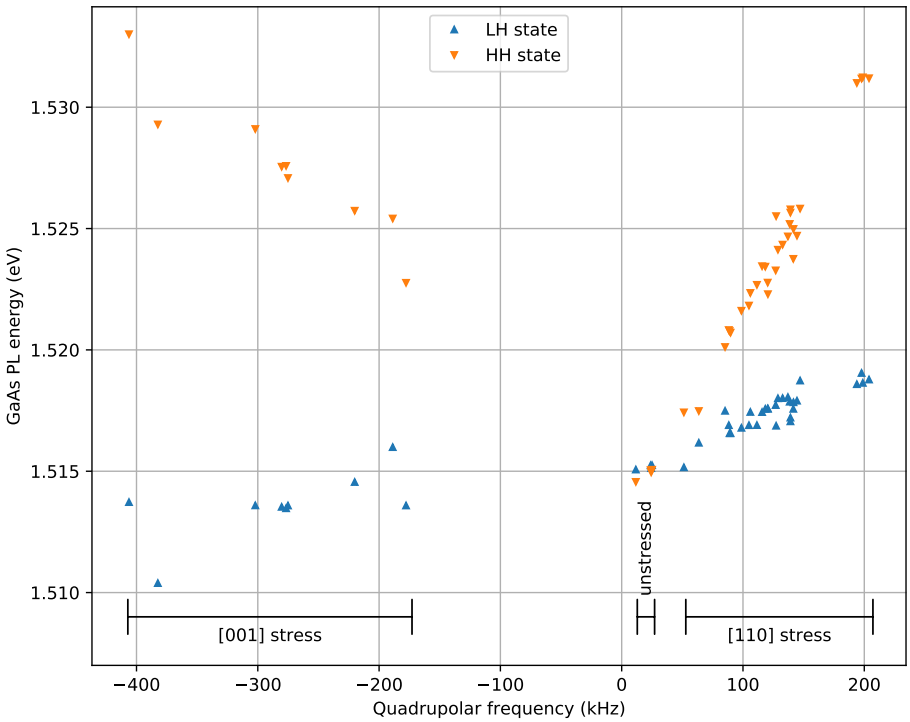

Figure 5.8: Energy of the GaAs PL peaks verses the ^{75}As quadrupolar frequency for quantum dots in the three stress configurations (annotated below data).

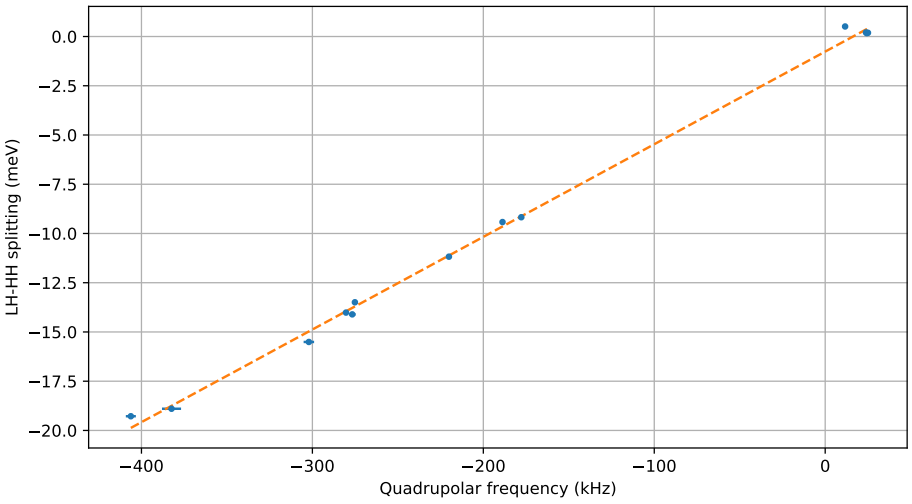

Figure 5.9: The splitting of the light- and heavy-hole peaks in PL verses the quadrupolar frequency for the $[0\,0\,1]$ stressed and unstressed samples.

the fitted line in figure 5.10 of the average light- and heavy-hole energy for the $[1\,1\,0]$ stressed sample has a gradient of $(55.7 \pm 2.2)\,\mu\mathrm{eV\,kHz^{-1}}$.

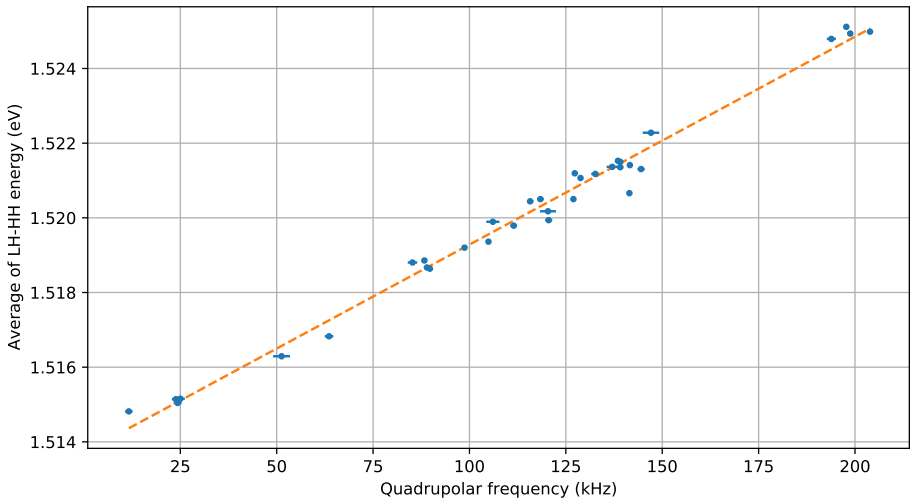

Figure 5.10: The average energy of the light- and heavy-hole peaks in PL verses the quadrupolar frequency for the $[1\,1\,0]$ stressed sample.

Utilising equations 5.28 and 5.30, the gradient for the fitted line in figure 5.9 can be determined as,

$$k_{[001]} = -\frac{4bh}{eQS_{11}}, \tag{5.36}$$

where the minus has been added to reflect that the light-hole exciton has a lower energy when the biaxial strain is less than zero, and using equation 5.35, the gradient for the fitted line in figure 5.10 can be shown to be,

$$k_{[110]} = \frac{c_{12} - c_{11}}{c_{11} + 2c_{12}} \frac{4ah}{eQS_{11}}. \tag{5.37}$$

As both of the gradients for the fitted lines, $k_{[001]}$ and $k_{[110]}$, can be used to determine the value of QS_{11} for $^{75}\mathrm{As}$, we choose to use $k_{[110]}$ as it has the most data points and will give a more reliable value. This results in a value for $(QS_{11})_{^{75}\mathrm{As}}$ of $(0.750 \pm 0.031)\,\mu\mathrm{V}$, when using $c_{11} = 118.8\,\mathrm{GPa}$, $c_{12} = 53.8\,\mathrm{GPa}$ and $a = -8.8\,\mathrm{eV}$ [47]. Using a value of $(0.314 \pm 0.006) \times 10^{-28}\,\mathrm{m^2}$ for $Q_{^{75}\mathrm{As}}$ [48], we find a value for $S_{11,^{75}\mathrm{As}}$ of $(23.9 \pm 1.1) \times 10^{21}\,\mathrm{V\,m^{-2}}$.

To calculate the values for $^{69}\mathrm{Ga}$, we first create a ratio of the quadrupolar frequencies for $^{69}\mathrm{Ga}$ and $^{75}\mathrm{As}$, for the same quantum dots, based on a smaller number of measurements than

in figure 5.10. From equation 5.28, this ratio is,

$$\frac{\nu_{Q,^{69}\mathrm{Ga}}}{\nu_{Q,^{75}\mathrm{As}}} = \frac{(QS_{11})_{^{69}\mathrm{Ga}}}{(QS_{11})_{^{75}\mathrm{As}}}, \tag{5.38}$$

assuming that ϵ_b is the same for both type of nuclei. The justification for this assumption is, firstly, the NMR technique used produces a spectrum that consists of nuclei that are from a single quantum dot and so different isotopes will be subject to the same strain. Secondly, the equivalence of strain for anions and cations is required for the integrity of the crystal structure and results in the displacement of the sublattices being within a small fraction of the lattice constant of each other. As the displacement is a smooth function, the strain tensor will have highly similar values for the sublattices. Thirdly, and finally, if the strain is not the same for the different isotopes, the ratio of the quadrupolar frequencies will not be linear. Figure 5.11 shows the relationship of the quadrupolar frequencies for $^{69}\mathrm{Ga}$ and $^{75}\mathrm{As}$ and it

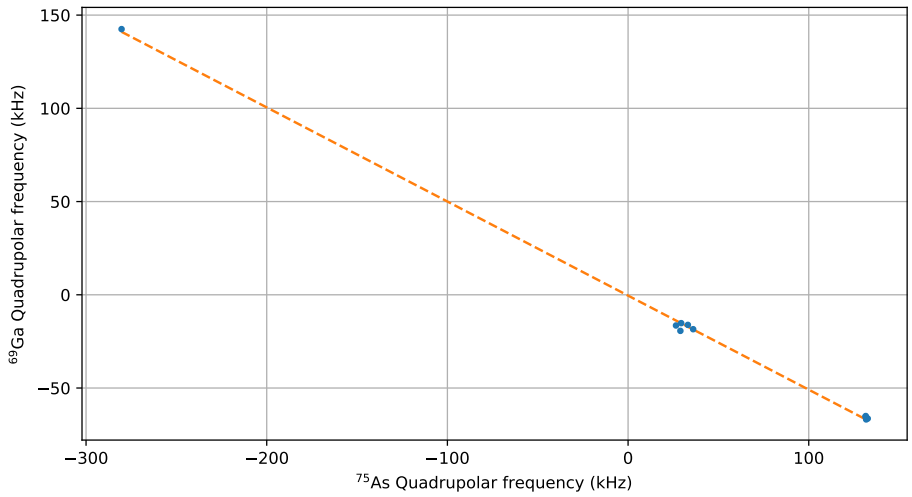

Figure 5.11: Comparison of the $^{69}\mathrm{Ga}$ and $^{75}\mathrm{As}$ quadrupolar frequencies for quantum dots in all three stress configurations.

is well described by a linear model, with the fitted line in the figure having a gradient of -0.505 ± 0.013, which is the ratio $\frac{\nu_{Q,^{69}\mathrm{Ga}}}{\nu_{Q,^{75}\mathrm{As}}}$. Using this ratio, the values for $^{69}\mathrm{Ga}$ can be calculated as $(QS_{11})_{^{69}\mathrm{Ga}} = (-0.379 \pm 0.018)\,\mu\mathrm{V}$ and $S_{11,^{69}\mathrm{Ga}} = (-22.2 \pm 1.1) \times 10^{21}\,\mathrm{V\,m^{-2}}$.

In addition to the values above, it is possible to use the $[0\,0\,1]$ and $[1\,1\,0]$ stress data to calculate the ratio of the deformation constants, $\frac{b}{a}$. Whilst this is not a sought after value, it does provide an ability to check the validity of the experimental technique, as the values for

the deformation constants are reasonably well known. Using equations 5.36 and 5.37 this ratio is,

$$\frac{b}{a} = \frac{c_{11} - c_{12}}{c_{11} + 2c_{12}} \frac{k_{[001]}}{k_{[110]}}. \tag{5.39}$$

The value of this ratio, using the same values for c_{11} and c_{12} as before [47], is 0.242 ± 0.018.

A summary of the results is shown in table 5.1.

Parameter	Value	Unit
$(QS_{11})_{^{69}\mathrm{Ga}}$	-0.379 ± 0.018	$\mu\mathrm{V}$
$(QS_{11})_{^{75}\mathrm{As}}$	0.750 ± 0.031	$\mu\mathrm{V}$
$S_{11,^{69}\mathrm{Ga}}$	-22.2 ± 1.1	$10^{21}\,\mathrm{V\,m^{-2}}$
$S_{11,^{75}\mathrm{As}}$	23.9 ± 1.1	$10^{21}\,\mathrm{V\,m^{-2}}$
$\frac{\nu_{Q,^{69}\mathrm{Ga}}}{\nu_{Q,^{75}\mathrm{As}}}$	-0.505 ± 0.013	
$\frac{b}{a}$	0.242 ± 0.018	

Table 5.1: Summary of the S_{11} experimental results

5.2.3 Discussion

To check the validity of the experimental technique, we shall first look at the calculated value of $\frac{b}{a}$. Values of the deformation constants for GaAs do vary slightly, with a ranging from $-8.33\,\mathrm{eV}$ to $-8.8\,\mathrm{eV}$ and b ranging from $-1.76\,\mathrm{eV}$ to $-2.1\,\mathrm{eV}$ [47, 49–53]. However, the range of values for $\frac{b}{a}$ are quite small at 0.20 to 0.24. The value that we calculate, 0.242 ± 0.018, is at the upper side of this range, but is still in agreement with the range of ratios derived from the published values[3] and so we can consider that the technique is at least largely valid.

There has only been a single published work on determining S_{11} for $^{69}\mathrm{Ga}$ and $^{75}\mathrm{As}$ [54], whose values are shown in table 5.2. Even from a cursory glance, there are substantial differences between the values in [54] and ours – in fact, our values for both isotopes are approximately $30\,\%$ smaller. While the uncertainty in the deformation potential constants does contribute to the difference, their contribution is much smaller than the difference. Due

[3]It should be noted here that the ratios are derived from each published work. We have not combined deformation constants from different pieces of work to derive the ratios, as this is likely to introduce extra sources of error and unfairly widen the range.

Parameter	Value	Unit
$(QS_{11})_{^{69}\mathrm{Ga}}$	$\mp 0.54 \pm 0.03$	μV
$(QS_{11})_{^{75}\mathrm{As}}$	$\pm 1.06 \pm 0.04$	μV
$S_{11,^{69}\mathrm{Ga}}$	$\mp 31.7 \pm 1.9$	$10^{21}\,\mathrm{V\,m^{-2}}$
$S_{11,^{75}\mathrm{As}}$	$\pm 34.0 \pm 5.2$	$10^{21}\,\mathrm{V\,m^{-2}}$

Table 5.2: S_{11} values from [54]. The values have been converted from cgs to SI.

to the sample structure, it is possible for the nuclei in the AlGaAs barrier to be contributing to the NMR spectrum. However, the small strain caused by the lattice mismatch between the GaAs quantum dot and the AlGaAs barrier is seen in the unstressed data (see figure 5.8), and so the nuclei in the AlGaAs barrier will have a different quadrupolar frequency to that of the nuclei in the GaAs dot. This contribution to the spectrum will also be quite small, as only approximately $10\,\%$ of the electron's wavefunction extends into the barrier [34], resulting in a small asymmetry in the shape of the satellite transitions. The effect of this on the line fitting and subsequent quadrupolar frequency for the quantum dot will be quite marginal. The presence of an electron in the dot will lead to both the broadening of the transitions and shifts of tens of kilohertz to the NMR spectrum [55]. However, these effects are suppressed in our measurements as the quantum dot is not illuminated when the RF is applied. Further to this, the central transition of the quantum dots is resolution limited for $^{75}\mathrm{As}$. When the central transitions are broader ($<10\,\mathrm{kHz}$), indicating the possible intermittent occupation of the dot, there is no deviation of the quadrupolar frequency – suggesting that the limited occupation is not long enough to have a significant effect on the measured spectrum.

Furthermore, if we consider the ratio of the results, that is $\frac{(QS_{11})_{^{69}\mathrm{Ga}}}{(QS_{11})_{^{75}\mathrm{As}}}$, we find that our value, -0.505 ± 0.032, is in very close agreement with the previous result, -0.508 ± 0.034 [54], suggesting that a systematic error is the cause of the difference. The previous work used a measurement technique, nuclear acoustic resonance, that requires the calibration of a large number of parameters, which gives a lot of opportunities for a systematic error to creep in. In addition to this, the difference in the results might be due to how the nuclear spins react to static strain, used in this work, and dynamic strain, used in the previous work – something that has not been significantly investigated for GaAs. Both of these are issues that our measurements do not have. It is also worth noting that the authors used the same technique for determining the S_{11} value for $^{115}\mathrm{In}$ in InSb and found their value to be signifi-

cantly larger than those previously measured, which also used static strain [56]. Therefore, it is most likely that the previous work had a systematic error that resulted in their values being unintentionally increased beyond the true values.

Unlike the previous work, our technique is able to determine the sign of the gradient elastic tensor. For GaAs/AlGaAs quantum dots the electron g factor is small, with the observed Zeeman shifting of the exciton's lines largely due to the hole g factor [57]. For a positive static magnetic field ($B_z > 0$), the hole g factor results in the exciton with a hole momentum projection of $j_z = +\frac{3}{2}$ ($\Uparrow$) having higher energy. For the exciton to be optically active, it must have an electron momentum projection of $s_z = -\frac{1}{2}$ ($\downarrow$). Under σ^+ excitation, the high energy Zeeman component is enhanced and the Overhauser splitting increases. As σ^+ excitation predominately creates $\Downarrow\uparrow$ excitons, the increase in the Overhauser splitting is due to the spin pumping of nuclear spins with $I_z < 0$, as the electrons' spin is $-\frac{1}{2}$ and the hyperfine constant is positive for both As and Ga nuclei. In the σ^+ NMR spectrum, the $-\frac{3}{2} \Leftrightarrow -\frac{1}{2}$ transition will be enhanced and have a larger amplitude than that of the $\frac{1}{2} \Leftrightarrow \frac{3}{2}$ transition, allowing them to be identified. When the $-\frac{3}{2} \Leftrightarrow -\frac{1}{2}$ transition has a lower frequency than the central transition, this indicates that $\nu_q < 0$. This is the case for the $[0\,0\,1]$ stressed spectrum shown in figure 5.6. As the stress is compressive ($\epsilon_b < 0$) and the quadrupole moment for $^{75}\mathrm{As}$ is positive, this results in $S_{11,^{75}\mathrm{As}} > 0$. For $^{69}\mathrm{Ga}$, where the quadrupole moment is negative, the sign is reversed, resulting in $S_{11,^{69}\mathrm{Ga}} < 0$.

5.3 Measurement of the S_{44} component

The S_{44} component of the gradient elastic tensor describes the effect of shear strain on the electric field gradient. As shown in figure 5.4, a shear stress can be introduced by using a uniaxial clamp providing that the clamp is not aligned to a single crystal axis. However, even when this is done, the effect of the shear components, or any other non-diagonal components of the gradient elastic tensor, on the electric field gradient are not visible in the NMR measurements if the sample's z axis is aligned with the magnetic field (as it is in the S_{11} measurement). However, by rotating the sample with respect to the magnetic field,

$$\mathbf{B} = \begin{pmatrix} B_0 \sin\theta\cos\phi \\ B_0 \sin\theta\sin\phi \\ B_0\cos\theta \end{pmatrix}, \tag{5.40}$$

where θ is the polar angle between the sample's $[0\,0\,1]$ crystal axis and the static magnetic field (whose magnitude is B_0) and ϕ is the azimuth angle of the sample's $[1\,0\,0]$ crystal axis relative to the axis of the NMR coil (see figure 5.12); the Zeeman Hamiltonian (equation 5.9) is no longer diagonal,

$$\hat{H}_z = -\frac{\gamma B_0}{4\pi}\begin{pmatrix} 3\cos\theta & \sqrt{3}\sin\theta\,(\cos\phi - i\sin\phi) & 0 & 0 \\ \sqrt{3}\sin\theta\,(\cos\phi + i\sin\phi) & \cos\theta & 2\sin\theta\,(\cos\phi - i\sin\phi) & 0 \\ 0 & 2\sin\theta\,(\cos\phi + i\sin\phi) & -\cos\theta & \sqrt{3}\sin\theta\,(\cos\phi - i\sin\phi) \\ 0 & 0 & \sqrt{3}\sin\theta\,(\cos\phi + i\sin\phi) & -3\cos\theta \end{pmatrix}. \tag{5.41}$$

The resulting eigenvalues are the same as when no rotation of the magnetic field is considered, as the Zeeman effect is not dependent on the sample's orientation. However, the eigenvectors are now a combination of the basis states, so when the same perturbation approach as for determining S_{11} is taken, these off-diagonal elements become part of the first order corrections. Therefore, the quadrupolar frequency is dependent on the orientation of the sample and the off-diagonal components of the gradient elastic tensor (e.g. shear strain),

$$\begin{aligned} \frac{\nu_Q(\theta,\phi)}{\nu_{Q,\theta=0}} &= 1 - \frac{3}{2}\sin^2\theta \\ &+ \frac{3\epsilon_\eta}{4\epsilon_b}\sin^2\theta\cos 2\phi \\ &+ \frac{2\epsilon_{xy}}{\epsilon_b}\sin^2\theta\sin 2\phi\frac{S_{44}}{S_{11}} \\ &+ \frac{2}{\epsilon_b}\sin 2\theta\left[\epsilon_{xz}\cos\phi + \epsilon_{yz}\sin\phi\right]\frac{S_{44}}{S_{11}}, \end{aligned} \tag{5.42}$$

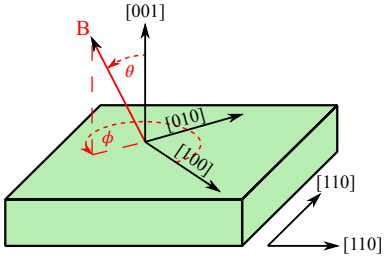

Figure 5.12: Schematic diagram of the angles describing the sample's rotation.

where $\nu_{Q,\theta=0}$ is the same as ν_Q in equation 5.28, that is, where the sample's growth axis is aligned with the magnetic field ($\theta = 0$). From equation 5.42, the quadrupolar frequency depends on S_{44} only through the ratio of $\frac{S_{44}}{S_{11}}$. When significant stress is applied uniaxially along the $[1\,1\,0]$ direction, the resulting strain can be described as,

$$\begin{gathered} \epsilon_b = -\frac{T}{2\left(c_{11}+c_{12}\right)}, \quad \epsilon_{xy} = \frac{T}{4c_{44}} \\ \epsilon_\eta = 0, \quad \epsilon_{xz} = 0, \quad \epsilon_{yz} = 0 \end{gathered} \tag{5.43}$$

where T is the applied uniaxial stress and c_{ij} are the elastic stiffness constants. This can be used to simplify equation 5.42 for quantum dots in the $[1\,1\,0]$ stress configuration,

$$\left(\frac{\nu_Q\left(\theta,\phi\right)}{\nu_{Q,\theta=0}}\right)_{[110]} = 1 - \frac{3}{2}\sin^2\theta - \frac{c_{11}+c_{12}}{2c_{44}}\sin^2\theta\sin 2\phi\frac{S_{44}}{S_{11}}. \tag{5.44}$$

To determine the ratio of the gradient elastic tensor components, a different approach to that taken in the S_{11} measurement is needed, as there are no unambiguous relationships between the NMR and GaAs PL that can be used to cross-calibrate the measurements. Instead, we can measure a small number of dots for multiple orientations of the sample. As each quantum dot is in its own strain environment, the results will not be as simple as they were for the S_{11} work and instead will require multidimensional fitting, detailed later, to produce a value for S_{44} that has a decent accuracy. Whilst measuring quantum dots in the $[1\,1\,0]$ stress configuration will reduce the number of fitting parameters, the equations in 5.43 only consider the externally applied stress, ignoring the quantum dot's intrinsic strain. Therefore, as we cannot measure the same quantum dots with and without applied stress, it is necessary to measure quantum dots in an externally unstressed sample so that the internal biaxial strain for the quantum dots can be approximated.

In equation 5.42, we choose to use the ratio of the gradient elastic tensors, rather than obtaining both S_{11} and S_{44} from the fitting, as we already know S_{11} to a decent accuracy and the extra degree of freedom in the fitting model for the extra parameter will needlessly increase the error in the fitting results.

Rotating the sample with respect to the static magnetic field (i.e. non-zero θ angles) brings certain disadvantages to the measurements. In particular, as the exciton's quantisation axis, $[0\,0\,1]$, is not aligned with the magnetic field, the optical based nuclear spin pumping

will result in the pumped nuclear spins initially aligning with the sample's $[0\,0\,1]$ direction and then precessing to align with the static magnetic field. This has two effects, firstly the level of polarisation achievable through DNP will be reduced (proportionally by $\cos^2\theta$, [33]) and secondly, the detectable nuclear spin polarisation, through the Overhauser effect on the quantum dot's states, will also be reduced. Both of these lead to a reduced NMR signal. In addition to this, due to the high refractive index of GaAs, there is a reduction in the detected PL as the emission, due to total internal reflection, is limited to a small cone centred around the sample's z axis.

5.3.1 Results

Three quantum dots in both an unstressed and $[1\,1\,0]$ stressed sample were measured under a variety of different angle combinations (aiming to maximise and minimise the components in equation 5.42). These quantum dots were located near the edge of the samples to ensure that equation 5.43 is as valid as possible. The orientation, and angle measurement, of the sample was performed at room temperature, with the deflection of laser being used to determine the sample's angle with respect to the magnetic field direction. The sample was then cooled to approximately $4.2\,\mathrm{K}$ for the NMR measurements. The PL spectrum of each dot, under $650\,\mathrm{nm}$ excitation and without an applied static magnetic field, was used to fingerprint the dots so that the same dots could be reliably found under different orientations. Surface features of the sample, primarily from the breaking of the sample into smaller pieces, were used to reduce the search area for each dot, with the fingerprinting used for precise identification.

The value of $\frac{S_{44}}{S_{11}}$, for both $^{75}\mathrm{As}$ and $^{69}\mathrm{Ga}$, is determined by simultaneously fitting the model to the quadrupolar frequencies and orientations for the 6 quantum dots. In addition to the ratio of gradient of elastic tensor components for both isotopes, the model also fits the strain tensor components for the unstressed quantum dots and the magnitude of the external stress for the stressed quantum dots. To account for the lack of internal strain in equations 5.43 for the stressed sample, the average of the biaxial strain for the unstressed quantum dots is added to that in equation 5.43 for the stressed dots. This results in the model having 20 fitting parameters in total for the 6 quantum dots. To estimate the errors in the fitted parameters, a Monte Carlo approach, as described in section 3.4, is used to estimate the $95\,\%$ confidence interval.

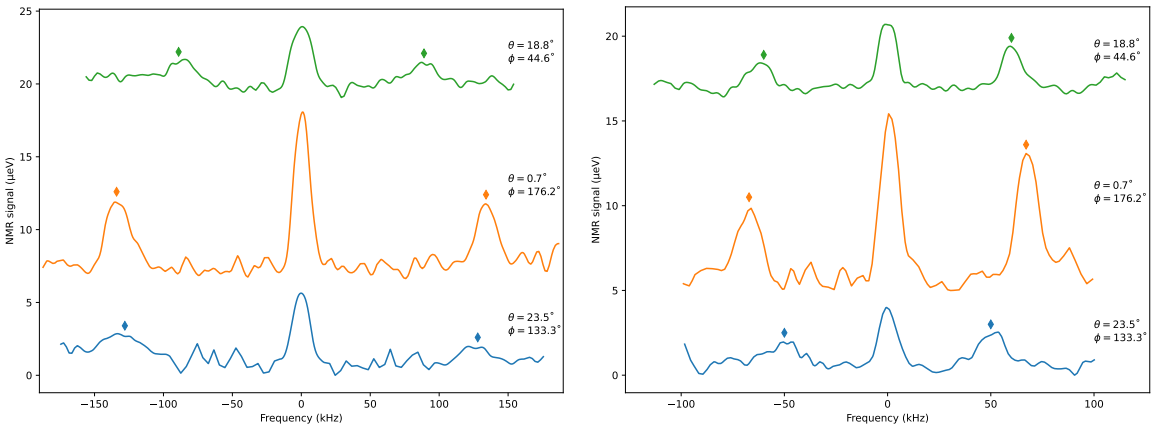

(a) ^{75}As (b) ^{69}Ga

Figure 5.13: NMR spectra for a quantum dot in the $[1\,1\,0]$ stressed sample in three orientations. Markers have been added above the satellite transition peaks.

An example of the effect that the orientation of the sample, with respect to the magnetic field, has on the NMR spectrum is shown in figure 5.13, for a quantum dot in the $[1\,1\,0]$ stressed sample. In the plots for both isotopes, the reduction in the nuclear polarisation, and the resulting NMR signal, with an increasing polar angle (θ) can be seen. Despite this, both satellite transitions can still be resolved; however, there is a practical limit in the region of $25°$ for the polar angle. Figure 5.14 shows the quadrupolar frequency with respect to the polar angle for the three measured quantum dots in the $[1\,1\,0]$ stressed sample. The fitted model is shown by the dashed lines, with the two panes of the graph, joining at $\theta = 0°$, showing the effect that the polar angle has for two azimuth angles on the different isotopes. In particular, with $\phi = 45°$ predominately affecting the quadrupolar frequency of ^{75}As with increasing polar angle, whilst ^{69}Ga is predominantly affected in the opposite direction ($\phi = 135°$), with increasing θ. Whilst there is limited data, all the measured quantum dots have close agreement with each other as well as the fitted model. Figure 5.15 shows the measured quadrupolar frequency for two quantum dots in an unstressed sample, with the centre of each circle indicating both of the angles and the size of the circle representing the quadrupolar frequency. In the case of QD1, the quadrupolar frequency for ^{75}As increases with the polar angle when the azimuthal angle is $45°$ or $90°$, whereas the quadrupolar frequency for ^{69}Ga decreases for these orientations, showing that the sign of $\frac{S_{44}}{S_{11}}$ is opposite for each isotope. The substantial differences in the variation of the quadrupolar frequency with the orientation between the two plots in figure 5.15 is due to non-zero values for either, or both, ϵ_{xz} and ϵ_{yz}.

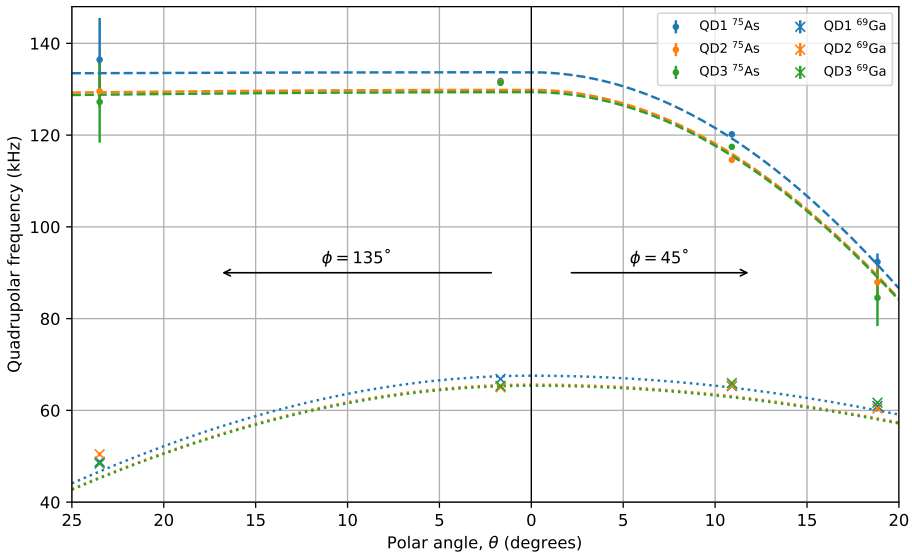

Figure 5.14: Quadrupolar frequency of both $^{75}\mathrm{As}$ and $^{69}\mathrm{Ga}$ for the $[1\,1\,0]$ stressed sample with respect to the sample's polar angle, for two different azimuth angles. The dotted lines are from equation 5.42 using the fitted parameters. For convenience, the quadrupolar frequency, on the vertical axis, is the magnitude rather than the absolute value.

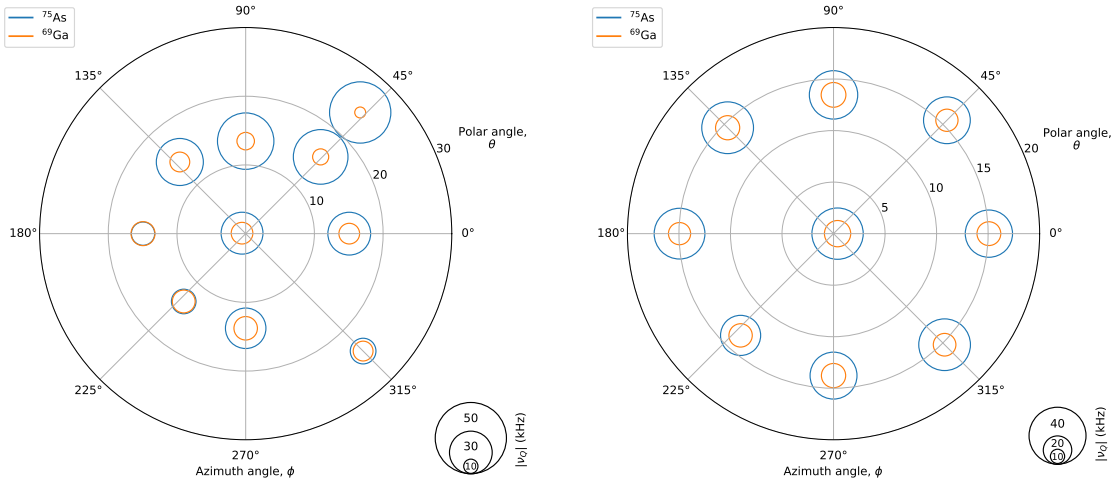

(a) QD1 (b) QD2

Figure 5.15: Quadrupolar frequency for both isotopes with respect to the sample's orientation for quantum dots in an unstressed sample.

The nature of the strain in the quantum dots can be determined by diagonalising the fitted strain tensor, which produces 3 orthogonal principal axes and the magnitude of the strain in those directions for each dot. It is expected that the direction of the largest strain is close

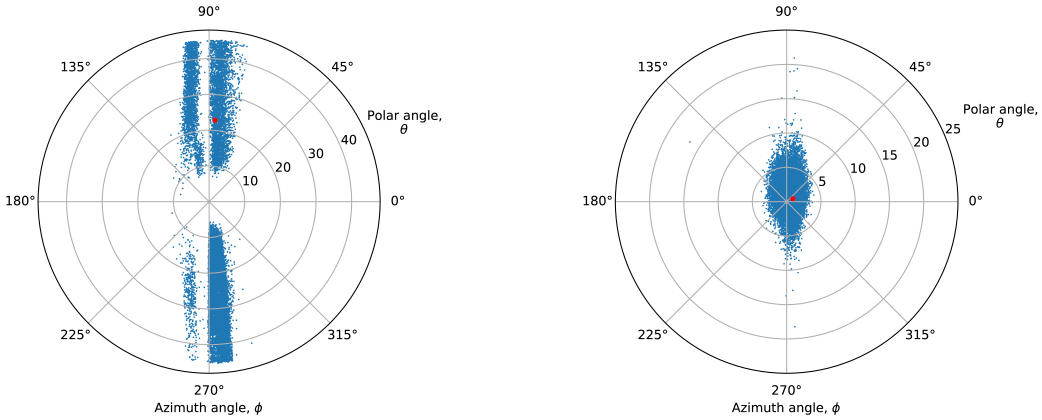

(a) QD1 (b) QD2

Figure 5.16: Direction of the largest principal strain (red) for two of the unstressed quantum dots, with the estimated error in the direction (blue) calculated using Monte Carlo sampling.

to the growth axis. This is true for two of the three quantum dots, where the polar angle is less than $4°$ – an example of one of these (QD2) is shown in figure 5.16. In the case of QD1, this strain axis is approximately $22.8°$ from the growth axis, whilst having a similar magnitude to the other two dots, agreeing with the observations of figure 5.15. Both QD1 and QD2 are fairly close together – within $10\,\mu\text{m}$ of each other – so the difference in their strain environments is likely due to local variations in the growth conditions. As hydrostatic strain can be neglected, the remaining two vectors can be characterised by the difference in their magnitudes and the direction of the largest – this is shown in figure 5.17 for the same two quantum dots. The magnitudes of the differences, and the directions they act in, are substantially different for these two dots, with the magnitude for QD1 being approximately a factor of 3 larger than that of QD2. It is expected that the strain induced by the GaAs / AlGaAs lattice mismatch would not have a preferential direction in the xy plane, so this result is surprising. However, it is worth noting that the terms that contribute to ϵ_1 and ϵ_2 in equation 5.42 (those containing ϵ_η and ϵ_{xy}) have a $\sin^2\theta$ dependency, whereas those that affect ϵ_3 have a $\sin 2\theta$ dependency. As our experiments are limited to $\theta < 25°$, there is reduced accuracy in the ϵ_η and ϵ_{xy} terms of equation 5.42, as the $\sin 2\theta$ term dominates. In figure 5.17, we can see that the estimated confidence region for QD1 is spread predominantly along $\phi = 0°$ and

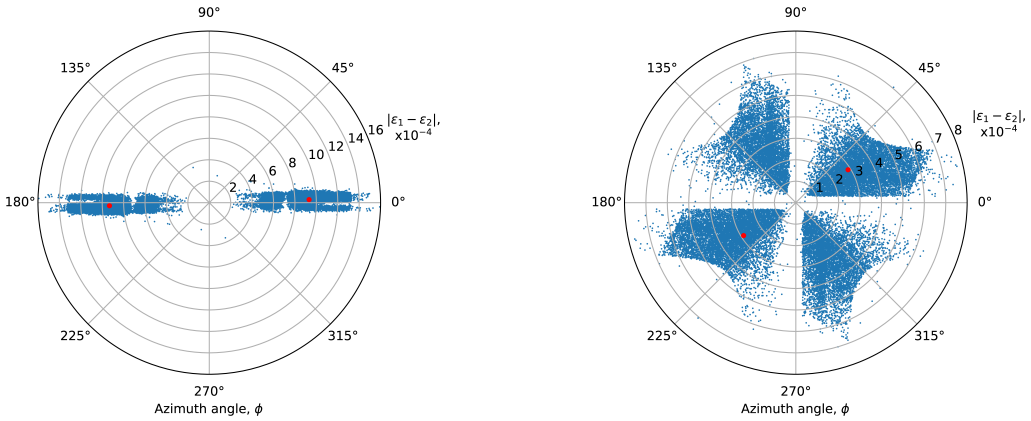

(a) QD1

(b) QD2

Figure 5.17: Difference in the magnitudes of the principal strain components ϵ_1 and ϵ_2, which are in the x and y direction, with respect to the azimuth angle of the largest of the two. The best-fit value shown in red, with the estimated confidence regions from Monte Carlo sampling shown in blue. Due to the definition of the principal strain vectors, each point has an azimuth angle at ϕ and ϕ+180°

has a significant range, whereas QD2 has a smaller radial range but is widely spread over the azimuth angle. It is therefore likely that the fitted polar angle for QD1 is significantly larger than the actual value, with the azimuth angle being fairly accurate. Whereas, for QD2 the reverse can be said, with there being more uncertainty in the azimuth angle than the polar angle.

Due to the size of the errors, the calculated values for the ratio of the gradient elastic tensor components, $\frac{S_{44}}{S_{11}}$, are best expressed as ranges, with the ratio for $^{75}\mathrm{As}$ being in the range of 1.20 to 2.36 and for $^{69}\mathrm{Ga}$ the range of -0.88 to -0.11. Using the results from section 5.2 this gives QS_{44} as approximately $1.40\,\mu\mathrm{V}$ for $^{75}\mathrm{As}$ and $0.19\,\mu\mathrm{V}$ for $^{69}\mathrm{Ga}$.

5.4 Discussion

As with the measurement of S_{11} for GaAs, there has been little previous work published on determining S_{44} (for GaAs). The only notable work is [54], where the $\frac{S_{44}}{S_{11}}$ ratio is 2.0 for $^{75}\mathrm{As}$ and 1.0 for $^{69}\mathrm{Ga}$. We therefore are in quite close agreement for the $^{75}\mathrm{As}$ value of the ratio, but there is quite a significant difference for $^{69}\mathrm{Ga}$. As we are looking at ratios, this removes the systematic errors that explain the difference in the results for the S_{11} values. In addition to this, whilst our measurement is limited to a small range of polar angles which will ultimately

affect the accuracy of our measurement, the fact that a factor of two difference is only present for the one isotope and the other isotope closely agrees, suggests that the source of the error is specific to certain isotopes or nuclei. Our experiment is highly unlikely to have any issues relating to a specific nuclei species and any issues that are caused by interactions of a specific isotope in the sample resulting in a change of the quadrupolar frequency would be present in our S_{11} measurement. However, the absorption in nuclear acoustic resonance (such as that used in [54]) scales as $(QS_{ijkl})^2$ for nuclear spins, and so measurements of lighter nuclei are more susceptible to errors due to other absorption mechanisms. We therefore believe it is likely that the measured value for $^{69}\mathrm{Ga}$ is over-estimated in the previous work.

Chapter 6

Understanding observed up-conversion and DNP phenomena

This chapter investigates the origins of up-conversion and DNP phenomena observed in GaAs/AlGaAs quantum dot samples, that have not been previously reported.

6.1 Up-conversion

An up-conversion mechanism is a process that results in photons being emitted from a material with a higher energy than those the material absorbed. There are many ways that this can occur, which can be broadly categorised on whether they require multiple photons to produce each up-converted photon or if th additional energy is obtained from another source. There are two prominent examples of single photon up-conversion, thermally excited and electrically driven up-conversion. In thermally excited up-conversion, phonons, or other excitations, in the material transfer energy to the optically generated electron-hole pair, resulting in a higher energy emission and the cooling of the material. Each incident photon results in an up-converted photon that has an increase in energy of a few $k_B T$, which is a few hundred $\mu\mathrm{eV}$ at $4.2\,\mathrm{K}$ [58]. In electrically driven up-conversion, an electric bias is applied to the sample so that an electric current is driven through it. Some of these electrons are then trapped in the dot's lowest state. Optical excited holes, from deep states in the barrier, are also trapped by the dot, with their recombination producing the up-converted emission [59].

Whilst some multi-photon up-conversion mechanisms rely on nonlinear properties, such as in parametric up-conversion, the majority rely on an intermediate state, that can either be virtual or real [58]. True two-photon up-conversion is an example of a virtual intermediate state, where two photons are absorbed simultaneously. One photon excites an electron from the ground state to the virtual intermediate state, with the other exciting the electron from the intermediate state to the excited state. As the intermediate state is virtual, the two photons have to be absorbed simultaneously and so requires high intensity excitation that is typically only found in pico- and femto-second pulsed lasers [60]. Two step two-photon up-conversion is similar, but instead has a real intermediate state, allowing the two photons to be separated in time, increasing the efficiency of the up-conversion mechanism. Both of these are diagrammatically shown in figures 6.1a and 6.1b, respectively.

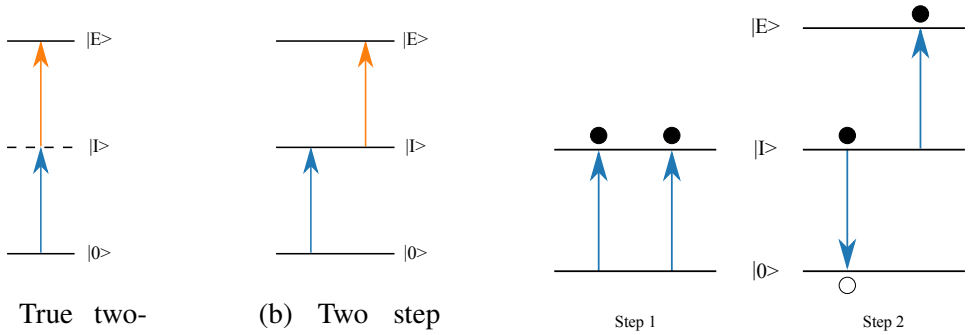

(a) True two-photon

(b) Two step two-photon

(c) Auger

Figure 6.1: Diagrams showing up-conversion processes that use an intermediate state, labelled as $|\mathrm{I}\rangle$, with the ground and excited states as $|0\rangle$ and $|\mathrm{E}\rangle$, respectively.

Auger up-conversion is another example of a mechanism that uses a real intermediate state. Two photons are absorbed, either sequentially or simultaneously, by the intermediate state, with one of the electron-hole pairs non-radiatively recombining, promoting the remaining electron to the excited state (see figure 6.1c). This is substantially more efficient than the other kinds of two photon up-conversion, with it being possible for the up-converted luminescence to have a $50\,\%$ efficiency at high intensities [58, 60]. The intermediate states for these mechanisms can have a variety of different origins, depending on the material and sample structure.

Up-conversion has been observed in bulk materials, such as in CdS, doped GaP and in undoped GaAs, where two step two-photon absorption occurs via Cu impurity levels,

deep donor levels and deep levels in As antisite defects (intentionally added by the growth technique), respectively [61–63]. As well as in epitaxially grown GaAs and AlGaAs layers, where intrinsic defects in the high purity layers provide the intermediate levels [64]. With a two step process, such as two step two-photon and Auger up-conversion, the intensity of the up-converted luminescence should have a quadratic dependence on the excitation power [64], which is the case for the bulk undoped GaAs. In bulk doped GaP, the dependence varies between linear and quadratic depending on the doping level and in the case of the GaAs and AlGaAs layers studied by Quagliano & Nather the dependence was linear, suggesting a saturation of one of the steps in the up-conversion process [62, 64]. It is possible for Auger up-conversion to have a cubic dependence on excitation power if an additional process is required to excite an electron-hole pair into the intermediate state [65].

Up-conversion has also been observed in confined structures, such as quantum wells and quantum dots, where two step two-photon absorption is the dominant process. In a multiple GaAs/AlGaAs quantum well structure, the up-converted PL had a near linear dependence on the excitation power, with the origin of the intermediate levels being attributed to the GaAs wells but with no discussion of the exact up-conversion mechanism [66].

More rigorous studies have been done in InGaAs quantum dots, where the up-converted PL from the dot has a near quadratic (an exponent of 1.8) dependence on the excitation power. Due to the moderate power density and the measurements being performed at low temperature, the up-conversion is likely to be either Auger or two step two-photon absorption. However, the authors were unable to determine which of these mechanisms was responsible [67]. Kammerer et al. observed that the up-converted PL increased as the excitation energy approached that of the wetting layer, concluding that the intermediate levels allowing the up-conversion were related to the wetting layer, rather than being defects in the substrate. In a similar study (also of InGaAs quantum dots), up-conversion from the GaAs barrier was observed when the excitation energy was within the absorption band of the quantum dots [65]. Up-conversion was also observed from a sample where the quantum dots and wetting layer were removed but with a significantly lower intensity and no clear structure to the emission around the energy of the quantum dots, implying an effective mechanism that transfers carriers from the dots to the barrier. The up-converted PL showed a quadratic dependence on the excitation power when the excitation was in the wetting layer and for

low powers when the excitation was in the quantum dots. At higher powers in the quantum dots, the quadratic dependency becomes more linear, which the authors suggest is due to the saturation of the intermediate states. This up-conversion could be due to both Auger and two step two-photon absorption; however, the authors suggest that the Auger process would not saturate with increasing excitation power, with them concluding that two step two-photon absorption is the primary up-conversion mechanism [65].

6.2 DNP

The generation of DNP by a quantum dot is introduced in section 2.5, where for simplicity it is assumed that the lowest, optically active states exchange their spin with the nuclear spin bath through the hyperfine interaction. Whilst this can be an efficient mechanism, it is not the only, or necessarily the dominant, mechanism of generating DNP.

In particular, the generation of DNP through resonant excitation of the optically active (bright) states is typically limited to significantly less than the full polarisation of the nuclear spins due to the probability of the spin exchange being small and the recombination time of the state being too slow, delaying the removal of a spin-exchanged carrier from the dot [68]. An alternative mechanism to this is exciting the normally optically inactive (dark) states, which, due to a reduction of symmetry in the dots, are optically accessible (albeit with a significantly lower oscillator strength than the bright states). These dark states can exchange their spin with the nuclear spins through a second order process, involving a virtual flip to a bright state [69]. If the lifetime of the dark states is significantly longer than that of the bright states, then the generation of DNP is dominated by the spin exchange involving the dark states [10]. These long lifetimes of the dark states means that they can be populated by low power non-resonant excitation [70]. In addition to this, the asymmetry in the energy splitting between the dark and light states, due to the exchange interaction, results in different probabilities for the spin exchange, with the generation of DNP in one direction being more efficient than the other. This can result in the generated nuclear polarisation being independent of the excitation helicity [69].

Excitation with energies that are greater than the quantum dot's lowest states, and with powers that are beyond those required to saturate them, can be significantly more efficient at

generating DNP through the higher excited states and their interaction with multi-excitons. The presence of a quantum well in the sample can provide a large number of short lived states that have a large energy broadening, resulting in a highly efficient DNP pumping mechanism [71]. In a similar way, energy broadening can be achieved through the use of higher temperatures, resulting in an increase in the pumping efficiency [72].

DNP has also been observed in bulk GaAs, by both above and below bandgap excitation [73–75]. In the case of above bandgap excitation, the DNP is generated in a similar way to that described in section 2.5 where the hyperfine interaction allows the spin of an electron to be exchanged with that of a near by nuclei. The electron in the conduction band has an angular momentum that is dependent on the helicity of the excitation laser, allowing the nuclear spin population to be pumped in both directions. Whilst above bandgap excitation has been observed to generate DNP in both intrinsic and doped GaAs, below bandgap excitation does not generate DNP in intrinsic GaAs as the excitation promotes an electron from the valence band to an impurity state in the bandgap [76]. However, the vast majority of un-doped GaAs wafers are not intrinsic GaAs but are semi-insulating – where instead of a perfect crystal, the wafer is grown with defects and is doped to give a similar concentration of dopant acceptors to defect donors, pinning the Fermi level near to the middle of the band gap. This results in similar properties to intrinsic GaAs whilst being considerably easier to manufacture.

Unlike that from above bandgap excitation, DNP generated from below bandgap excitation is not affected by the excitation's helicity and is always positive with respect to the equilibrium [75]. This has been attributed to the quadrupolar interaction, rather than the hyperfine interaction, with the photon absorption and electron recombination of delocalised shallow donor impurity states creating fluctuating electric field gradients. These fluctuations are dependent on the kinetic temperature of the electrons, not their polarisation, and can drive the nuclear spins to the same temperature. However, this effect cannot increase the polarisation above that of the thermal polarisation and so would not be observable in our NMR experiments [77]. If these impurity levels are present, they will also contribute to DNP generation above the bandgap. This can be modelled through the ratio of the quadrupolar and hyperfine relaxation timescales, $f = \frac{T_Q}{T_H}$, with this ratio being the function of the impurity (donor) level occupation (Γ),

$$f = f_0 \frac{\Gamma}{1 - \Gamma}, \tag{6.1}$$

where f_0 is a property of the material [75]. For high intensity, above bandgap excitation, Γ is close to 1, $T_H \ll T_Q$ and so the hyperfine interaction dominates. For the opposite extreme, low intensity and below bandgap excitation, Γ is close to 0, $T_Q \ll T_H$ and so the quadrupolar interaction dominates. In the transition between these two extremes is above bandgap excitation with low intensity, or where the absorption is otherwise reduced. In this regime, it is possible for the quadrupolar interaction to dominate resulting in the same kind of DNP generation as from below bandgap excitation.

An alternative mechanism to the quadrupolar interaction generating DNP is less well defined optical selection rules, where the excitation with one polarisation can excite an electron with either spins. This has been observed with above bandgap excitation in bulk GaAs, with σ^- excitation exciting spin up electrons from the heavy-hole states as well as spin down electrons from the light-hole states. The excited electrons, on average, are predominately spin up with excitation of spin down electrons being 3 times less likely. However, this can vary significantly with the excitation energy [78]. This could equally occur with below bandgap excitation, with an impurity level having less well defined optical selection rules. Like above, if the timescales were different for the hyperfine relaxation of the above and below bandgap states, their ratio could be modelled and would similarly be dependent on the impurity level occupation.

6.3 Experiments

All measurements for the experiments contained in this chapter were performed in the bath cryostat system (described in section 3.2) with four types of measurements being conducted. These were power dependence of the PL spectroscopy, photoluminescence excitation (PLE) spectroscopy, wavelength dependence of the DNP and nuclear spin dynamics.

The power dependence of the PL measurements were performed using non-resonant excitation with the spectrums being detected by using the $1200\,\mathrm{mm}^{-1}$ grating of the single $0.5\,\mathrm{m}$ spectrometer. Each spectrum was taken in a single cycle, with the sample being continuously exposed to the excitation.

The PLE measurements also used a single cycle, continuous approach. However, instead of the power being varied, the wavelength of the excitation was varied around the resonance

of the quantum dot and quantum well. The resulting PL spectra were detected by the double spectrometer.

The wavelength dependence of the DNP uses the pump-probe technique, where the wavelength of the pump laser is varied. The polarisation level of the nuclei is determined by measuring the Overhauser shift of the quantum dot's PL using non-resonant excitation. The length of the pump part of the cycle is long enough to ensure that the DNP has reached a steady state. Each cycle starts with a wide-band NMR pulse to depolarise all the nuclear isotopes. This randomises the nuclear spin environment and ensures that there is no build up of DNP from other excitation wavelengths or the use of multiple cycles to capture each spectra.

The nuclear spin dynamics consist of two measurements that are closely related. These measure the amount of time it takes to pump (build-up) the nuclei to a steady state and how long it takes for the built up polarisation to decay in the dark. The build-up time measurement is similar to the wavelength dependence, except that for each wavelength the length of time that the sample is excited (T_p) with the pump laser is varied. Consequently, these measurements take substantially longer for each wavelength than the wavelength dependence, so only a few wavelengths of interest are chosen to be measured. With the decay time measurement, instead of the pump time being varied, the dark time between the pump and probe pulse (T_d) is varied, allowing the decaying level of the nuclear polarisation to the equilibrium to be measured. Like the build-up time measurement, the time required to measure each pump wavelength is long enough that only a few wavelengths are chosen to be measured.

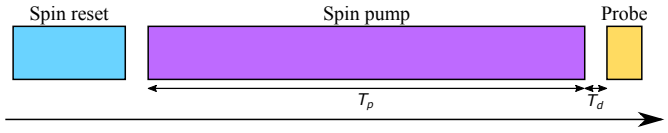

Figure 6.2: Schematic of the pump-probe cycle used in the wavelength dependence and nuclear spin dynamics measurements. T_p is the length of time that the sample is exposed to the pump laser and T_d is the length of time between the pump excitation pulse and the probe excitation pulse.

Each of these measurements tell us something about the quantum dot or its surrounding nuclear environment. The power dependence of the PL, with its non-resonant excitation, allows us to see the optically active states of the quantum dot (and how they change with

excitation power) as well as other features, such as the location of the quantum well. We expect that the intensity of the emission from the lowest energy states of the quantum dot will increase linearly with excitation power until they reach saturation, where their intensities will increase sub-linearly to the point where they do not increase any further. When the lower energy states are saturated, the quantum dot's higher energy states will become visible in the spectra and this will result in a broad spectrum with little detail at high powers [79]. The PLE spectra allow us to precisely determine the states of the quantum dot as they are individually probed with the exciting laser rather than relying on carriers, being generated elsewhere by the above resonance excitation, tunnelling into the dot's states. Because of this, PLE can show additional states that are obscured in PL due to fast relaxation of charge carriers.

The wavelength dependence of the DNP shows us at what wavelengths and powers the most efficient pumping of nuclear spins occurs. We expect there to be no nuclear spin pumping for excitation with photon energies below the quantum dot band gap. For excitation that is resonant with or above the band gap of the dot, the efficiency of the spin pumping can be quite complicated, but at a very basic level, we expect higher excitation powers to generate more DNP (up to a limit) and that excitation that is far away from the dot or the quantum well to be less efficient. In a similar way, the spin build up times can be complicated, but generally the high levels of DNP will be accompanied by fast build up times.

6.4 Results

Unexpected phenomena were observed in three samples – unstressed pieces of sample B and sample C, and a piece of sample B externally stressed along the $[1\,1\,0]$ direction (using a clamp as described in section 5.2).

6.4.1 Sample B (120 nm barrier)

Unstressed

Figure 6.3 shows the measured DNP, through the Overhauser shift, for quantum dot 1. The figure is split into two panes, with the top pane showing the measured DNP when using σ^+ polarisation of the pump layer and the bottom pane showing the DNP for the σ^- polarisation.

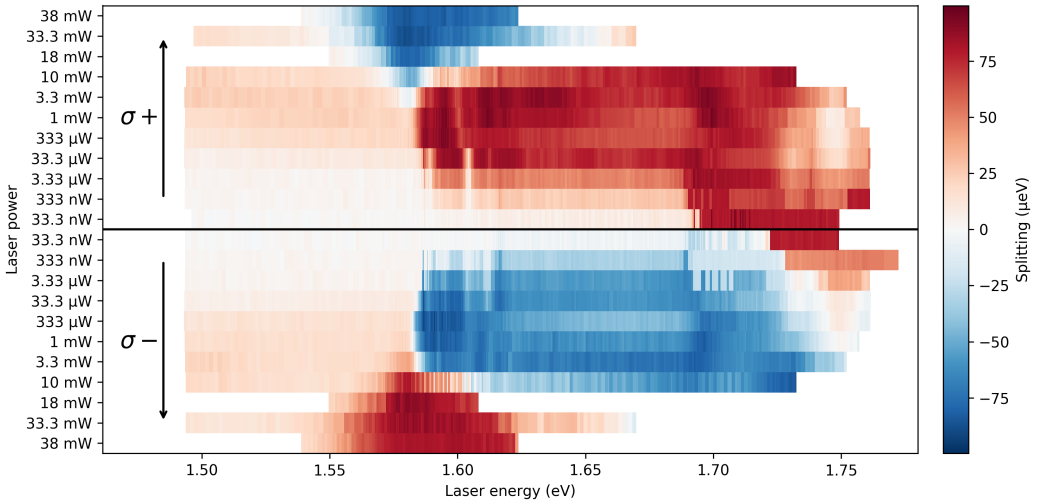

Figure 6.3: Wavelength dependence of DNP of quantum dot 1 in sample B.

The figure is arranged so that the lowest excitation power of the pumping laser is where the two panes meet, with the excitation power increasing in opposite directions, as indicated by the arrows on the left hand side of the figure. Figure 6.4 consists of two plots, (a) shows a

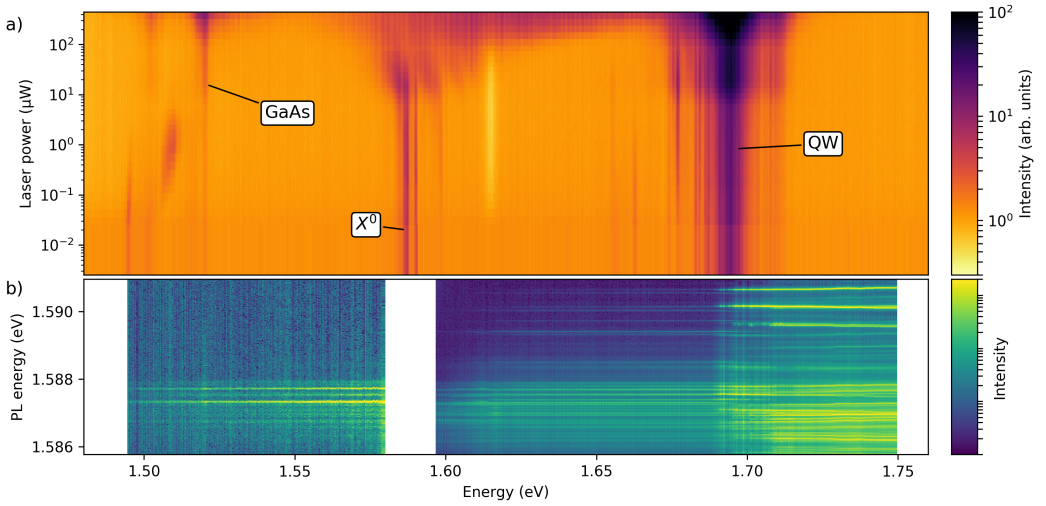

Figure 6.4: Power dependence of PL (a) and PLE spectra (b) of quantum dot 1 in sample B.

power dependence of the PL spectra when the dot is excited with $1.94\,\mathrm{eV}$ laser light and is annotated to show the two lines that are emitted from the Zeeman split states of X^0, the lines from the GaAs emission and the bright lines that result from emission from the quantum well (labelled as QW). The second plot, (b), shows the PLE spectra, where the vertical axis is the energy of the detected PL, with the break in the data on the horizontal axis being slightly larger than the width of the data in the vertical axis. This plot has two different scales for the

data on the left and right of the break (i.e. for the data that corresponds to emission with less, and more, energy than the X^0 emission) as the magnitude of the emission is significantly different for the two regions, hence why the scale bar for the plot does not have numerical values.

There are three prominent features that are visible in figure 6.3 – the reversal of DNP at high powers near the dot's X^0 emission, the positive DNP at low powers at higher energies than the quantum well with a limited reversal for low powers of σ^- excitation and the positive DNP from sub-band excitation that increases with excitation power. In addition to this, figure 6.4 shows that up-conversion is present in the PLE spectra, with emission from the dot being produced by excitation with a lower energy than the dot's X^0 state. Figure 6.5 shows the

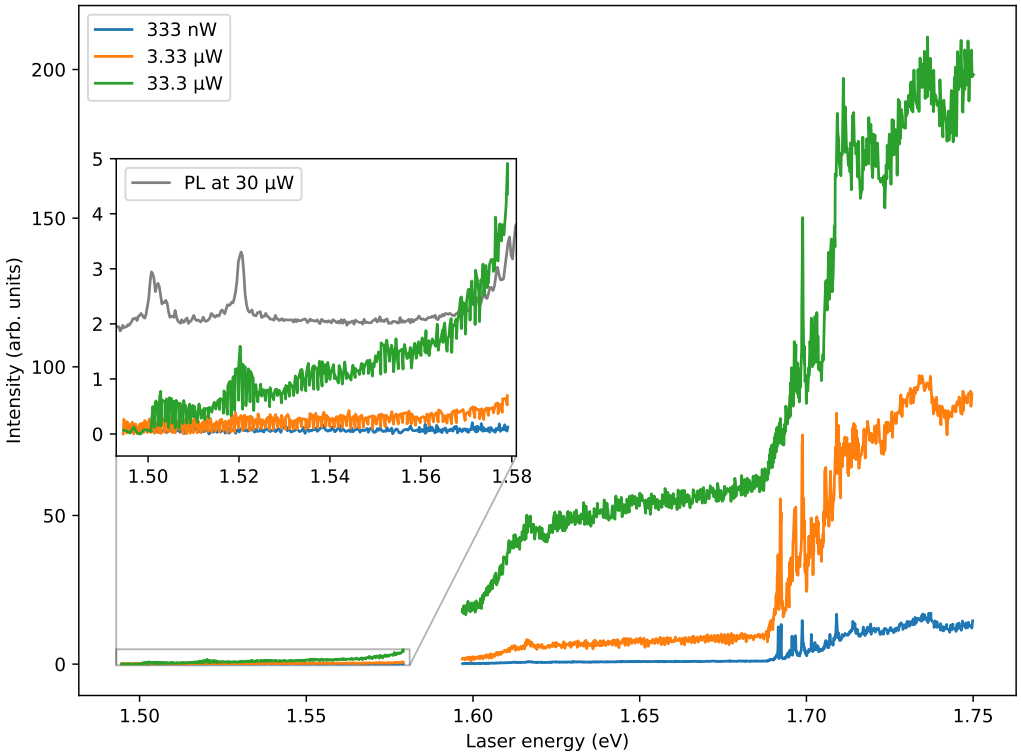

Figure 6.5: Integrated PLE of quantum dot 1 in sample B, across the X^0 emission (1.586 to $1.591\,\mathrm{eV}$). The inset plot additionally shows a PL spectrum in grey.

integrated PLE for the same dot, which generally has broad features for the three measured powers for excitation energies that are less than the quantum well. There are two features in the up-conversion, just above $1.50\,\mathrm{eV}$ and at $1.52\,\mathrm{eV}$, which correlate fairly well with the GaAs peaks visible in PL.

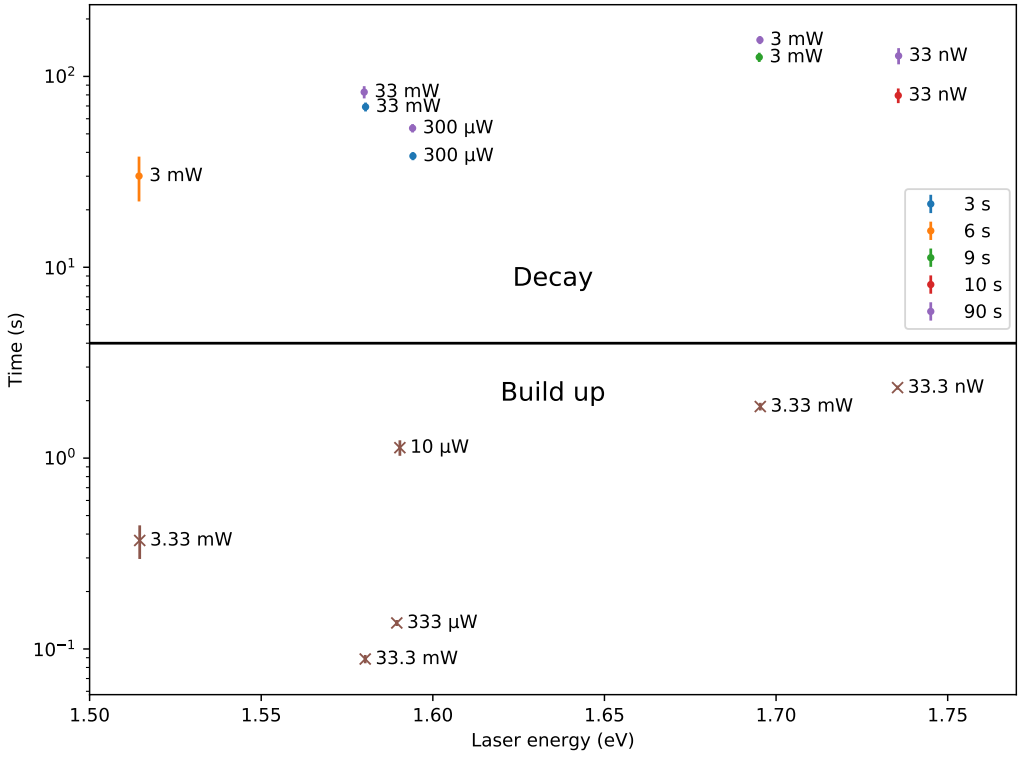

Figure 6.6: Nuclear spin polarisation build-up and decay times of quantum dot 1 in sample B. The powers next to the data points is the power used for pumping. For the decay data points, the length of time used for pumping is shown in the legend.

Figure 6.6 shows the results of the nuclear spin dynamics measurements, with the figure split into two panes – the top being for decay measurements and the bottom being for build-up measurements. The fastest pumping, with respect to excitation power, occurs near the dot's resonance (approximately $1.59\,\mathrm{eV}$) and is significantly faster than the pumping that results from exciting the quantum well ($1.70\,\mathrm{eV}$). The reverse pumping that is just below X^0 ($1.58\,\mathrm{eV}$) at high powers, is significantly faster than pumping into the quantum well and is similar to what would be expected if it was resonant with the dot (and the inversion did not occur). The pumping at low powers just above the quantum well ($1.74\,\mathrm{eV}$) has a similar build-up time to high power pumping into the quantum well, despite its significantly lower power, whilst having similar decay times. The pumping below X^0 ($1.51\,\mathrm{eV}$), resulting from up-conversion, appears to be faster than pumping with the same power into the quantum well. However, the level of these two polarisations is significantly different by approximately a factor of 3 (see figure 6.3, with the pumping times differing by approximately a factor of 5.

Figure 6.7 shows the wavelength dependence of the DNP of a second dot in sample B, with figure 6.8 showing the power dependence of the PL and the PLE. From both of these

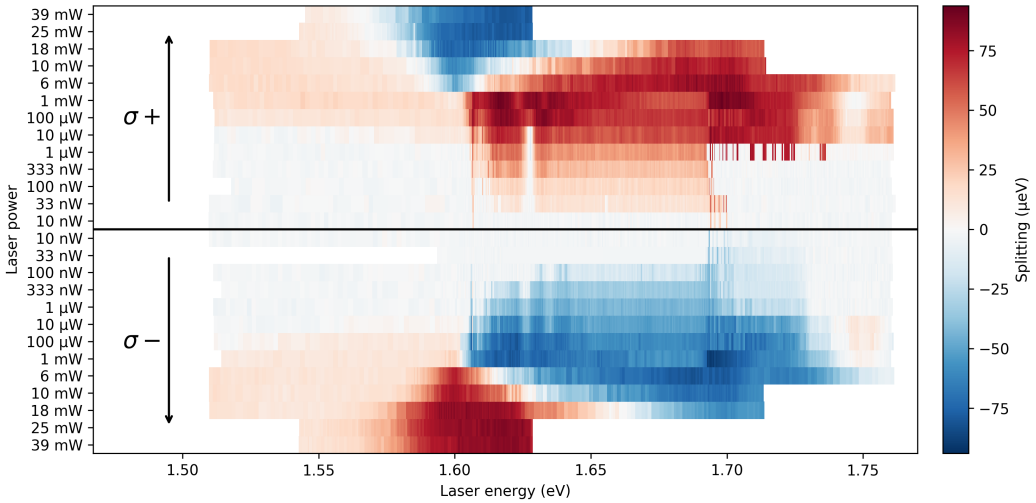

Figure 6.7: Wavelength dependence of DNP of quantum dot 2 in sample B.

figures, it can be seen that the results for this dot are largely similar to that of dot 1, with up-conversion being present in the PLE spectra, positive DNP in the wavelength dependence from sub-bandgap excitation and the reversal of DNP at higher powers around the dot's X^0 emission. There is, however, one noticeable difference between the two dots for low powers above the quantum well. Where there was efficient pumping for σ^+ and a reversal happening

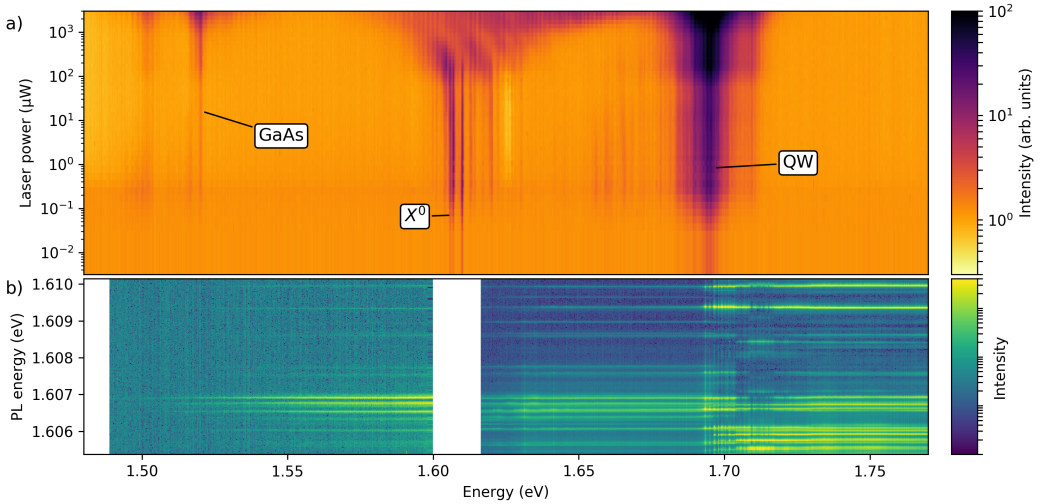

Figure 6.8: Power dependence of PL (a) and PLE spectra (b) of quantum dot 2 in sample B.

for σ^- excitation greater than $1.72\,\mathrm{eV}$ (up to around $3.3\,\mathrm{mW}$) in dot 1; for dot 2, we do not see any pumping of nuclear spins above the quantum well for the lowest powers of σ^+ excitation, with there being a small amount of pumping for σ^-. There is only a small amount of reversal for σ^- between $10\,\mu\mathrm{W}$ and $6\,\mathrm{mW}$; however, this feature does look remarkably similar to that seen in dot 1.

Figure 6.9 shows the integrated PLE for dot 2. Unlike the PLE spectra for dot 1 (figure 6.5), the PLE spectra for dot 2 does not have the same features that correlate with the GaAs PL lines (although there is a very small increase around $1.52\,\mathrm{eV}$ which could be related). Instead, there is a small increase around $1.54\,\mathrm{eV}$, which does not correlate to any lines observed in the PL spectra.

Externally stressed along $[1\,1\,0]$

Figure 6.10 shows the wavelength dependence of the DNP, with figure 6.11 showing the power dependence of the PL and PLE of a quantum dot in sample B which is under compressive stress along the $[1\,1\,0]$ direction. When compared with the dots in the unstressed sample there are two large differences – there is no reversal of the DNP polarisation around the dot's X^0 emission at high powers and there is no up-conversion observed in the PLE spectra. There is also no reversal of the nuclear spin polarisation at low powers for excitation energies greater than that of the quantum well; however, this was only seen in one of the externally unstressed dots. For excitation with energies below X^0, there is some polarisation

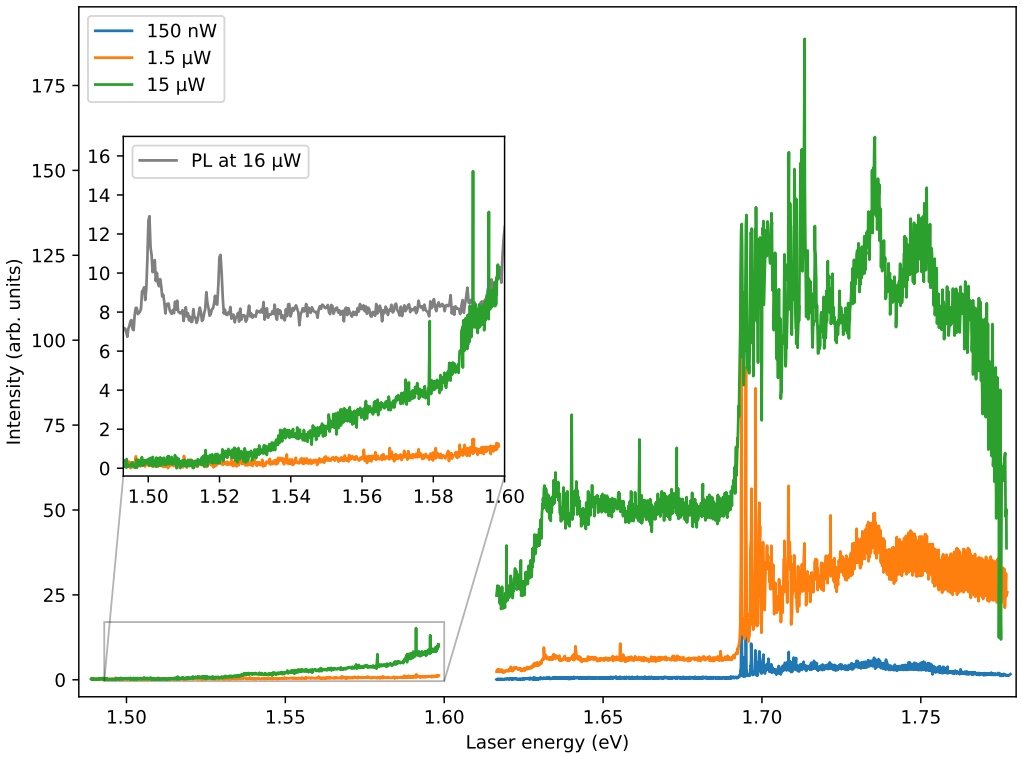

Figure 6.9: Integrated PLE of quantum dot 2 in sample B, across the X^0 emission (1.605 to 1.610 eV). The inset plot additionally shows a PL spectrum in grey.

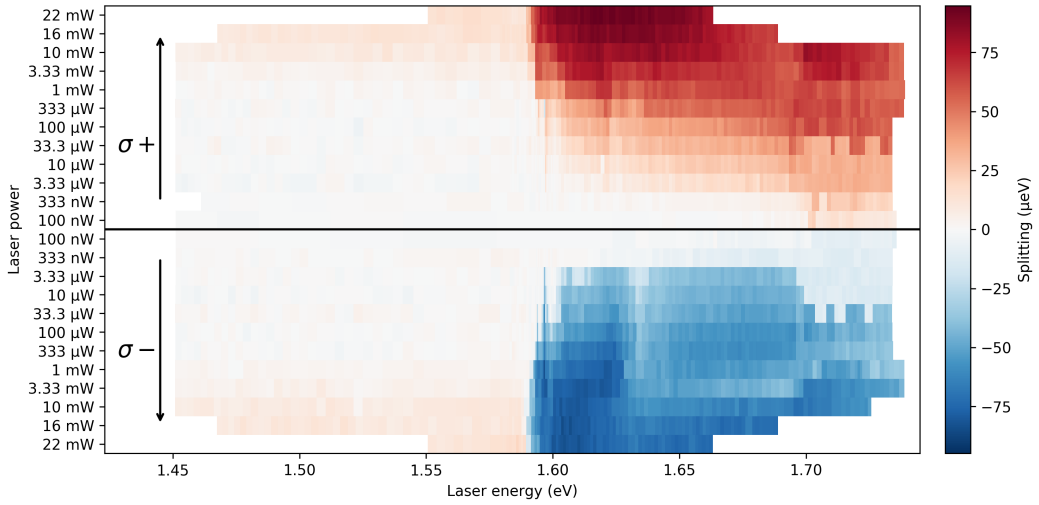

Figure 6.10: Wavelength dependence of DNP of quantum dot 1 in the stressed sample B.

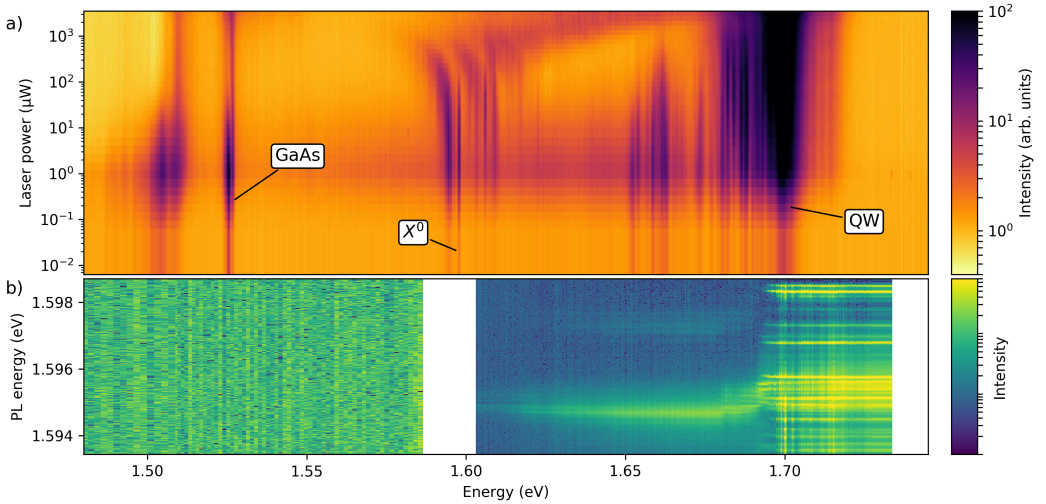

Figure 6.11: Power dependence of PL (a) and PLE spectra (b) of quantum dot 1 in the stressed sample B.

generated; however, the maximum polarisation level is significantly less than that observed in the unstressed sample ($10\,\mathrm{meV}$ compared to $20\,\mathrm{meV}$) and requires significantly more excitation power to be reached ($16\,\mathrm{mW}$ compared to $1\,\mathrm{mW}$). This suggests that this mechanism responsible for nuclear polarisation with excitation energies below X^0 is around an order of magnitude less efficient in the externally stressed sample. In addition to this, polarisation of the nuclear spins was observed for excitation energies of $1.45\,\mathrm{eV}$, which is significantly less than the GaAs emission lines observed in the PL spectra[1]. The power dependence of the PL in figure 6.11a shows that the emission from both the bulk GaAs and the quantum well are significantly brighter than in the unstressed sample.

The integrated PLE for the dot is shown in figure 6.12. The shape of this graph is different to the results for the unstressed sample, where instead of a fairly sharp increase just above the dot's X^0, with the PL being nearly constant until just below the quantum well, we see a steady increase until the quantum well band gap, where the PL jumps in brightness.

Figure 6.13 shows the results of the nuclear spin dynamics measurements for this dot. The pumping time when resonant with the dot is shorter than in the unstressed sample by a factor of approximately 4.7, whilst the decay times are quite similar. Pumping below the dot is significantly slower by approximately 7.9 times. The decay time when pumping into

[1]It is worth noting that smaller excitation energies were used with the externally stressed sample than with the unstressed sample for this measurement. We, therefore, cannot say that polarisation of the nuclear spins does not occur at $1.45\,\mathrm{eV}$ in the unstressed sample.

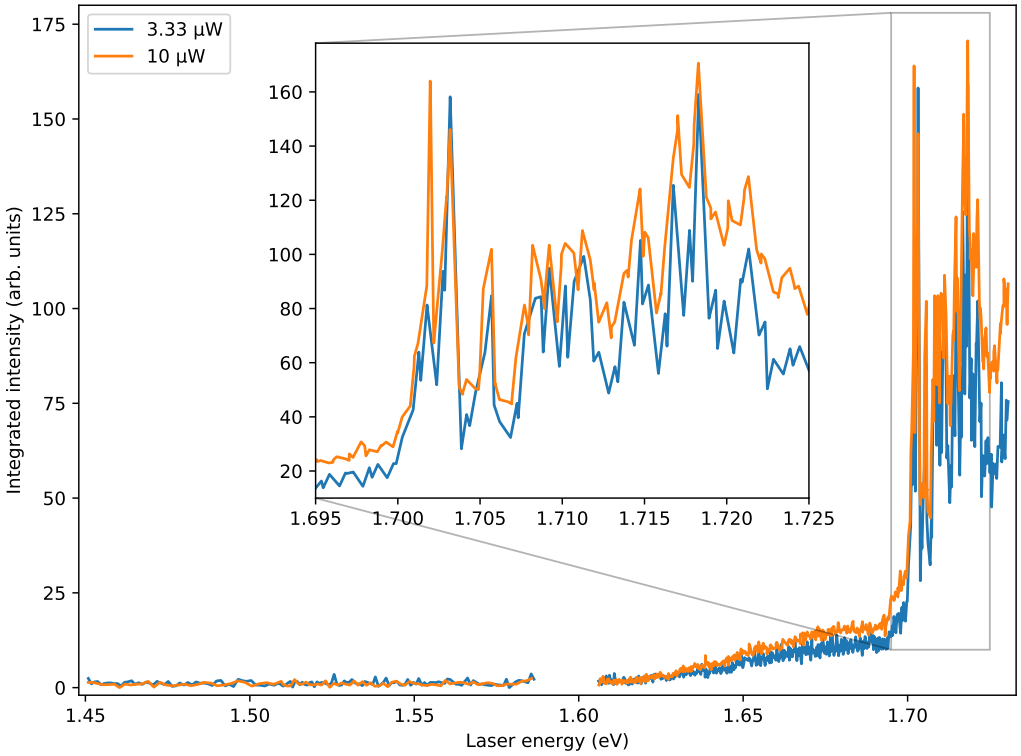

Figure 6.12: Integrated PLE of quantum dot 1 in the stressed sample B, across the X^0 emission (1.593 to $1.599\,\mathrm{eV}$). The inset plot additionally shows a PL spectrum in grey.

the quantum well is approximately 3 times quicker than for the unstressed sample and has a peculiarity in that the decay time largely does not change when pumped for 3, 10 and 90 seconds.

6.4.2 Sample C (12 nm barrier)

Figure 6.14 shows the wavelength dependence of the DNP, with figure 6.15 showing the power dependence of the PL and the PLE of a quantum dot in sample C, with all three having significant differences to those for sample B. There is no up-conversion observed in the PLE spectra and the GaAs feature in the PL power dependence is significantly brighter (although this may be due to the difference in the quality of the surface of the samples). The wavelength dependence of the DNP does show spin pumping occurring from below the dot excitation, with there being a very strong feature seen around $1.50\,\mathrm{eV}$ between $1\,\mathrm{mW}$ and $10\,\mathrm{mW}$ which is independent of the polarisation of the excitation. There is no reversal at high powers near the dot's X^0 emission; however, there is a reduction in the polarisation for both

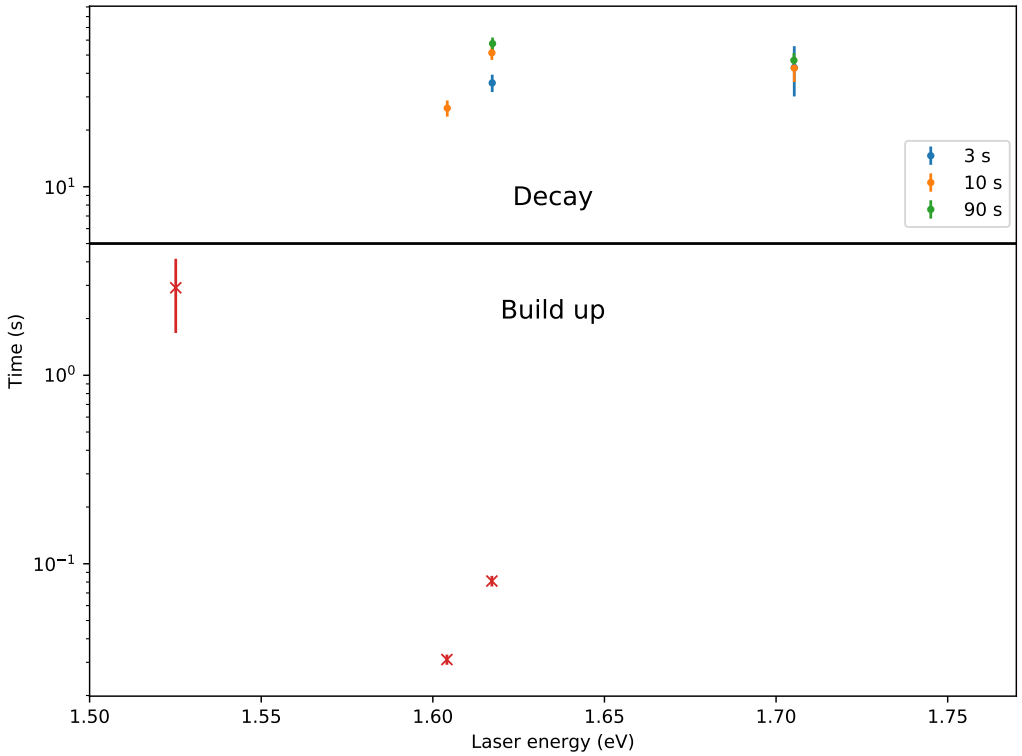

Figure 6.13: Nuclear spin polarisation build-up and decay times of quantum dot 1 in the stressed sample B. All of the points had an excitation power of $22\,\mathrm{mW}$ with the exception of the points at $1.70\,\mathrm{eV}$ which had an excitation power of $11\,\mathrm{mW}$.

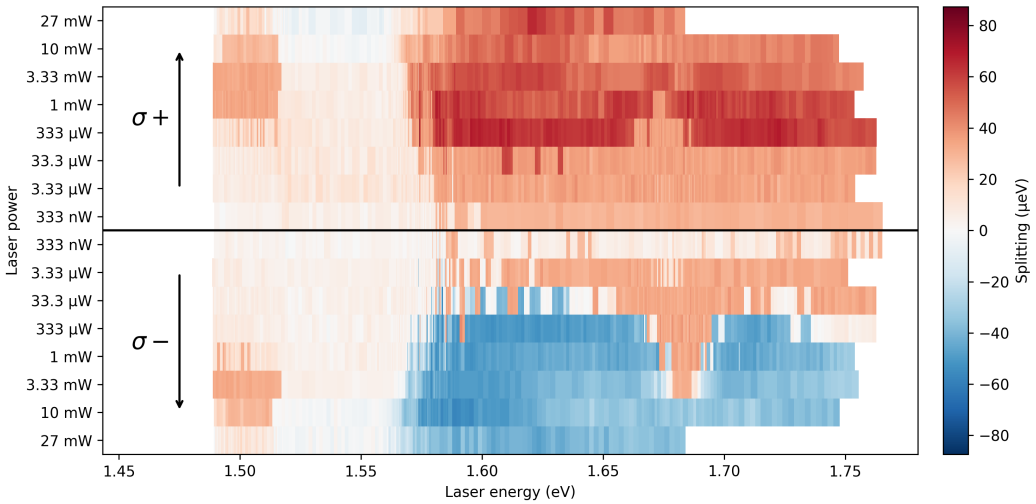

Figure 6.14: Wavelength dependence of DNP of quantum dot 1 in sample C.

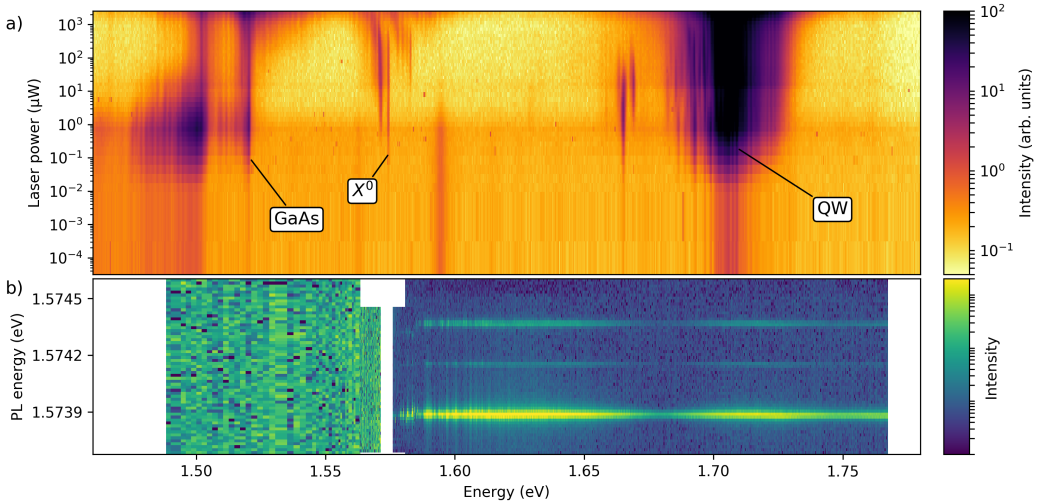

Figure 6.15: Power dependence of PL (a) and PLE spectra (b) of quantum dot 1 in sample C.

σ^+ and σ^- pumping at high powers ($10\,\mathrm{mW}$ and $27\,\mathrm{mW}$) below the dot, compared to lower powers with the same excitation energies. Pumping with an excitation power of $3.33\,\mu\mathrm{W}$ in either optical polarisation results in a very similar level of polarisation, which is also reversed for σ^-. This is different to what was seen for dot 1 in sample B, as the reversal only occurred above the quantum well at low powers, whereas here it occurs for any excitation above the dot's resonance. There is a feature, just below the quantum well at approximately $1.68\,\mathrm{eV}$, where σ^- pumping results in an inverted polarisation for all but the highest powers used.

Figure 6.16 shows the integrated PLE for the same dot, where no up-conversion is present. There is a dip in the PLE around the same energy as the feature in the wavelength dependence of the DNP ($1.68\,\mathrm{eV}$). As this dip means that the absorbed excitation is not producing luminescence (or at least luminescence in the observed spectral range), it is likely that the photons are being absorbed by the dot and then are quickly, and efficiently, tunnelling out of the dot due to the thin AlGaAs barrier.

Figure 6.17 shows the results from the nuclear spin dynamics measurements. As with the dots in sample B, as well as what is expected, the fastest spin pumping and the longest spin decay times are produced from excitation that is resonant with the dot. This spin pumping is approximately 17.5 times faster than in sample B and results in a decay time that is approximately 3.8 times longer. Pumping into the quantum well ($1.70\,\mathrm{eV}$) is also faster than in sample B, but instead by a factor of approximately 4. The pumping with excitation energies

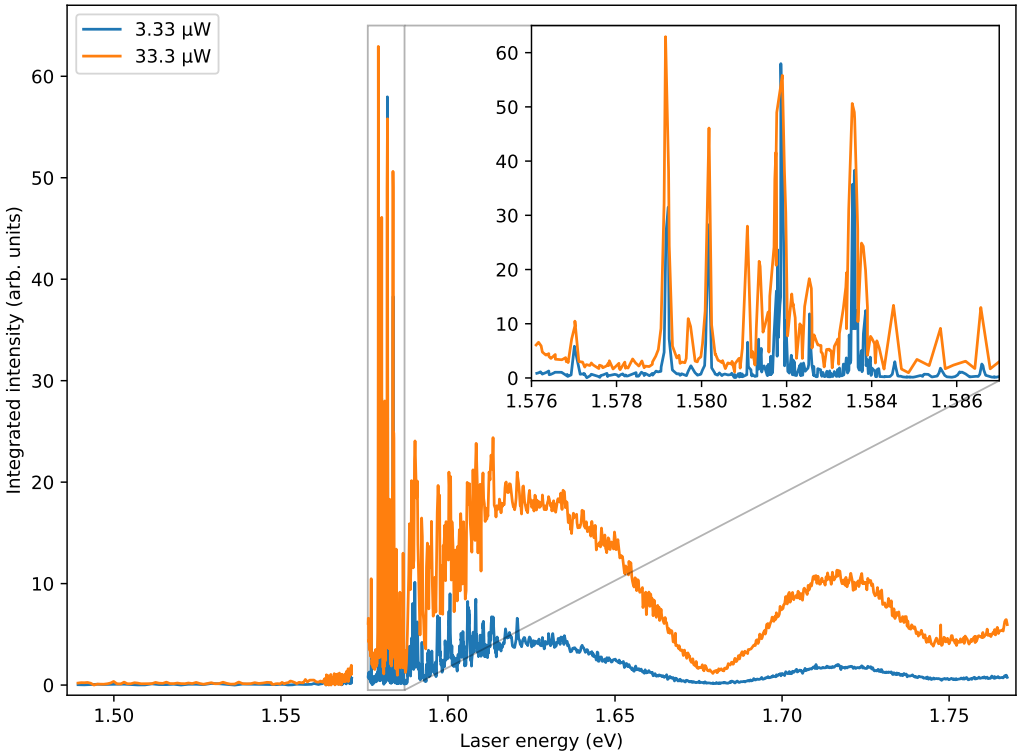

Figure 6.16: Integrated PLE of quantum dot 1 in sample C, across the X^0 emission (1.573 to $1.575\,\mathrm{eV}$). The inset plot additionally shows a PL spectrum in grey.

below X^0 is significantly slower than that seen in sample B by a factor of 8.7. Whilst the polarisation is higher here at $1.50\,\mathrm{eV}$ than in sample B, this would not increase the pumping time to this extent.

6.5 Discussion

From the results, there are some common features observed in the samples, which we will discuss separately.

6.5.1 Up-conversion observed in PLE

Up-conversion in the PLE is only observed in sample B when it is not externally stressed and is not observed in sample C. The PLE spectra for the two quantum dots in sample B both have a similar shape. Whilst dot 1 has two features that correlate with the GaAs peaks

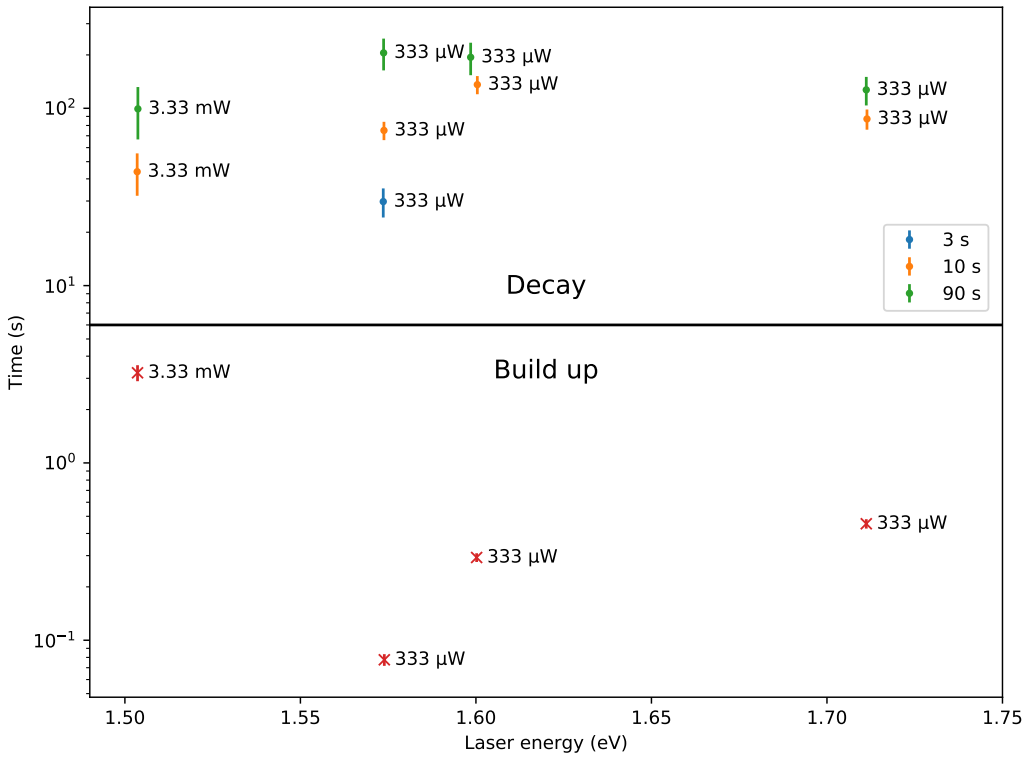

Figure 6.17: Nuclear spin polarisation build-up and decay times for quantum dot 1 in sample C.

observed in the PL spectra, this is not the case for dot 2. The PLE for both of the dots reaches a plateau approximately $24\,\mathrm{meV}$ above the dot's X^0.

From figures 6.4b and 6.8b, it appears that the up-converted PL emission begins at different points in the measured excitation energy range - with all measured excitation resulting in PL emission for dot 1 and only excitation above approximately $1.50\,\mathrm{eV}$ resulting in emission for dot 2. However, this is not the case – figure 6.18 shows a single PL spectrum for each dot with their respective PLE spectra and it can be seen that the emission from X^0 is visible at the lowest excitation energy used for both dots. In addition to this, figure 6.18 shows that, in both cases, emission is produced when the excitation energy is below the bulk GaAs bandgap.

Figure 6.19 shows the power dependence of the up-converted PL from the PLE measurement for quantum dot 1 in sample B. The intensity of the up-converted PL is well described by a linear function with respect to the excitation power, with the exception of the lowest measured power. As the excitation powers are low, the mechanism is most likely to involve a two step process (such as two step two-photon or Auger up-conversion) with the interme-

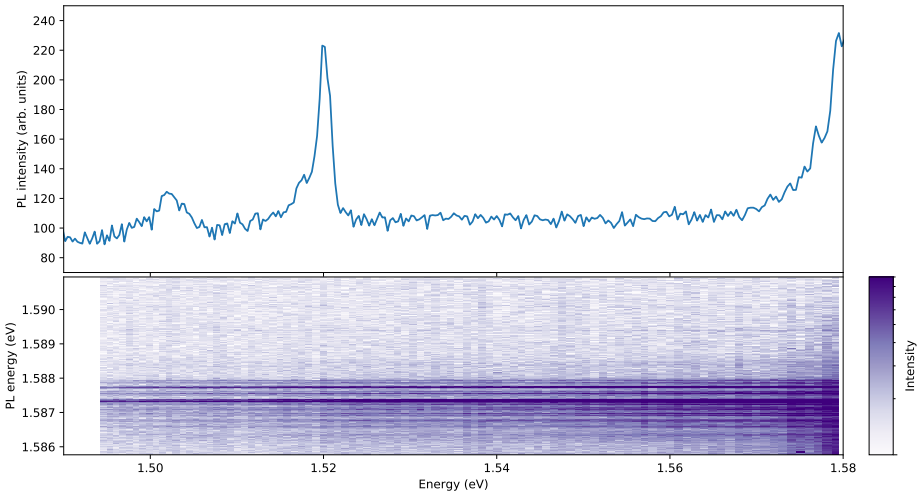

(a) Quantum dot 1

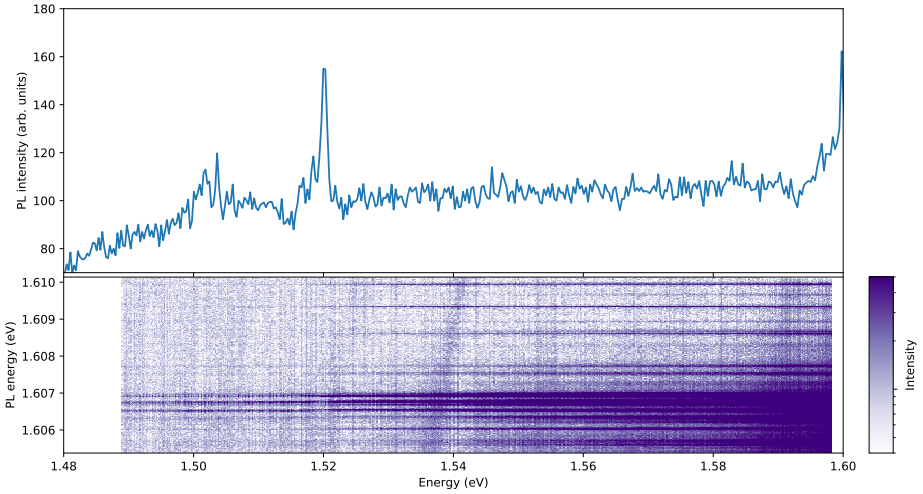

(b) Quantum dot 2

Figure 6.18: Comparison of the up-converted PL observed in the PLE measurements (bottom) to the PL spectra (top) for two quantum dots in sample B. The PL spectra, due to the energy range, show the GaAs emission at each dots' location.

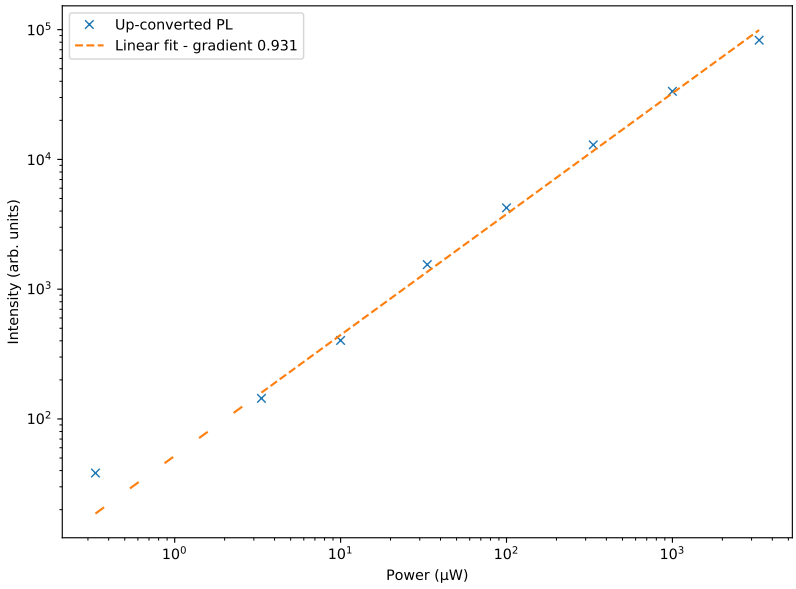

Figure 6.19: Power dependence of the up-converted PL of quantum dot 1 in sample B.

diate level being saturated at low powers, resulting in a linear power dependence. Out of the two step processes, the mechanism is most likely to be Auger up-conversion as the efficiency of the up-conversion appears to be fairly high.

Whilst it is not possible to conclusively identify the origin of the intermediate level, we can reduce the possible origins based on the collected data. As we are detecting the up-

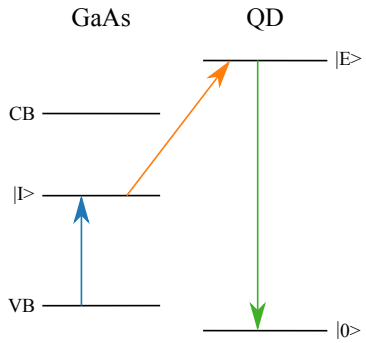

Figure 6.20: Energy diagram showing the up-conversion process when the emission from the quantum dot is being detected. The blue arrow represents the exciting of an electron from the valence band (VB) to an intermediate state ($|\mathrm{I}\rangle$). The orange arrow represents the exciting of an electron from the intermediate to an excited state in the quantum dot ($|\mathrm{E}\rangle$), with the green arrow representing the emission that is detected from the dot's excited state. The annotations CB and $|0\rangle$ are for the conduction band and the ground state of the quantum dot, respectively.

conversion through the emission from the quantum dot states (see figure 6.20), the energy

of the up-converted electron must be equal to or larger than the energy of the quantum dot state producing the detected emission. Therefore, for the up-conversion to be a two step process, the intermediate level must have an energy, relative to the valence band, that is at least half that of the observed emission. From figure 6.21, the largest observed up-converted emission was at approximately $1.610\,\mathrm{eV}$ and so the lower limit on the intermediate level's energy is approximately $0.805\,\mathrm{eV}$ above the valence band. In addition to this, the lowest excitation energy used puts an upper limit on the energy of the intermediate level, with the lowest used in our experiment that produced up-conversion being $1.489\,\mathrm{eV}$, requiring that the intermediate level is less than $1.489\,\mathrm{eV}$ above the valence band.

The sample consists of two materials, GaAs and $Al_{0.4}Ga_{0.6}As$, that have different band gaps, with the GaAs bandgap being the smaller at $1.52\,\mathrm{eV}$ (at $4.2\,\mathrm{K}$). The $Al_{0.4}Ga_{0.6}As$ is lattice matched to the GaAs and its conduction and valence bands will be offset from those of GaAs. For the conduction band, it is $0.34\,\mathrm{eV}$ above that of GaAs, with the valence band being $0.20\,\mathrm{eV}$ below that of the GaAs, resulting in a bandgap of $2.06\,\mathrm{eV}$ for the $Al_{0.4}Ga_{0.6}As$ [47]. The intermediate level will be due to an impurity or defect in either of the two materials. The above values are for bulk material, with the energies of the states increasing for confined materials. In the case of the quantum well, the bandgap increases from $1.52\,\mathrm{eV}$ to approximately $1.69\,\mathrm{eV}$. Whilst the $Al_{0.4}Ga_{0.6}As$ barrier is a confined material, at a thickness of $120\,\mathrm{nm}$ (for sample B) the increase in energy of the states will be very small and so we will consider impurity and defect states in the barrier to be equivalent to those in bulk material.

The vast majority of impurities (e.g. carbon, silicon, germanium, nickel and copper) result in levels in GaAs and AlGaAs that are either too close to the conduction band (i.e. within $10\,\mathrm{meV}$) or are too close to the valence band for them to be a possible source of the observed up-conversion [41]. The exceptions to this are chromium, titanium, oxygen and hydrogen. A chromium impurity results in an acceptor level that is $0.63\,\mathrm{eV}$ below the conduction band, but the presence of chromium during the growth of the sample is highly unlikely. A titanium impurity results in two levels - an acceptor level and a donor level, both are below the conduction band by $0.23\,\mathrm{eV}$ and $1.00\,\mathrm{eV}$, respectively. Whilst titanium is present in the reactor used to grow the samples, the doping level required to create defects is quite significant and is unlikely to have been caused accidentally [80, 81]. An oxygen impurity results in two donor level that are $0.4\,\mathrm{eV}$ below the conduction band and $0.67\,\mathrm{eV}$

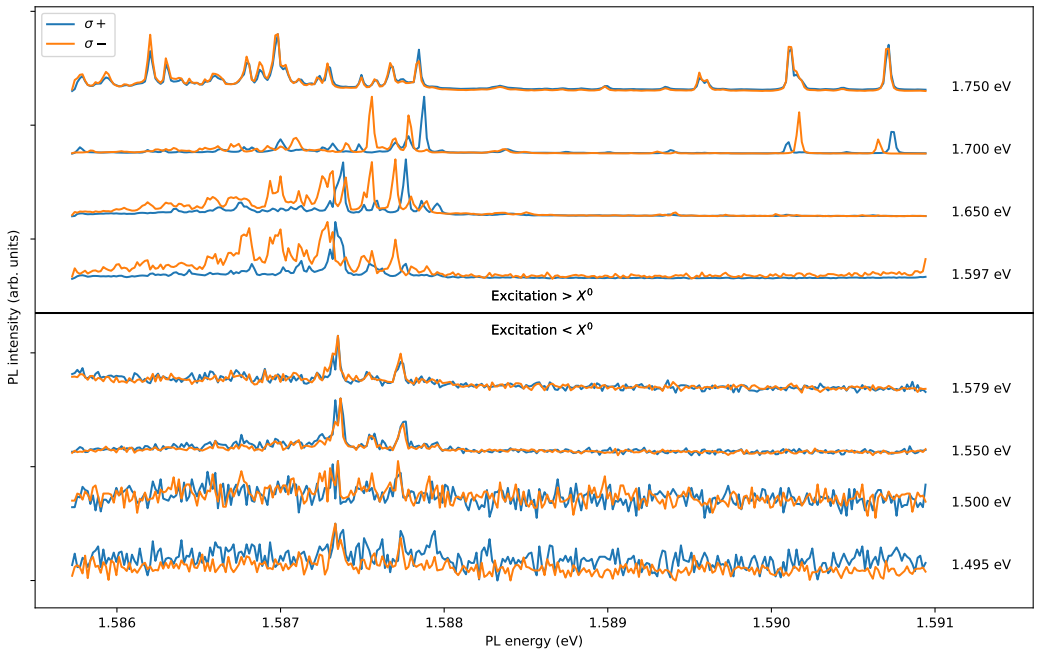

(a) Quantum dot 1

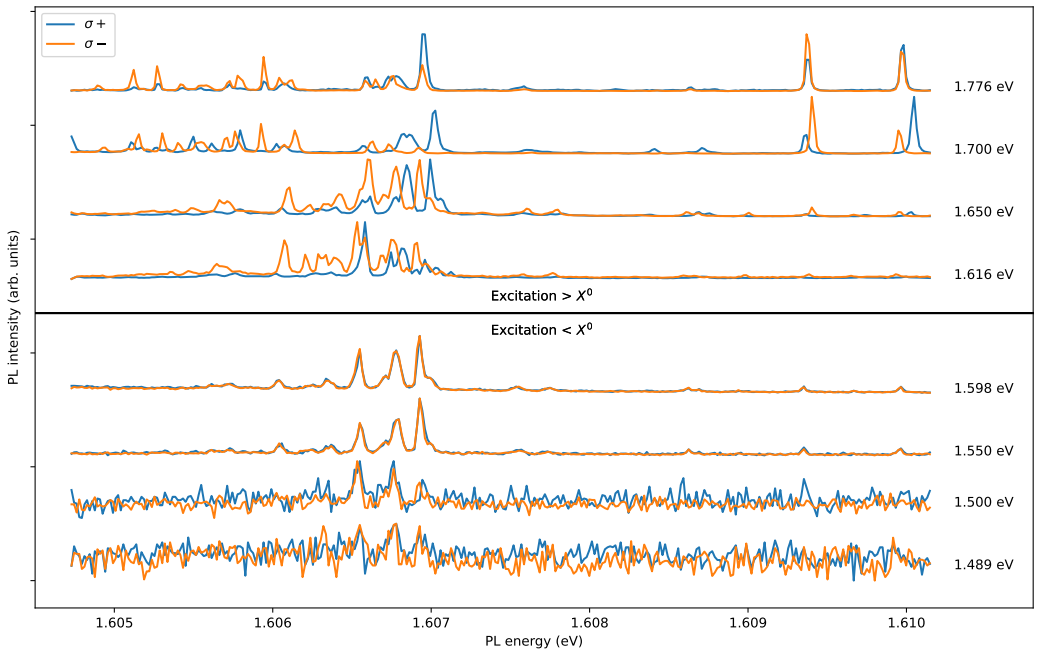

(b) Quantum dot 2

Figure 6.21: Normalised PL spectra of the two quantum dots in sample B for a range of excitation energies, as annotated to the right of each spectrum.

above the valence band [41]. Finally, a hydrogen impurity results in a donor level that is $0.75\,\mathrm{eV}$ below the conduction band.

In addition to impurities, the intermediate level could have its origin in a crystal defect. The only defect that can be present in either bulk or MBE grown GaAs, or AlGaAs, that could potentially be the origin of the intermediate level is the EL2 defect. This defect, commonly referred to as an As anti-site defect, is where an arsenic atom is located where a gallium atom should be in a perfect crystal. Whilst the number of EL2 defects in a sample can be increased by growing the material in an arsenic rich environment, the defect is always present in GaAs [82]. The EL2 defect has two donor levels, one is $0.75\,\mathrm{eV}$ below the conduction band whilst the other is $0.54\,\mathrm{eV}$ above the valence band [83]. However, the EL2 defect has a metastable state where the defect level becomes optically and electrically inaccessible, with it only being possible to remove the defect from the metastable state by heating the sample to above $125\,\mathrm{K}$. This metastable state is achieved by optical exciting the defect with energies between 1.04 and $1.3\,\mathrm{eV}$ [84]. A summary of these impurity and defect levels is shown in

Origin	Type	Energy (eV)
Chromium	Acceptor	$E_c - 0.63$
Titanium	Acceptor	$E_c - 0.23$
Titanium	Donor	$E_c - 1.00$
Oxygen	Donor	$E_c - 0.40$
Oxygen	Donor	$E_v + 0.67$
Hydrogen	Donor	$E_c - 0.75$
EL2	Donor	$E_c - 0.75$
EL2	Donor	$E_v + 0.54$

Table 6.1: Relevant impurity and defect levels for up-conversion, with their energy shown relative to either the conduction (E_c) or valence (E_v) band.

table 6.1, with figure 6.22 showing the levels with respect to the required energy range in bulk GaAs and $Al_{0.4}Ga_{0.6}As$ as well as GaAs in the quantum well.

During the growth of these samples, the MBE reactor had an atmospheric leak that was progressively getting worse. Unfortunately, the extent of the leak or the resultant level of impurities it introduced into the reactor is unknown. The likely impurities that the leak could have introduced are carbon, hydrogen, nitrogen and oxygen. Of these, hydrogen and oxygen are the only two that are relevant as carbon creates an impurity level that is too close to the valence band for the observed up-conversion (see figure 6.22) and nitrogen is largely inert.

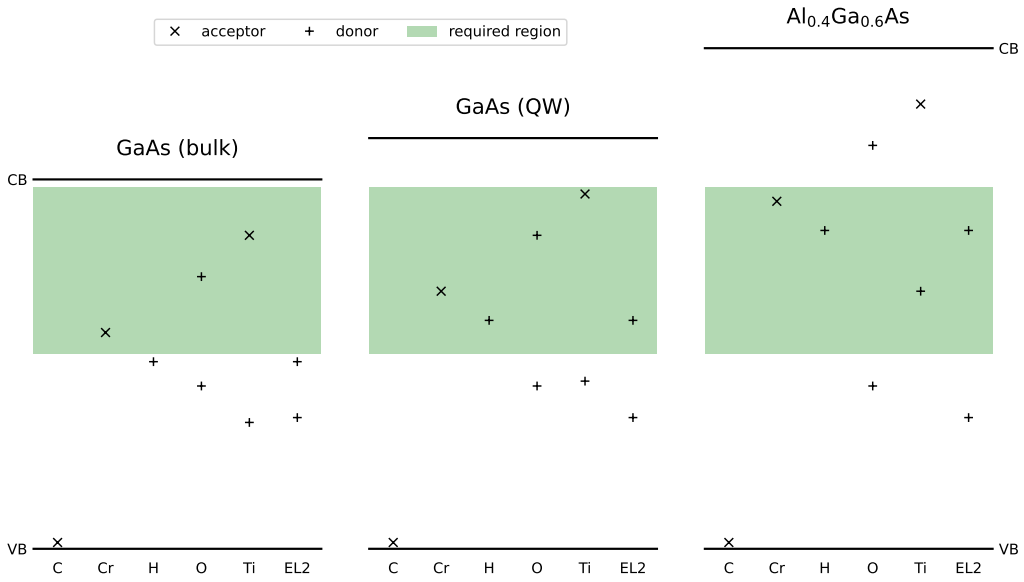

Figure 6.22: Impurity and defect levels in bulk GaAs, the confined GaAs of the quantum well and bulk $Al_{0.4}Ga_{0.6}As$ in relation to the conduction and valence bands (show as CB and VB, respectively) of each material. The possible energy range for the intermediate level is shaded green.

To further reduce the possible origins, it is important to consider the physical location of the impurity or defect. If it is located in the $Al_{0.4}Ga_{0.6}As$ material then it will be in the barrier in which the quantum dots are etched into, potentially placing the intermediate level very close to the quantum dot. The GaAs material is in several places in the sample - the bulk material, the capping layer, and the quantum well. Both the bulk material and capping layer are $120\,\mathrm{nm}$ away from the dot and so are highly unlikely to be part of an efficient up-conversion mechanism. The quantum well, however, is fairly close to the dots and so is a possible location for the impurity or defect level.

Combining this with the likely impurities, the intermediate level is likely to be either due to a hydrogen impurity in the $Al_{0.4}Ga_{0.6}As$ barrier, or a hydrogen or oxygen impurity in the quantum well. It is also possible for the intermediate level to be due to an EL2 defect in either the barrier or quantum well. These potential origins for the intermediate level are summarised in table 6.2.

It is worth noting that whilst sample C was grown after sample B, and so would be expected to have a higher level of impurities, no up-conversion is observed in sample C. We attribute this to the significantly smaller barrier in sample C, allowing the generated carriers

Origin	Type	Energy (eV)
Hydrogen in $Al_{0.4}Ga_{0.6}As$	Donor	1.31
EL2 in $Al_{0.4}Ga_{0.6}As$	Donor	1.31
Oxygen in GaAs QW	Donor	1.29
Hydrogen in GaAs QW	Donor	0.94
EL2 in GaAs QW	Donor	0.94

Table 6.2: Summary of impurity and defect levels that are potentially responsible for the observed up-conversion.

at the impurity levels to tunnel away from the quantum dot and into the bulk GaAs before they can be excited into the dot (through either of the two step mechanisms).

6.5.2 DNP from excitation energies less than X^0

DNP that is generated by excitation energies that are less than the quantum dot's X^0 is observed in all samples. Whilst the up-conversion observed in the PLE spectra of the unstressed sample B is a possible mechanism for this, it does not explain why the DNP is observed in sample B when it is externally stressed and in sample C, suggesting that there is an additional mechanism.

In the unstressed (as grown) sample B, the below dot DNP has a slower build-up time than DNP produced by resonant optical excitation of the dot, but is faster than pumping into the quantum well. As the below dot DNP is faster than pumping into the quantum well, this suggests that it is most likely to be related to the up-conversion seen in the PLE. Whilst it is possible that the polarisation could be generated through the up-conversion mechanism, it is more likely that the impurity or defect states responsible for the up-conversion are directly contributing to the polarisation.

For the externally stressed sample B, where there is no up-conversion in the PLE, the build-up time for the below dot DNP is significantly slower than that in the unstressed sample B, suggesting that there is an additional mechanism generating below dot DNP. This would also suggest that this mechanism is present in the unstressed sample B, with it contributing less to the polarisation than the mechanism related to the up-conversion.

In sample C, the below dot DNP feature visible in the wavelength dependence of the DNP is only strongly present between $1\,\mathrm{mW}$ and $10\,\mathrm{mW}$ and is accompanied by a region of DNP with smaller polarisation at higher energies (but still less than X^0). The build-up

time for this strongly polarised feature is significantly slower than both resonant pumping and pumping into the quantum well, with the decay time being significantly shorter. This suggests that there are two separate process, one which is likely to be similar to that seen in the externally stressed sample B and one that is unique to this sample. This second mechanism only becomes efficient at high excitation powers and is localised in excitation energy, but becomes less efficient at spin pumping at the highest excitation powers used.

We therefore have three different mechanisms that are generating the DNP for excitation energies less than X^0 - one that is related to the up-conversion intermediate level, one that is present in all samples and one that produces higher levels of polarisation in sample C (at high powers and lower excitation energies). As the excitation is below the bandgap of the materials in the sample, the DNP is being produced by an impurity or defect state. However, this state does not have to be the same as those that could produce up-conversion in the PLE measurement, as described in the previous section, as there are no restrictions on the energy range that the impurity or defect level has to be in (other than it has to be equal or less than the excitation energy).

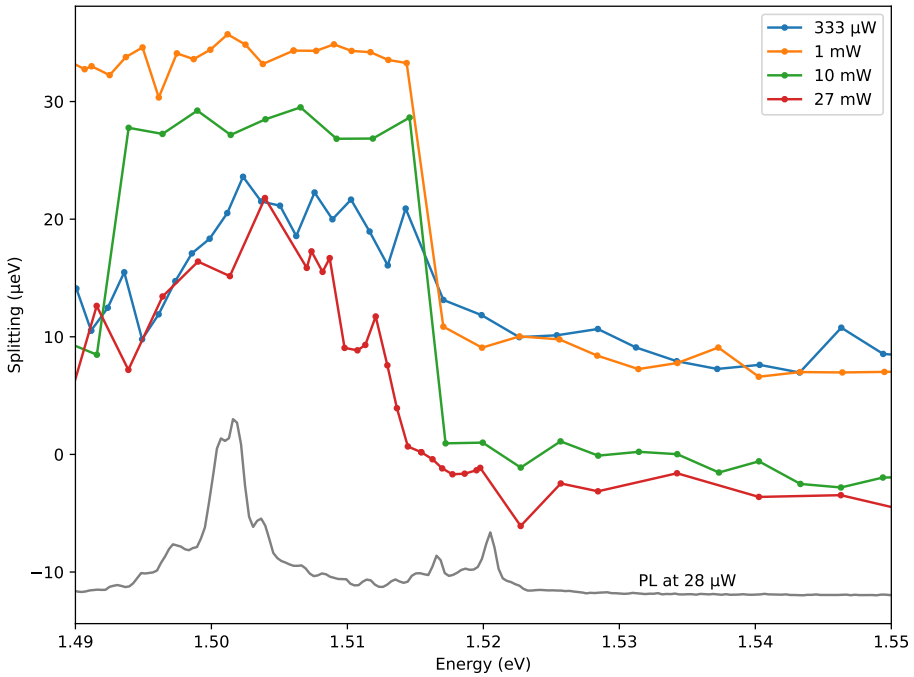

Figure 6.23: Wavelength dependence of DNP for excitation energies around the GaAs peaks observed in PL for quantum dot 1 in sample C. A PL spectrum for the dot is shown in grey at the bottom of the graph.

Figure 6.23 shows the wavelength dependence of DNP for selected excitation powers for the quantum dot in sample C as line graphs with a PL spectrum for the same dot. Here we see that the higher polarisation does not extend in excitation energy beyond $1.52\,\mathrm{eV}$ - the bandgap of bulk GaAs. In addition to this, the peak in the PL spectrum around $1.517\,\mathrm{eV}$ coincides with both a sharp decrease in the generated polarisation (at 1 and $10\,\mathrm{mW}$) and a previous reported broad emission peak, between 1.490 and $1.505\,\mathrm{eV}$, observed in PL from carbon impurities added to create semi-insulating GaAs [76]. Whilst we cannot definitively say that the observed PL peak in figure 6.23 is due to the same impurity, as the spectrum was taken with far above bandgap excitation and we do not have a relevant PLE measurement, it is highly likely to be related to the bulk GaAs.

We, therefore, potentially have a link between the observed nuclear spin polarisation and the bulk GaAs, which is unexpected. Generally speaking, the bulk material is too far away from the quantum dots for their nuclear spins to affect those of the dots or to be observed by the dot. However, in this sample, the distance between the dot and the bulk GaAs is around $7\,\mathrm{nm}$ (as the nanoholes the dots are grown in are around 4 to $5\,\mathrm{nm}$ deep). This is still a long distance for nuclear spin diffusion, making any diffusion slow and very inefficient. But at high powers, it might be possible for this diffusion to have an effect on the polarisation observable by the dot.

Unfortunately, there are a wide range of impurity and defect states that could be producing the DNP. Whilst we can attribute the one mechanism (in the unstressed sample B) to be due to the same level as in the up-conversion, this still results in a range of possibilities in both the barrier and quantum well. In the case of the mechanism only observed in sample C, we can potentially say that it is due to a level (perhaps carbon) in the bulk GaAs. For the last mechanism, present in all samples, it is likely to be due to a level in the barrier or quantum well, but we cannot be more precise than that.

The independence of the generated polarisation and the excitation helicity is likely due to the optical selection rules being less well defined - that is both helicities being able to excite carriers with the same spin. This has previously been reported for above bandgap excitation and there is no reason why this could not occur for an impurity or defect level [78].

6.5.3 Helicity independent DNP at low powers in sample C

In the wavelength dependence of DNP for the quantum dot in sample C (figure 6.14), similar levels of polarisation are observed at low powers (e.g. $3.3\,\mu\mathrm{W}$) above the energy of X^0 for both excitation helicities. This level of polarisation is greater than that generated below X^0 for the same power, but is similar to the maximum level of polarisation that is observed from the GaAs feature (below $1.52\,\mathrm{eV}$ and between 1 and $10\,\mathrm{mW}$). Whilst these both could be due to the same mechanism, it is unlikely as there is a substantial difference in the generated polarisations (at the same excitation power) and the feature around the GaAs PL peaks does not extend very far towards X^0. It is, therefore, more likely that the level of polarisation observed in these two different regions is being limited and the mechanisms behind them are different. As to the mechanism for the above X^0 DNP, the generation of DNP from dark exciton states has previously been observed to be dominant at low powers and can also be independent of the excitation helicity, which could explain our observations [70].

6.5.4 Inverted DNP polarisation below QW in sample C

In figure 6.16, there is a significant dip around $1.68\,\mathrm{eV}$, where the quantum dot is nearly transparent. The width of this dip decreases with excitation power and the centre, which has a non-zero intensity, increases with excitation power. The origin of this transparency could either be due to the charge carriers, from the absorbed photons, quickly tunnelling out of the excited state (be it in the dot or elsewhere) or the photons being absorbed by states whose recombination does not result in emission from the quantum dot.

The dip observed in the PLE, correlates well with the positive polarisation feature just below the energy of the quantum well for σ^- excitation in figure 6.14. In addition to this, a decrease in the polarisation for the σ^+ excitation is seen at slightly lower excitation energies for the same powers. Both of these features have a very similar level of polarisation as the helicity independent DNP at lower powers, and this is highly unlikely to be a coincidence. Therefore, the most likely explanation is that these are due to the bright exciton states not being excitable at energies just less than the quantum well. However, the dark exciton states are still excitable, allowing the same level of polarisation to be generated as at lower powers.

Whilst this explains what is observed, the reason for the bright exciton states to become unexcitable for these energies is not understood, although it is likely that the small barrier plays a part.

6.5.5 Reversal of DNP near X^0 at high powers in sample B

Both quantum dots in the unstressed sample B show a reversal of the generated nuclear polarisation around their X^0 emission at excitation powers above $3\,\mathrm{mW}$, with the width of the reversal (in terms of excitation energy) increasing with excitation power. The low energy side of this increasing width is present in all the samples, albeit without the polarisation reversal, and is due to the sample being heated by the excitation. The higher sample temperature broadens the dot's states allowing for a more efficient generation of DNP [72]. The broadening of the dot's states can be seen in the power dependence of the PL spectra in figures 6.4a, 6.8a, 6.11a and 6.15a. It is interesting to note that the broadening of the states in the power dependence of the PL for the dots in the unstressed sample B is similar to the increasing width seen in the wavelength dependence of the DNP. This is not the case for the externally stressed sample, where the low energy side of the polarisation's increasing width stays considerably closer to the energy of X^0. This will be due to the strain affecting and limiting the overlapping of the dot's states with the nuclear spins. The lack of the reversal feature for the externally stressed sample is related to this and so we can deduce that the reversal of polarisation is related to the states in the quantum dot. Further to this, the build-up time for this reversal feature is similar to the resonant build-up time for other samples, with it being faster than the resonant build-up time of the same sample - although this is highly likely to be due to different excitation powers being used.

As to the origin of the reversal, it could potentially be due to the interplay of light- and heavy-hole excitons, which have opposite spin to each other when excited with the same helicity; or potentially the relaxation of trions hitting a bottle-neck, with it being quicker for them to undergo a spin flip before relaxation than relaxation alone.

6.6 Summary

In summary, these previously unreported phenomena have a variety of origins. The observed up-conversion in sample B is likely to be Auger up-conversion involving either a hydrogen impurity in the $Al_{0.4}Ga_{0.6}As$ barrier, an EL2 defect in either the barrier or GaAs quantum well or a hydrogen or oxygen impurity in the GaAs quantum well. The generation of DNP with excitation energies less than X^0 are likely due to the same up-conversion impurity or defect in the unstressed sample B, impurity or defects in the quantum well or $Al_{0.4}Ga_{0.6}As$ barrier in all samples and potentially an impurity or defect in the bulk GaAs for high powers in sample C. The helicity independence of the DNP at low powers in sample C for excitation energies greater than X^0 is most likely due to dark excitons, with the inverted polarisation for σ^- excitation around $1.68\,\mathrm{eV}$ being the same effect combined with the bright excitons being optically inaccessible at these excitation powers. Finally, the reversal of DNP at high powers in sample B around X^0 is related to states in the quantum dot, but the mechanism for the reversal is currently not known.

Chapter 7

Summary and future work

Whilst somewhat brief and outside the main scope of this thesis, the initial characterisation of the fabricated Schottky diode InGaAs quantum dot samples has been used as part of other work (see [38]). The accurate measurement of the gradient elastic tensor for GaAs is a significant step forward in aiding the modelling of NMR, with applications in structural analysis of quantum dots, as well as furthering the understanding of the effects of strain on electron-nuclei interactions and how these affect the lifetime and coherence of spins. Our measurement, as detailed in chapter 5, is substantially more accurate than the previous work. However, whilst our measurement of the S_{11} component could not be significantly improved, the accuracy of the measurement of the S_{44} could be. As the S_{44} component is only observable when the sample is rotated, with respect to the magnetic field, it is beneficial to perform the experiment over the entire range of the possible rotations. However, our experimental setup restricts us to a small range of these rotations, due to the optical spin pumping of the nuclei requiring the sample's growth axis to be aligned with the magnetic field, with the generated nuclear polarisation significantly decreasing with increasing rotation. However, the rotation to enable the observation of the S_{44} component is only necessary during the NMR's RF pulse. With the nuclear spins having a long lifetime, it is potentially possible to start with the sample orientated so that its growth axis is aligned with the magnetic field for the pumping of the nuclear spins, rotate the sample for the RF depolarisation pulse and then rotate the sample back to the start position for the detection of the spin polarisation. However, due to the requirements of the optical alignment, for both spin pumping and polarisation detection, this is not possible with current technology as any method to do this would result

in the sample being returned to a different position to that it had at the start. Alternatively, the magnetic field could be rotated with respect to the sample; however, this is also plagued with problems, due to the strength of the field and range of angles required. Therefore, our measurement of the gradient elastic tensor for GaAs is likely to be the most accurate for the foreseeable future.

The measurement of the up-conversion and DNP phenomena in GaAs/AlGaAs dots is important as understanding the origins of these effects gives us a greater insight into the sample's structure and how the quantum dots interact with their environment. The studying of sample C has demonstrated some of the effects of having a smaller barrier, with that of sample B demonstrating the effects of strain. The determination of the origins of the unexpected phenomena observed in the samples is limited by the collected data. The understanding of these effects, therefore, could be furthered by collecting more data, particularly from lower excitation energies, which were not possible with our setup.

Chapter 8

Bibliography

[1] A. I. Ekimov & A. A. Onushchenko. “Quantum size effect in three-dimensional microscopic semiconductor crystals”. *Journal of Experimental and Theoretical Physics Letters* **34**(6), 345–349 (1981).

[2] V. G. Lifshits, A. A. Saranin, A. V. Zotov & M. Katayama. *Surface Science*. Springer-Verlag GmbH, 2003. ISBN: 3540005455.

[3] O. Gywat, H. J. Krenner & J. Berezovsky. *Spins in Optically Active Quantum Dots*. Wiley VCH Verlag GmbH, 2009. ISBN: 3527408061.

[4] Q. Xie, A. Madhukar, P. Chen & N. P. Kobayashi. “Vertically Self-Organized InAs Quantum Box Islands on GaAs(100)”. *Physical Review Letters* **75**(13), 2542–2545 (1995). DOI: 10.1103/physrevlett.75.2542.

[5] I. Kegel, T. H. Metzger, A. Lorke, J. Peisl, J. Stangl, G. Bauer, J. M. Garciá & P. M. Petroff. “Nanometer-Scale Resolution of Strain and Interdiffusion in Self-Assembled InAs/GaAs Quantum Dots”. *Physical Review Letters* **85**(8), 1694–1697 (2000). DOI: 10.1103/physrevlett.85.1694.

[6] W. M. McGee, T. J. Krzyzewski & T. S. Jones. “Atomic scale structure and morphology of (In,Ga)As-capped InAs quantum dots”. *Journal of Applied Physics* **99**(4), 043505 (2006). DOI: 10.1063/1.2172228.

[7] D. M. Bruls, J. W. A. M. Vugs, P. M. Koenraad, H. W. M. Salemink, J. H. Wolter, M. Hopkinson, M. S. Skolnick, F. Long & S. P. A. Gill. “Determination of the shape and indium distribution of low-growth-rate InAs quantum dots by cross-sectional scanning

tunneling microscopy". *Applied Physics Letters* **81**(9), 1708–1710 (2002). DOI: 10.1063/1.1504162.

[8] R. Leon, Y. Kim, C. Jagadish, M. Gal, J. Zou & D. J. H. Cockayne. "Effects of interdiffusion on the luminescence of InGaAs/GaAs quantum dots". *Applied Physics Letters* **69**(13), 1888–1890 (1996). DOI: 10.1063/1.117467.

[9] A. Zrenner, L. V. Butov, M. Hagn, G. Abstreiter, G. Böhm & G. Weimann. "Quantum dots formed by interface fluctuations in AlAs/GaAs coupled quantum well structures". *Physical Review Letters* **72**(21), 3382–3385 (1994). DOI: 10.1103/physrevlett.72.3382.

[10] D. Gammon, A. L. Efros, T. A. Kennedy, M. Rosen, D. S. Katzer, D. Park, S. W. Brown, V. L. Korenev & I. A. Merkulov. "Electron and Nuclear Spin Interactions in the Optical Spectra of Single GaAs Quantum Dots". *Physical Review Letters* **86**(22), 5176–5179 (2001). DOI: 10.1103/physrevlett.86.5176.

[11] C.-D. Lee, C. Park, H. J. Lee, S. K. Noh, K.-S. Lee & S.-J. Park. "Formation of self-assembled GaAs/AlGaAs quantum dots by low-temperature epitaxy". *Applied Physics Letters* **73**(18), 2615–2617 (1998). DOI: 10.1063/1.122523.

[12] S. Ishida, Y. Arakawa & K. Wada. "Seeded self-assembled GaAs quantum dots grown in two-dimensional V grooves by selective metal–organic chemical-vapor deposition". *Applied Physics Letters* **72**(7), 800–802 (1998). DOI: 10.1063/1.120897.

[13] R. Nötzel, Z. Niu, M. Ramsteiner, H.-P. Schönherr, A. Tranpert, L. Däweritz & K. H. Ploog. "Uniform quantum-dot arrays formed by natural self-faceting on patterned substrates". *Nature* **392**(6671), 56–59 (1998). DOI: 10.1038/32127.

[14] A. Rastelli, S. Stufler, A. Schliwa, R. Songmuang, C. Manzano, G. Costantini, K. Kern, A. Zrenner, D. Bimberg & O. G. Schmidt. "Hierarchical Self-Assembly of GaAs/AlGaAs Quantum Dots". *Physical Review Letters* **92**(16), 166104 (2004). DOI: 10.1103/physrevlett.92.166104.

[15] C. Heyn, A. Stemmann, T. Köppen, C. Strelow, T. Kipp, M. Grave, S. Mendach & W. Hansen. "Highly uniform and strain-free GaAs quantum dots fabricated by filling

of self-assembled nanoholes". *Applied Physics Letters* **94**(18), 183113 (2009). DOI: 10.1063/1.3133338.

[16] A. Stemmann, C. Heyn, T. Köppen, T. Kipp & W. Hansen. "Local droplet etching of nanoholes and rings on GaAs and AlGaAs surfaces". *Applied Physics Letters* **93**(12), 123108 (2008). DOI: 10.1063/1.2981517.

[17] H. Drexler, D. Leonard, W. Hansen, J. P. Kotthaus & P. M. Petroff. "Spectroscopy of Quantum Levels in Charge-Tunable InGaAs Quantum Dots". *Physical Review Letters* **73**(16), 2252–2255 (1994). DOI: 10.1103/physrevlett.73.2252.

[18] R. J. Warburton, C. Schäflein, D. Haft, F. Bickel, A. Lorke, K. Karrai, J. M. Garcia, W. Schoenfeld & P. M. Petroff. "Optical emission from a charge-tunable quantum ring". *Nature* **405**(6789), 926–929 (2000). DOI: 10.1038/35016030.

[19] A. Bracker, E. Stinaff, D. Gammon, M. Ware, J. Tischler, A. Shabaev, A. Efros, D. Park, D. Gershoni, V. Korenev & I. Merkulov. "Optical Pumping of the Electronic and Nuclear Spin of Single Charge-Tunable Quantum Dots". *Physical Review Letters* **94**(4) (2005). DOI: 10.1103/physrevlett.94.047402.

[20] L. Bouet, M. Vidal, T. Mano, N. Ha, T. Kuroda, M. V. Durnev, M. M. Glazov, E. L. Ivchenko, X. Marie, T. Amand, K. Sakoda, G. Wang & B. Urbaszek. "Charge tuning in [111] grown GaAs droplet quantum dots". *Applied Physics Letters* **105**(8), 082111 (2014). DOI: 10.1063/1.4894174.

[21] L. Zhai, M. C. Löbl, G. N. Nguyen, J. Ritzmann, A. Javadi, C. Spinnler, A. D. Wieck, A. Ludwig & R. J. Warburton. "Low-noise GaAs quantum dots for quantum photonics". *Nature Communications* **11**(1), 4745 (2020). DOI: 10.1038/s41467-020-18625-z.

[22] M. Fox. *Optical Properties of Solids*. Oxford University Press, 2010. 396 pp. ISBN: 0199573360.

[23] P. Michler. *Single Quantum Dots: Fundamentals, Applications, and New Concepts*. Berlin New York: Springer-Verlag, 2003. ISBN: 3540140220.

[24] H. W. van Kesteren, E. C. Cosman, W. A. J. A. van der Poel & C. T. Foxon. "Fine structure of excitons in type-II GaAs/AlAs quantum wells". *Physical Review B* **41**(8), 5283–5292 (1990). DOI: 10.1103/physrevb.41.5283.

[25] D. Sarkar, H. P. van der Meulen, J. M. Calleja, J. M. Becker, R. J. Haug & K. Pierz. "Exciton fine structure and biexciton binding energy in single self-assembled InAs/AlAs quantum dots". *Journal of Applied Physics* **100**(2), 023109 (2006). DOI: 10.1063/1.2209089.

[26] W. S. Slaughter. *The Linearized Theory of Elasticity*. Birkhäuser Boston, 2012. 572 pp. ISBN: 1461266084.

[27] M. Grundmann. *The Physics of Semiconductors*. Springer-Verlag GmbH, 2016. ISBN: 3319238795.

[28] T. B. Bahder. "Eight-band k·p model of strained zinc-blende crystals". *Physical Review B* **41**(17), 11992–12001 (1990). DOI: 10.1103/physrevb.41.11992.

[29] D. A. B. Miller, D. S. Chemla, T. C. Damen, A. C. Gossard, W. Wiegmann, T. H. Wood & C. A. Burrus. "Band-Edge Electroabsorption in Quantum Well Structures: The Quantum-Confined Stark Effect". *Physical Review Letters* **53**(22), 2173–2176 (1984). DOI: 10.1103/physrevlett.53.2173.

[30] T. Unold, K. Mueller, C. Lienau, T. Elsaesser & A. D. Wieck. "Optical Stark Effect in a Quantum Dot Ultrafast Control of Single Exciton Polarizations". *Physical Review Letters* **92**(15), 157401 (2004). DOI: 10.1103/physrevlett.92.157401.

[31] C. Kloeffel & D. Loss. "Prospects for Spin-Based Quantum Computing in Quantum Dots". *Annual Review of Condensed Matter Physics* **4**(1), 51–81 (2013). DOI: 10.1146/annurev-conmatphys-030212-184248.

[32] A. M. Stoneham. *Theory of defects in solids : electronic structure of defects in insulators and semiconductors*. Oxford New York: Clarendon Press Oxford University Press, 1975. ISBN: 0198507801.

[33] B. Urbaszek, X. Marie, T. Amand, O. Krebs, P. Voisin, P. Maletinsky, A. Högele & A. Imamoglu. "Nuclear spin physics in quantum dots: An optical investigation". *Reviews of Modern Physics* **85**(1), 79–133 (2013). DOI: 10.1103/revmodphys.85.79.

[34] E. A. Chekhovich, A. Ulhaq, E. Zallo, F. Ding, O. G. Schmidt & M. S. Skolnick. "Measurement of the spin temperature of optically cooled nuclei and GaAs hyperfine constants in GaAs/AlGaAs quantum dots". *Nature Materials* **16**(10), 982–986 (2017). DOI: 10.1038/nmat4959.

[35] A. Abragam. *The principles of nuclear magnetism*. Oxford: Clarendon Press, 1978. ISBN: 0198512368.

[36] P. Callaghan. *Principles of nuclear magnetic resonance microscopy*. Oxford England: Clarendon Press, 1991. ISBN: 0198539444.

[37] C. Slichter. *Principles of magnetic resonance*. Berlin New York: Springer-Verlag, 1990. ISBN: 0387501576.

[38] G. Gillard, I. M. Griffiths, G. Ragunathan, A. Ulhaq, C. McEwan, E. Clarke & E. A. Chekhovich. "Fundamental limits of electron and nuclear spin qubit lifetimes in an isolated self-assembled quantum dot". *npj Quantum Information* **7**(1), 43 (2021). DOI: 10.1038/s41534-021-00378-2.

[39] M. Cross & M. J. Adams. "Effects of doping and free carriers on the refractive index of direct-gap semiconductors". *Opto-electronics* **6**(3), 199–216 (1974). DOI: 10.1007/bf01423984.

[40] G. Cowan. *Statistical Data Analysis*. OUP Oxford, 1998. 212 pp. ISBN: 0198501552.

[41] S. M. Sze & K. K. Ng. *Physics of semiconductor devices*. John Wiley & Sons, 2007. ISBN: 9780471143239.

[42] B. Tuck. *Atomic diffusion in III-V semiconductors*. A. Hilger, 1988. ISBN: 9780852743515.

[43] B. L. Sharma. *Diffusion in semiconductors*. eng. Clausthal-Zellerfeld (W.Ger): Trans Tech, 1970.

[44] J. Rouquerol, K. S. W. Sing & P. Llewellyn. "Adsorption by Metal Oxides". In: *Adsorption by Powders and Porous Solids*. Elsevier, 2014, pp. 393–465. DOI: 10.1016/b978-0-08-097035-6.00011-5.

[45] R. J. Harrison & P. L. Sagalyn. "Trace Relations for Tensors Relating Electric Fields and Elastic Strains to Nuclear Quadrupole Effects". *Physical Review* **128**(4), 1630–1631 (1962). DOI: 10.1103/physrev.128.1630.

[46] Y. Sun, S. Thompson & T. Nishida. *Strain Effect in Semiconductors*. Springer-Verlag GmbH, 2009. ISBN: 1441905510.

[47] S. Adachi, P. Capper, S. Kasap & A. Willoughby. *Properties of Semiconductor Alloys: Group-IV, III-V and II-VI Semiconductors*. John Wiley & Sons, 2009. 424 pp. ISBN: 0470743697.

[48] N. J. Stone. "Table of nuclear electric quadrupole moments". *Atomic Data and Nuclear Data Tables* **111-112**, 1–28 (2016). DOI: 10.1016/j.adt.2015.12.002.

[49] I. Vurgaftman, J. R. Meyer & L. R. Ram-Mohan. "Band parameters for III–V compound semiconductors and their alloys". *Journal of Applied Physics* **89**(11), 5815–5875 (2001). DOI: 10.1063/1.1368156.

[50] F. H. Pollak, M. Cardona & K. L. Shaklee. "Piezoelectroreflectance in GaAs". *Physical Review Letters* **16**(21), 942–944 (1966). DOI: 10.1103/physrevlett.16.942.

[51] M. Chandrasekhar & F. H. Pollak. "Effects of uniaxial stress on the electroreflectance spectrum of Ge and GaAs". *Physical Review B* **15**(4), 2127–2144 (1977). DOI: 10.1103/physrevb.15.2127.

[52] R. Bendorius & A. Shileika. "Electroreflectance spectra of GaAs at hydrostatic pressure". *Solid State Communications* **8**(14), 1111–1113 (1970). DOI: 10.1016/0038-1098(70)90007-4.

[53] H. Qiang, F. H. Pollak & G. Hickman. "Piezo-photoreflectance of the direct gaps of GaAs and Ga0.78Al0.22As". *Solid State Communications* **76**(9), 1087–1091 (1990). DOI: 10.1016/0038-1098(90)90970-m.

[54] R. K. Sundfors. "Experimental gradient-elastic tensors and chemical bonding in III-V semiconductors". *Physical Review B* **10**(10), 4244–4252 (1974). DOI: 10.1103/physrevb.10.4244.

[55] M. N. Makhonin, E. A. Chekhovich, P. Senellart, A. Lemaître, M. S. Skolnick & A. I. Tartakovskii. "Optically tunable nuclear magnetic resonance in a single quantum dot". *Physical Review B* **82**(16), 161309 (2010). DOI: 10.1103/physrevb.82.161309.

[56] R. K. Sundfors. “Determination of the Gradient-Elastic Tensors forAIIIBVCompounds Using Nuclear Acoustic Resonance”. *Physical Review* **177**(3), 1221–1230 (1969). DOI: 10.1103/physrev.177.1221.

[57] A. Ulhaq, Q. Duan, E. Zallo, F. Ding, O. G. Schmidt, A. I. Tartakovskii, M. S. Skolnick & E. A. Chekhovich. “Vanishing electron g factor and long-lived nuclear spin polarization in weakly strained nanohole-filled GaAs/AlGaAs quantum dots”. *Physical Review B* **93**(16), 165306 (2016). DOI: 10.1103/physrevb.93.165306.

[58] Y. Yang, Y. H. Zhang, W. Z. Shen & H. C. Liu. “Semiconductor infrared up-conversion devices”. *Progress in Quantum Electronics* **35**(4), 77–108 (2011). DOI: 10.1016/j.pquantelec.2011.05.001.

[59] I. V. Ignatiev, I. E. Kozin, H.-W. Ren, S. Sugou & Y. Masumoto. “Anti-Stokes photoluminescence of InP self-assembled quantum dots in the presence of electric current”. *Physical Review B* **60**(20), R14001–R14004 (1999). DOI: 10.1103/physrevb.60.r14001.

[60] N. S. Makarov, Q. Lin, J. M. Pietryga, I. Robel & V. I. Klimov. “Auger Up-Conversion of Low-Intensity Infrared Light in Engineered Quantum Dots”. *ACS Nano* **10**(12), 10829–10841 (2016). DOI: 10.1021/acsnano.6b04928.

[61] R. E. Halsted, E. F. Apple, J. S. Prener & W. W. Piper. “Two-step Optical Excitation in CdS and ZnS”. In: *Proceedings of the International Conference on Semiconductor Physics* (Prague, 1960). Academic Press, 1961, pp. 776–779.

[62] A. Schindler, R. Bindemann & K. Kreher. “Two-step excitation of photoluminescence in GaP”. *Physica Status Solidi (b)* **59**(2), 439–445 (1973). DOI: 10.1002/pssb.2220590208.

[63] E. J. Johnson, J. Kafalas, R. W. Davies & W. A. Dyes. “Deep center EL2 and anti-Stokes luminescence in semi-insulating GaAs”. *Applied Physics Letters* **40**(11), 993–995 (1982). DOI: 10.1063/1.92954.

[64] L. G. Quagliano & H. Nather. “Up conversion of luminescence via deep centers in high purity GaAs and GaAlAs epitaxial layers”. *Applied Physics Letters* **45**(5), 555–557 (1984). DOI: 10.1063/1.95319.

[65] P. P. Paskov, P. O. Holtz, B. Monemar, J. M. Garcia, W. V. Schoenfeld & P. M. Petroff. "Photoluminescence up-conversion in InAs/GaAs self-assembled quantum dots". *Applied Physics Letters* **77**(6), 812–814 (2000). DOI: 10.1063/1.1306653.

[66] N. Kamata, K. Hoshino, T. Uchida, K. Yamada, M. Nishioka & Y. Arakawa. "Up-conversion luminescence via a below-gap state in GaAs/AlGaAs quantum wells". *Superlattices and Microstructures* **22**(4), 521–527 (1997). DOI: 10.1006/spmi.1996.0293.

[67] C. Kammerer, G. Cassabois, C. Voisin, C. Delalande, P. Roussignol & J. M. Gérard. "Photoluminescence Up-Conversion in Single Self-Assembled InAs/GaAs Quantum Dots". *Physical Review Letters* **87**(20), 207401 (2001). DOI: 10.1103/physrevlett.87.207401.

[68] E. A. Chekhovich, M. N. Makhonin, K. V. Kavokin, A. B. Krysa, M. S. Skolnick & A. I. Tartakovskii. "Pumping of Nuclear Spins by Optical Excitation of Spin-Forbidden Transitions in a Quantum Dot". *Physical Review Letters* **104**(6), 066804 (2010). DOI: 10.1103/physrevlett.104.066804.

[69] E. A. Chekhovich, A. B. Krysa, M. S. Skolnick & A. I. Tartakovskii. "Light-polarization-independent nuclear spin alignment in a quantum dot". *Physical Review B* **83**(12), 125318 (2011). DOI: 10.1103/physrevb.83.125318.

[70] J. Puebla, E. A. Chekhovich, M. Hopkinson, P. Senellart, A. Lemaitre, M. S. Skolnick & A. I. Tartakovskii. "Dynamic nuclear polarization in InGaAs/GaAs and GaAs/AlGaAs quantum dots under nonresonant ultralow-power optical excitation". *Physical Review B* **88**(4), 045306 (2013). DOI: 10.1103/physrevb.88.045306.

[71] G. Ragunathan, J. Kobak, G. Gillard, W. Pacuski, K. Sobczak, J. Borysiuk, M. Skolnick & E. Chekhovich. "Direct Measurement of Hyperfine Shifts and Radio Frequency Manipulation of Nuclear Spins in Individual CdTe/ZnTe Quantum Dots". *Physical Review Letters* **122**(9), 096801 (2019). DOI: 10.1103/physrevlett.122.096801.

[72] B. Urbaszek, P.-F. Braun, T. Amand, O. Krebs, T. Belhadj, A. Lemaítre, P. Voisin & X. Marie. "Efficient dynamical nuclear polarization in quantum dots: Temperature de-

pendence". *Physical Review B* **76**(20), 201301 (2007). DOI: 10.1103/physrevb.76.201301.

[73] A. K. Paravastu & J. A. Reimer. "Nuclear spin temperature and magnetization transport in laser-enhanced NMR of bulk GaAs". *Physical Review B* **71**(4), 045215 (2005). DOI: 10.1103/physrevb.71.045215.

[74] P. J. Coles & J. A. Reimer. "Penetration depth model for optical alignment of nuclear spins in GaAs". *Physical Review B* **76**(17), 174440 (2007). DOI: 10.1103/physrevb.76.174440.

[75] Y. Li, J. P. King, L. Peng, M. C. Tamargo, J. A. Reimer & C. A. Meriles. "Helicity independent optically-pumped nuclear magnetic resonance in gallium arsenide". *Applied Physics Letters* **98**(11), 112101 (2011). DOI: 10.1063/1.3564897.

[76] A. K. Paravastu, S. E. Hayes, B. E. Schwickert, L. N. Dinh, M. Balooch & J. A. Reimer. "Optical polarization of nuclear spins in GaAs". *Physical Review B* **69**(7), 075203 (2004). DOI: 10.1103/physrevb.69.075203.

[77] Y. Li, J. P. King, J. A. Reimer & C. A. Meriles. "Near-band-gap photoinduced nuclear spin dynamics in semi-insulating GaAs: Hyperfine- and quadrupolar-driven relaxation". *Physical Review B* **88**(23), 235211 (2013). DOI: 10.1103/physrevb.88.235211.

[78] K. Ramaswamy, S. Mui, S. A. Crooker, X. Pan, G. D. Sanders, C. J. Stanton & S. E. Hayes. "Optically pumped NMR: Revealing spin-dependent Landau level transitions in GaAs". *Physical Review B* **82**(8), 085209 (2010). DOI: 10.1103/physrevb.82.085209.

[79] M. Vachon, S. Raymond, A. Babinski, J. Lapointe, Z. Wasilewski & M. Potemski. "Energy shell structure of a single InAs/GaAs quantum dot with a spin-orbit interaction". *Physical Review B* **79**(16), 165427 (2009). DOI: 10.1103/physrevb.79.165427.

[80] A. M. Hennel, C. D. Brandt, K. Y. Ko & L. M. Pawlowicz. "Properties of Titanium in GaAs and InP". *Materials Science Forum* **10-12**, 645–650 (1986). DOI: 10.4028/www.scientific.net/msf.10-12.645.

[81] P. Krispin & H. Kostial. “Deep-level planar doping of titanium in GaAs”. *physica status solidi (b)* **194**(1), 145–158 (1996). DOI: 10.1002/pssb.2221940115.

[82] H. J. Queisser. “Defects in Semiconductors: Some Fatal, Some Vital”. *Science* **281**(5379), 945–950 (1998). DOI: 10.1126/science.281.5379.945.

[83] D. M. Hofmann, B. K. Meyer, J.-M. Spaeth, M. Wattenbach, J. Krüger, C. Kisielowski-Kemmerich & H. Alexander. “EL2 and anion antisite defects in plastically deformed GaAs”. *Journal of Applied Physics* **68**(7), 3381–3385 (1990). DOI: 10.1063/1.346341.

[84] P. Trautman & J. M. Baranowski. “Structure and metastability of the EL2 defect in GaAs”. *International Journal of Modern Physics B* **09**(11), 1263–1312 (1995). DOI: 10.1142/s0217979295000549.